Rational design of advanced electrocatalysts for oxygen and hydrogen reactions in fuel cells and water electrolyzers

by

Yang Qiu

A dissertation submitted to the graduate faculty

in partial fulfillment of the requirements for the degree of

DOCTOR OF PHILOSOPHY

Major: Chemical Engineering

Program of Study Committee:
Wenzhen Li, Major professor
Eric W. Cochran
Jean-Philippe Tessonnier
George A. Kraus
Robbyn K. Anand

The student author, whose presentation of the scholarship herein was approved by the program of study committee, is solely responsible for the content of this dissertation. The Graduate College will ensure this dissertation is globally accessible and will not permit alterations after a degree is conferred.

Iowa State University

Ames, Iowa

2018

TABLE OF CONTENTS

LIST OF FIGURES

LIST OF TABLES

NOMENCLATURE

PEMFCs	Proton Exchange Membrane Fuel Cells
AFCs	Alkaline Fuel Cells
HEMFCs	Hydroxide Exchange Membrane Fuel Cells
SOFC	Solid Oxide Fuel Cell
PAFC	Phosphoric Acid Fuel Cell
MCFC	Molten Carbonate Fuel Cell
AEMFCs	Anion Exchange Membrane Fuel Cells
ORR	Oxygen Reduction Reaction
PGM	Platinum Group Metals
DFT	Density Functional Theory
OER	Oxygen Evolution Reaction
RDE	Rotating Disk Electrode
RRDE	Rotating Ring-Disk Electrode
SHE	Standard Hydrogen Electrode
RHE	Reversible Hydrogen Electrode
GC-RDE	Glassy Carbon Rotating Disk Electrode
MEA	Membrane Electrode Assembly
ECSA	Electrochemical Surface Area
OAm	Oleylamine
OAc	Oleic Acid
PTFE	Polytetrafluoroethylene
Benzyl Ether	BE

STEM	Scanning Transmission Electron Microscopy
SAED	Selected Area Electron Diffraction
SEM	Scanning Electron Microscope
EDS	Energy-Dispersive X-Ray Spectroscopy
XRD	X-Ray Powder Diffraction
XPS	X-Ray Photoelectron Spectroscopy
ICP-AES	Inductively Coupled Plasma Atomic Emission Spectroscopy
BET theory	Brunauer–Emmett–Teller Theory
CV	Cyclic Voltammetry
LSV	Linear Sweep Voltammetry
CA	Chronoamperometry
EIS	Electrochemical Impedance Spectroscopy
MMO	Mercury / Mercury Oxide
TOF	Turnover Frequency
IPA	Iso-Propanol
HOR	Hydrogen Oxidation Reaction
HER	Hydrogen Evolution Reaction
HBE	Hydrogen Binding Energy
	Half-Wave Potential Difference

RIR   Reference Intensity Ratio

NPs   Nano-particles

$E_{1/2}$ Half-Wave Potential Difference

ACKNOWLEDGMENTS

members and other faculty and staff in Chemical and Biological Engineering Department

at Iowa State University.

ABSTRACT

With the fast growing of global population and living standards, the sufficient energy supplying to meet global energy consumption becomes the most important and difficult challenge toward the human beings. To mitigate the significant requirement of fossil fuels, the sustainable energy as a promising alternative to fossil fuel has been extensively developed. In the energy cycle, the renewable primary energy conversion as well as following electrical energy storage and conversion plays a critical role, and water electrolyzers and fuel cells as the representative energy storage and conversion devices have been attracted much attention. However, the relatively low activity of catalysts toward hydrogen and oxygen reactions and high cost of catalysts still limit the practical applications of water electrolyzers and fuel cells. Therefore, my Ph.D. research is focused on the rational design and investigation of advanced electrocatalysts toward oxygen reduction/evolution reactions (ORR/OER), and hydrogen evolution/oxidation reactions (HER/HOR) with a promising activity and durability employed in practical energy storage and conversion applications, e.g. fuel cells, and water electrolyzers.

In terms of ORR, the N- and S- dual doped mesoporous carbon materials (N-S-CMK-3) were rationally synthesized serving as electrocatalytic ORR catalysts, featuring the high surface area originated by highly organized hierarchical mesoporous structures, which could desirably facilitate the diffusion of O_2 fuel. This N-S-CMK-3 exhibits remarkable ORR activity and durability in direct alcohol fuel cells (alkaline environment); For OER catalysts, the carbon supported amorphous NiFe nanoparticles was rationally synthesised as the highly active OER catalysts, which exhibits promising OER activity with remarkable durability for long-term electrocatalytic OER tests; On the other hand, the bcc structured

PdCu NPs was prepared to meet the requirement of high HOR activity in alkaline electrolyte. The crystalline structure transformation with thermal treatment temperature was also investigated, which provide a promising guide for highly active HOR catalyst design

CHAPTER 1. INTRODUCTION AND SIGNIFICANCE OF THE RESEARCH

1.1 Energy outlooks

In the coming years, with the world population rapidly increasing, great concerns about global warming due to increased greenhouse gas CO_2 emissions, and major crude oil reserves diminishing, our present unsustainable energy situation of heavy reliance on nonrenewable fossil resource has to be changed. The world consumption of primary energy, which is dominated by fossil fuel consumption, has greatly increased from 3.8 billion tons of oil equivalent in 1965 to 12.2 billion tons of oil equivalent in 2011. The growth in the world economy means more energy is required, thereby, energy consumption will continuously increase, and is predicted to be 34 % between 2014 and 2035 (**Figure 1a**).[1] Although, we can use coal and natural gas to cover the gap left behind oil, he fossil fuels still remain the dominant source of energy powering the global economy, providing almost 80% of total energy supply in 2035 (down from 86% 2014), and it is still only a matter of time to exhaust all the fossil resources.[1, 2]

Renewable energy, which is derived from the continually replenished resources such as sunlight, wind, biomass, geothermal heat, etc., is more desirable for our sustainable social development. Among non-fossil fuels, renewables grow rapidly (6.6% p.a.), causing their share in primary energy to rise from around 3% today to 9% by 2035, and the demand of renewable energy will sharply increase, closing to oil requirement at 2035 (**Figure 1b**).[1, 2] In addition, most of the renewables fuels, up to 38%, serve to power generation, especially in Europe and United states (**Figure 1c**).[2]
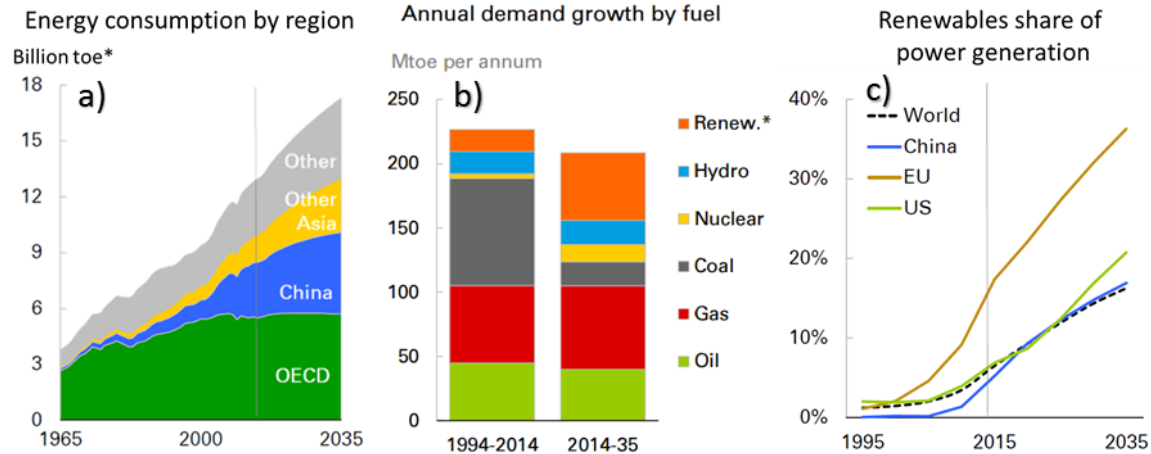
Figure 1.1 a) Graphic of energy consumption by region from 1965 to 2035; **b)** Graphic energy annual demand growth by fuel from 1994 to 2035; **c)** Graphic of renewables share of power generation growth from 1995 to 2035.[2] Copyright 1996-2016 BP p.l.c., used with permission.

1.2 Fuel cells - the promising electrical energy conversion technologies

To obtain usable electrical energy from renewable energy sources, many energy conversion techniques are widely investigated. Among all alternative power generation techniques, fuel cells are more attractive, featuring high energy conversion efficiency, zero pollutant emissions, as well as quiet operation (alleviate noise pollution). As an energy conversion device, fuel cells can directly convert the energy stored in chemical bonds, into electrical energy without the Carnot cycle's limitation. It is noteworthy that the ideal H_2/O_2 fuel cell shows a remarkably high energy conversion efficiently of 83% (based on ratio of Gibbs free energy change to enthalpy), whereas the traditional fossil fuel combustion engines can reach only <50% energy conversion efficiency. If the renewable biomass compounds are employed as chemical fuel for energy conversion, a higher theoretical energy conversion efficiency can be obtained as i.e. 97% of ethanol, and 99% of glycerol.

There are five main types of fuel cells classified by the type of electrolyte: 1) Proton-exchange membrane fuel cells (PEMFCs); 2) Alkaline fuel cells (AFCs); 3) Solid oxide fuel cells (SOFCs); 4) Phosphoric acid fuel cells (PAFCs); and 5) molten carbonate fuel

cells (MCFCs). The PEMFC is more attractive owning to its low operation temperature, quick-start time, and high power-to-weight ratio, and thus, has been extensively used in portable energy suppliers and passenger vehicles, such as cars and buses. However, the widespread applications of PEMFC could be hindered by three main issues: 1) the sluggish kinetics of oxygen reduction reaction (at the cathode) with the unsatisfied durability of the cathode catalyst; 2) high cost for Pt-group metal catalysts for PEMFCs; 3) the replacement of H_2 with renewable, easily stored and transported liquid fuels. In the regard of discussed issues above, AFCs were studied. In high pH media, non-noble transition metal based catalysts can survive for a longer term, thus significantly decreasing the total cost for catalysts, whereas only noble metal can be used in acidic environment in PEMFCs from a long term stable fuel cell operation point of view. On the other hand, the biomass derived compounds could serve as anode fuel replacing H_2 in AFCs, and the slow kinetic of ethanol oxidation can be significantly improved in high pH media. By using a solid anion exchange membrane as the electrolyte, the liquid KOH electrolyte could be removed from AFCs system, which can effectively prevent the electrode flooding issue for traditional AFCs. Consequently, the AEM fuel cells structure become close to conventional PEMFCs, except that they use an alkaline membrane instead of an acid membrane, so called as anion-exchange membrane fuel cells (AEMFC) (**Figure 1.2**). The H_2 fuel or other biomass derived compounds (e.g. ethanol, glycerol) will be oxidized at the anode side of AEMFCs, while the air (O_2) will be reduced at cathode side, and the two reaction chambers is separated by an ion-exchange membrane to prevent the fuel and electrolyte crossover.
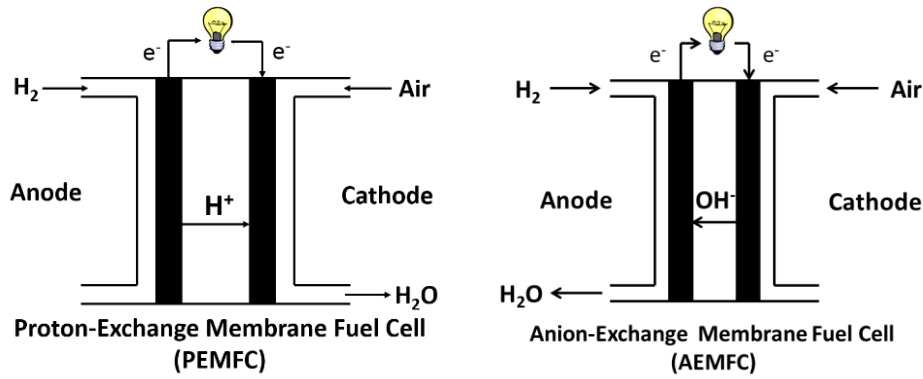
Figure 1.2 Schematic of proton-exchange membrane fuel cell (PEMFC) and anion-exchange membrane fuel cell (AEMFC).

1.3 Water electrolyzers – an primising renewable primary energy storage technologies in the future

The water electrolysis, featuring high purity H_2/O_2 generation, simply process, and environmental friendly, has been considered as a promising renewable primary energy conversion technology. In the absence of energy storage devices, the renewable primary energy could face many problems including regionalism, intermittence, etc., which could cause an instable power supplying and electrical energy waste at off-peak times. Therefore, the energy storage system is required, and the water electrolyzers has been extensively developed, owing to the simple low regional limitation, low system cost, and environmental friendly. On the other hand, hydrogen, which has the highest specific energy density, is considered as a good energy carrier to mitigate the requirement of global energy consumption in the future. Although about 96% hydrogen was obtained from hydrocarbon sources via pyrolysis, the water electrolysis for hydrogen generation possess the advantages of high purity and zero CO_2 and CO emission, thereby attracting a great attention.[3]

The water electrolyzer is composed of oxygen evolution reaction (OER) (anode) and hydrogen evolution reaction (HER) (cathode), and an ion exchange membrane can be used to separate two reaction chambers.
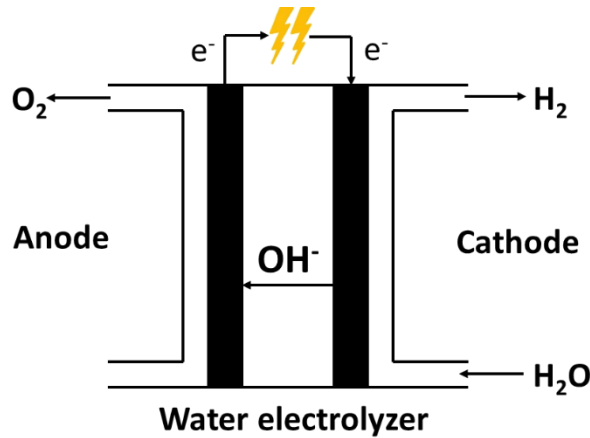
Figure 1.3 Schematic of water electrolyzer with hydroxide exchange membrane

1.4 Rechargeable metal air batteries - An efficient electrical energy storage technology

In sharp contrast to the fuel cells, the metal air batteries can store the excess electrical energy to chemical energy in a battery system. The energy storage technologies can be divided into four types, including mechanical, electrical, chemical, and electrochemical. Among all energy storage technologies, the pumped hydroelectric system as well as the compressed air energy storage system account for higher than 99.5% of a worldwide storage capacity of 128 GW of discharge power.[3] However, the long respond time to fast power demand, geographical prerequisite, and high capital cost severely limit their applications. Conversely, electrochemical energy storage, especially for rechargeable batteries, possesses a number advantages, including flexible, modular power and energy characteristics to meet different grid functions with fast response time, pollution-free operation, high round-trip efficiency, long cycle life, and low capital and maintenances

cost, thereby, recently attracting much more attentions. Among these batteries, the metal-air batteries are more favorable because of their high gravimetric volumetric energy density (**Table 1**). The schematic representation of a typical Li-O_2 battery is shown in **Figure 1.3**. On discharging mode, the Li-metal anode is oxidized, releasing Li^+ into the electrolyte, while the O_2/air from the atmosphere reach the porous cathode and dissolves into electrolyte, followed by the reduction at the cathode electrode surface to form LiOH with Li^+ in alkaline environment. On discharging mode, both processes are reversed, representing as oxygen evolution (anode side) and Li^+ reduction (cathode side). Although, the fundamental mechanisms of O_2 reduction and evolution in aqueous electrolyte have been extensively studied, the detailed chemistry behind them still need to be further understood, and the highly active ORR and OER catalysts are still required to lower the extra energy cost caused by poor kinetics of ORR and OER.[3-5]

Table 1 Data for several electrochemical reactions that form the basis of energy-storage devices.[5] Copyright (2011), Rights Managed by Nature Publishing Group, used with permission.

Battery	Cell voltage (V)	Theoretical specific energy (Wh kg⁻¹)	Theoretical energy density (Wh l⁻¹)
Today's Li-ion $\frac{1}{2}C_6Li + Li_{0.5}CoO_2 \leftrightarrow 3C + LiCoO_2$	3.8	387	1,015
Zn–air $Zn + \frac{1}{2}O_2 \leftrightarrow ZnO$	1.65	1,086	6,091* (ZnO)
Li–S $2Li + S \leftrightarrow Li_2S$	2.2	2,567	2,199† (Li + Li₂S)
Li–O_2 (non-aqueous) $2Li + O_2 \leftrightarrow Li_2O_2$	3.0	3,505	3,436‡ (Li + Li₂O₂)
Li–O_2 (aqueous) $2Li + \frac{1}{2}O_2 + H_2O \leftrightarrow 2LiOH$§	3.2	3,582	2,234‖ (Li + H₂O + LiOH)

*Based on volume of ZnO at the end of discharge; †based on the sum of the volumes of Li at the beginning and Li₂S at the end of discharge; ‡based on the sum of the volumes of Li at the beginning and Li₂O₂ at the end of discharge; §assuming the product is anhydrous LiOH and alkaline conditions; and ‖based on the sum of the volumes of Li + H₂O consumed and the LiOH at the end of discharge.
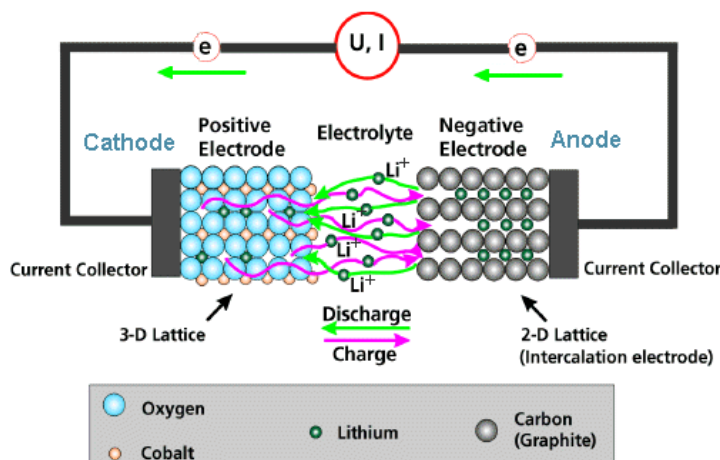
Figure 1.4 Schematic of Li-O$_2$ batteries (cited from hyperscripts of Dr. Helmut Föll, http://www.tf.unikiel.de/matwis/amat/elmat_en/kap_2/advanced/t2_1_3.html), Copyright H. Föll, used with permission.

1.5 The mechanism and application of electrocatalytic oxygen reduction reaction (ORR)

Oxygen reduction reaction (ORR) is the major cathodic reaction that occurs in many energy conversion systems, such as previously discussed rechargeable metal-air batteries (discharging mode) and regenerative fuel cells (power delivery mode). ORR in aqueous solutions occurs mainly by two reaction pathways: 1) the direct 4-electron transfer reduction pathway to generate H_2O (acidic media) or OH^- (alkaline media), and 2) the 2-electron transfer reduction pathway to produce hydroperoxide (H_2O_2) (acidic media) or HO_2^- (alkaline media). The reaction pathways are shown as follows:

Table 2 Thermodynamic electrode potentials of electrochemical O_2 reduction reaction. (Thermodynamic electrode potential is cited from Ref.26)

Electrolyte	ORR	Thermodynamic electrode potential at standard conditions / V vs. SHE
Acidic aqueous solution	$O_2 + 4H^+ + 4e^- \longrightarrow 2H_2O$	1.229
	$O_2 + 2H^+ + 2e^- \longrightarrow H_2O_2$	0.699
	$H_2O_2 + 2H^+ + 2e^- \longrightarrow 2H_2O$	1.760
Alkaline aqueous solution	$O_2 + 2H_2O + 4e^- \longrightarrow 4OH^-$	0.401
	$O_2 + H_2O + 2e^- \longrightarrow HO_2^- + OH^-$	-0.065
	$HO_2^- + H_2O + 2e^- \longrightarrow 3OH^-$	0.867

To minimize the required extra potential (so called overpotential) for ORR and delivery a practically usable current in a fuel cell, a direct 4-electroton transfer reaction predominated ORR catalyst is desired to minimize any unwanted by-products generation (e.g. H_2O_2 or HO_2^-). The state-of-the-art technology still heavily rely on the platinum (Pt)-group metals (PGM), which are the most efficient ORR catalysts at low temperatures. However, their high cost, scarcity, and inferior durability (e.g. agglomeration issue), significantly hinder their widespread applications. In addition, the PGM catalysts have been found to be poisoned after long term test in alcohol fuel cells, which is caused by the crossover of alcohol fuel from the anode to cathode reaction chamber. With the alcohol crossover, electrochemical oxidation of alcohol could occur and compete with the ORR on the PGM catalysts, thereby creating a short-circuit potential to severely decrease the performance of alcohol fuel cell. With the aim of mitigating these barriers, considerable studies are focusing on lowering the PGM loading, or directly replacing PGM by using non-PGM catalysts for electrocatalytic ORR.

The mechanism of ORR on Pt and Pt-based bimetallic catalysts have been extensively investigated by using theoretical density functional theory calculation (DFT) to guide rational ORR catalysts design and synthesis. Nørskov and his co-works reported two possible rate-limiting steps for ORR, including the adsorbed O and OH species removal and dissociation of O_2 (or the transfer of electrons and protons to adsorbed O_2).[6] For metals that bind oxygen too strongly, the ORR rate is limited by the adsorbed O or OH removal process.[7] Conversely, the ORR rate is limited by the O_2 dissociation process, when the metals bind oxygen too weakly. As shown in **Figure 1.4**, both the experimental data and these models strongly suggest that a surface that binds O 0.0 to 0.4 eV more weakly than Pt(111) should exhibit an ORR activity better than Pt, with the optimum at a binding energy of roughly 0.2 eV (volcano peak) weaker than that of Pt. Therefore, the transition metal (e.g. Ni, Fe, Co etc.) was introduced to weaken the oxygen binding, and alloys, Pt_xM_y (M = Ni, Fe, Co etc.) with different morphology were extensively studied. Sun and his co-workers synthesized the $Pt_{0.58}Fe_{0.42}$ alloy nanoparticles, that show comparable ORR performance in acidic environment.[8] Watanabe and his co-workers also reported remarkable ORR activity exhibited by Pt-Co and Pt-Fe nanoparticles.[9] Recently, Huang et.al demonstrated the Mo-doped Pt_3Ni and obtained the well-known highest ORR activity in acidic media.[10] On the other hand, to further reduce the Pt content, Adzic reported the underpotential deposition method that can fabricate a Pt monolayer on Au and Co metals to form a core–shell structured nanoparticles as ORR catalysts.[11, 12]

Transition metal macrocyles have been discovered to be a competitive non-PGM ORR catalyst for a long time. Zelenay and his co-workers did seminal work on polyaniline-Fe-

C, based ORR catalysts and achieve the highest state-of-the-art ORR activity and durability tested in single PEMFC setting.[13, 14].
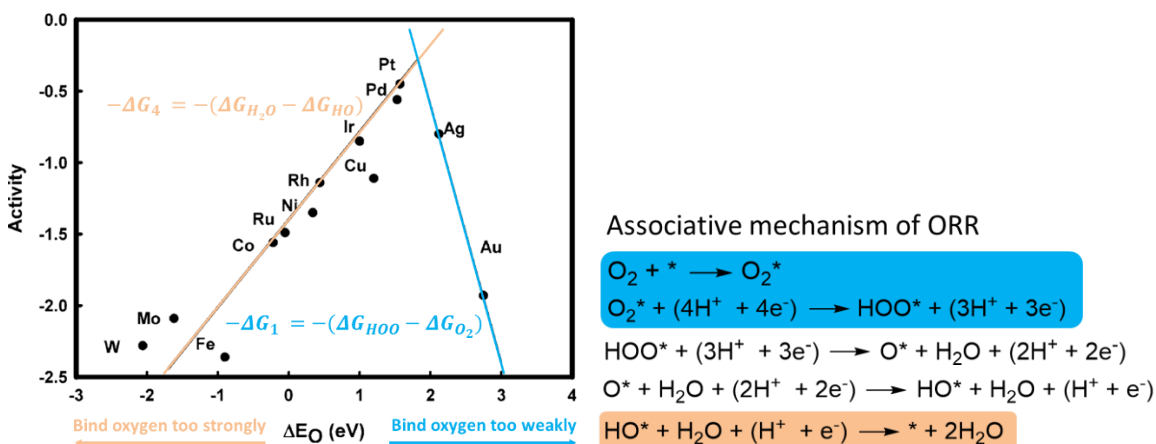
Figure 1.5 Trends in oxygen reduction activity plotted as a function of the oxygen binding energy (ΔE_O). The activcity defined as the negative change of the free energy, $-\Delta G$.[6] Copyright (2004) American Chemical Society, used with permission.

In 2009, Dai first found the doped nitrogen in carbon frameworks could significantly improve the ORR activity of carbon nanotube in alkaline electrolyte, with formation of water as main product through the 4-electron transfer pathway.[15] Although, the intrinsic ORR activity of N-doped carbon materials is underperformed to PGM catalyst, the heteroatom doped carbon materials were considered as a promising alternative to replace the conventional PGM for ORR. Besides nitrogen, other elements, such as S, B and P, etc., have been also incorporated into the carbon framework and exhibited remarkable ORR performances. To understand the heteroatom effects on carbon material for ORR activity promotion, DFT calculations were used to investigate the energy barrier change for rate-determining step of ORR. For each reaction step, the system energy decreases accordingly, indicating that the four-electron transformation reaction takes place spontaneously. The catalytic active sites on the N-graphene depend on spin density distribution and atomic charge distribution. The substituting nitrogen atoms introduce no-pair electrons to the

graphene and changes the atomic charge distribution on it. Generally, the carbon atoms that possess highest spin density are the active sites. If the negative value of spin density is small, the carbon atoms with large positive atomic charge density may act as the active sites.[16] Consequently, different non-metallic elements were incorporated into carbon framework to fabricate the heteroatom doped metal-free ORR catalysts, and the dual doped and tri-doped carbon materials were even investigated. As compared to the PGM catalysts, the metal-free carbon materials feature the low cost, outstanding electrocatalytic ORR activity, and the robust stability in fuel cell and rechargeable metal-air batteries. In the absence of PGM, the metal-free catalysts display no poisoning issue when serving as a cathode ORR catalyst in alcohol fuel cell. Further the severe performance degradation, ascribing to the nanoparticle agglomeration, was also suppressed.

1.6 The mechanism and application of electrocatalytic oxygen evolution reaction (OER)

Oxygen evolution reaction (OER), as the reversed reaction of ORR, is the process of generating molecular oxygen through electrochemical oxidation of water. OER plays a key role in a number of important energy conversion and storage processes, such as rechargeable metal-air batteries (charging mode), and water electrolyzers. However, a large overpotential is required to drive the sluggish OER to be downhill, thereby decreasing the efficiency of energy conversion in rechargeable metal-air batteries, and severely limiting the performance of water electrolyzer. In water splitting reaction, H_2 is generated at the cathode and oxygen is evolved at the anode side, and the reaction mechanism can be written as following. Since the hydrogen binding is more weakly than oxygen on metal surfaces, the hydrogen evolution under both acidic and alkaline environment is much faster than

OER. Therefore, the OER has been considered as the rate limiting for the water splitting process.[17] The reaction pathways are shown as follows:

Table 3 Thermodynamic electrode potentials of electrochemical O_2 evolution reaction. (Thermodynamic electrode potential is cited from Ref.26)

Electrolyte	OER	Thermodynamic electrode potential at standard conditions / V vs. SHE
Acidic aqueous solution	$2H_2O \longrightarrow O_2 + 4H^+ + 4e^-$	1.229
Alkaline aqueous solution	$4OH^- \longrightarrow O_2 + 2H_2O + 4e^-$	0.401

To obtain an efficient elctrocatalyst for OER, Nørskov and his co-workers made a model that representing the catalyst activity by using elementary step free energy change. They first investigated the OER activity on noble metal surfaces, e.g. Pt(111) and Au(111), because such noble metals exhibit promising activity for ORR. However, they found the huge overpotential is required, and the OER could start at around 1.8 V on both Pt and Au electrode. This high potential requirement should be attributed to difficult step that converting HO* to adsorbed O, as well as further oxidation to form adsorbed OOH. Furthermore, it was found that a stable oxygen layer could be formed from dissociation of water on the metal surface at lower potential (lower than OER occurred potential), and only after the surface has oxidized sufficiently to make this step slower than the formation of adsorbed O, will oxygen evolution start. In other words, the oxygen layer has to be formed to facilitate the oxygen evolution taking place on an oxidized metallic surface. Therefore, the metal oxides were investigated (e.g. RuO_2, IrO_2). Rossmeisl et.al found that the rutile-type (110) surfaces of RuO_2 and IrO_2 are highly effective for OER, due to the moderate ability for binding of oxygen (not too strong or too weak).[17, 18] As shown in **Figure 1.5**,

strong and weak O* binding on the oxide surfaces, the OER activity is limited by the OOH*

and O* formation step, respectively. Thus, the RuO_2 and IrO_2, locating around the volcano

peak position, exhibit promising OER activity with low overpotential required. Based on

the results of discussed theoretical analysis above, a material with a little stronger oxygen

binding ability is predicted to have a higher catalytic activity for OER than that of RuO_2,

and this opens a new dimension in rational metal oxide OER catalysts design.
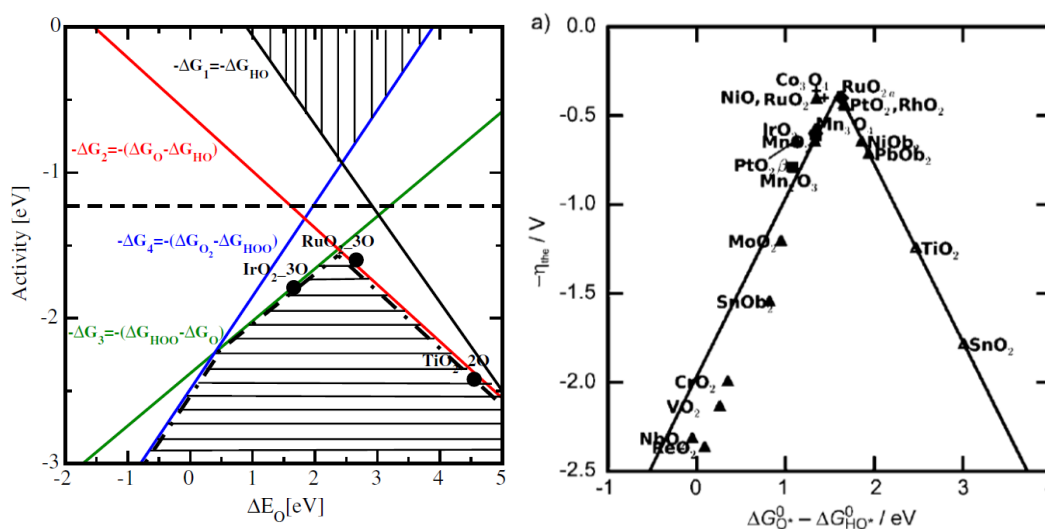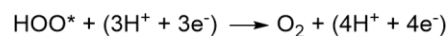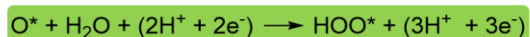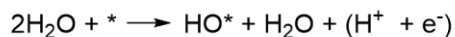
Figure 1.6 Trends in oxygen evolution activity plotted as a function of the oxygen binding energy (ΔEo). The activcity defined as the negative change of the free energy, -ΔG.[18-19] Copyright (2006) Elsevier B.V. (left), Copyright (2011) WILEY-VCH Verlag GmbH & Co. KGaA, Weinheim, (right), used with permission.

In addition to RuO_2 and IrO_2, other rutile oxides were investigated by using same model

for DFT calculation, such as Mn_xO_y, Co_3O_4, and NiO.[19] Rossmeisl and his co-workers

reported that many transition metal oxides (e.g. Co, Mn, and Ni,) have similar oxygen

binding ability as compared to the RuO_2 and IrO_2, and could exhibit promising activity for

OER (**Figure 1.5**), these modeling predictions have been experimentally confirmed by the remarkable OER activity obtained over Co_3O_4 thin film, and Co_3O_4 nanoparticles with low overpotential required. However, the poor stability of non-noble transition metal oxides harshly hinders their applications for OER in acidic environment, and the overpotential could gradually increase during oxygen evolution. Only RuO_2 and IrO_2 were found to be stable in acidic media, whereas the high cost and scarcity of such noble metal still far from satisfactory. Conversely, Ni, Co and Mn, etc, non-noble transition metal oxides exhibit a robust stability in alkaline media, and even show smaller required overpotential as compared to that of IrO_x and RuO_x, resulting from the oxidation of IrO_x to water-soluble IrO_4^{2-} or other solvated Ir(VI) ions in alkaline.[20] Therefore, the non-noble metal oxides were extensively investigated for OER application in alkaline environment.

Although the theoretical calculation can be used to guide rational design of efficient OER catalysts, the real experimental studies suggest that the electrocatalytic OER activity could be significantly affected by many other factors, such as morphology, crystallinity, and exposed surface area, etc. Among the non-noble transition metal oxides, the nickel oxide (NiO_x) has the most complicated composition, including diverse oxidation states from 2.0 to 3.67 under positive applied potential, and the different structure could significantly change the ability for oxygen binding, thereby exhibiting completely different OER performance. It has been reported that the Ni oxidation states could be spontaneously changed during the electrode aging without any applied potential, and the specific Ni oxidation state could be maintained at a certain potential, featuring a tunable OER activity originated from different Ni oxidation states.[21] To tune the metal oxidation state, bi-metal was introduced, such as Fe, and Co, to form bimetallic oxides with more complex

15

configurations. Pletcher and his co-workers demonstrated the $NiCo_2O_4$ and $NiFe(OH)_2$ on nickel form, which exhibit about 200 mV overpotential for OER.[22] Mary et al, also introduced the Fe into Ni oxide thin film, and they found the Fe could significantly promote the OER activity of Ni oxide.[23] On the other hand, Suntivich et al. reported the approach to synthesize the perovskite oxide as highly active OER catalysts, and the benefits of $A_{1-x}A'_xB_yB'_{1-y}$ structure induce at least an order of magnitude higher intrinsic activity as compared to the state-of-the-art IrO_2 for OER in alkaline media.[24] Recently, the elements of W, whose highest oxidation state is a structurally versatile coordination host, was introduced into rutile oxide system to tune the binding energy of oxygen, and the synthesized FeCoW gel materials show the highest OER activity among all previously investigated catalysts.[25]

1.7 The mechanism and application of electrocatalytic hydrogen oxidation and evolution reaction (HOR/HER)

Hydrogen oxidation and evolution reaction (HOR/HER), as the counter reaction coupled with ORR and OER, are also extensively investigated in the energy storage and conversion devices, e.g. fuel cells and water electrolyzers. As compared to ORR and OER, HOR and HER have a much faster kinetics, and exhibit several order magnitude larger exchange current density than that of ORR and OER. Therefore, the HOR and HER become more reversible, and a much smaller overpotential is required to delivery enough current in the application of fuel cells and water electrolyzers. The reaction pathways of HOR/HER in acidic and alkaline media are shown as following.

Table 4 Thermodynamic electrode potentials of electrochemical H_2 oxidation and evolution reaction.[27]

Electrolyte	HOR/HER	Thermodynamic electrode potential at standard conditions / V vs. SHE
Acidic aqueous solution	$H_2 \longleftrightarrow 2H^+ + 2e^-$	0.000
Alkaline aqueous solution	$H_2 + 2OH^- \longleftrightarrow 2H_2O + 2e^-$	-0.826

Although, the HOR and HER contribute a related smaller overpotential cost in energy storage and conversion devices, the Pt-based catalysts are still required, and considered as the most effective catalyst toward HOR/HER in both acid and base electrolytes. As the discussion in 1.2 section, the hydroxide exchange membrane fuel cells, featuring non-noble metal catalysts employment, better catalysts stability, and lower system cost, is considered as the most promising replacement of PEM technologies. However, the activity of HOR/HER on Pt catalyst was found to be two magnitude lower in alkaline than those in acidic electrolyte, and Pt exhibits a poor capability to tolerate CO poisoning. Therefore, the study to find a highly efficient and cost-effective catalyst toward HOR/HER in base is highly desirable.

To investigate the activity of HOR/HER, the exchange current density (i_o) of HOR/HER on different catalyst were measured (using simple Bulter-Volmer equation) and correlated to calculated hydrogen chemisorption energy per H atom, as shown in **Figure 1.6**.[27] It is noted that both Heyrovsky and Volmer step were found to be the rate limiting step and reported in previous work, respectively.

$$H_2 + * \longleftrightarrow 2H^* \text{ (Tafel step)}$$

$$H_2 + OH^- + * \longleftrightarrow H^* + e^- + H_2O \text{ (Heyrovsky step)}$$

$$H^* + OH^- \longleftrightarrow H_2O + e^- + * \text{ (Volmer step)}$$
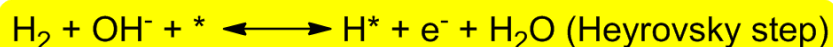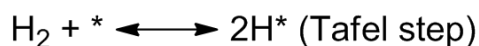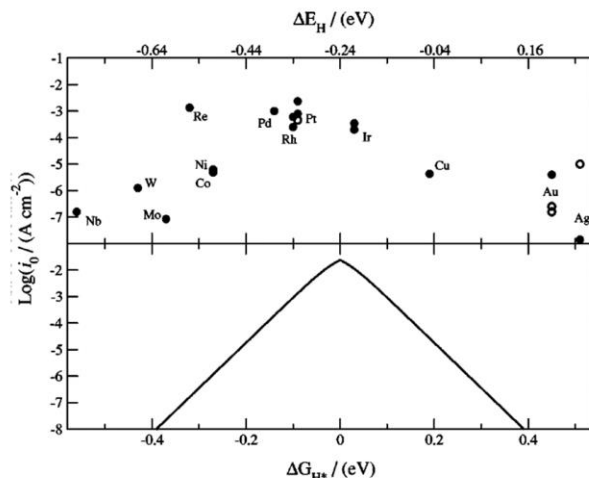
Figure 1.7 (top) Experimentally measured exchange current, $\log(i_0)$, for hydrogen evolution over different metal surfaces plotted as a function of the calculated hydrogen chemisorption energy per atom, ΔE_H (top axis). Single crystal data are indicated by open symbols. (bottom) The result of the simple kinetic model now plotted as a function of the free energy for hydrogen adsorption, $\Delta G_{H^*} = \Delta E_H + 0.24$ eV.[27] Reprinted with permission from J. Electrochem. Soc., 152, J23 (2005). Copyright 2003, The Electrochemical Society, used with permission.

From **Figure 1.6**, it has been found that Pt is very close to the volcano peak, indicating the most optimal hydrogen binding energy (HBE), thereby exhibiting the highest HOR/HER activity. In addition, many investigations were conducted on monometallic catalysts of Pd, Rh and Ir due to their acceptable HBE. However, the measured exchange current density of listed catalysts was found to be only 1/4 of that of Pt (I_o, Pt > Ir > Rh > Pd), which suggests a poor activity of HOR/HER.[28] To optimize the HBE of HOR/HER catalysts, the second metal was incorporated into noble metal system to form PtM, IrM, or PdM alloy or core-shell structured materials. It is expected that the second metal could tune the electronic structure of primary metal, so as adjusting the HBE of catalyst. For example, if we introduce Ag into Pt system, and the HBE of Pt surface could be weaken and close to volcano peak, thereby exhibiting higher HOR/HER activity. In addition, the bimetallic

HOR/HER catalysts always display good tolerance toward CO due to the second element incorporation. Bonnefont et al. introduced Au to weaken the HBE of Pd, and obtained acceptable HOR performance.[29] Alia et al. also demonstrate a Pd coated Cu nanowire as the highly efficient HOR catalyst in alkaline.[30]

Recently, Markovic and his co-worker theoretically reported that the HOR electrocatalytic activity of catalysts (Ir is more oxophilic than Pt and Au) is positively proportional to their oxophilicity, and many noble metal-based alloys with higher oxophilicity as compared to pure Pt were investigated.[31] However, such oxophilicity effect was seriously challenged. Gasteiger and co-workers researched the catalyst HOR activity by measuring their exchange current, i_o, and they found the more oxophilic Ir/C exhibits much lower HOR activity as compared to Pt/C and Pd/C.[28] In addition, Zhuang's group and Yan's group studied the oxophilicity effect on noble metal-based alloy, and claimed that the high HOR activity of PtRu and Pd coated Cu nanowire should be attributed to the optimized hydrogen binding energy (HBE) as opposed to an oxophilicity effect.[30, 32]

Consequently, the rational design of HOR/HER catalyst is highly desired and guided by Norskov's volcano plot. Although, monometallic Pd shows an inferior activity toward HOR/HER due to the strong HBE and H_2 permeability (not discussed), the second metal should be significantly weaken the HBE of PdM, which provide a grateful potential to fabricate a highly efficient, robust and cost-effective HOR/HER catalyst in base electrolyte as the alternatives to Pt materials.

1.8 Research Goals and Significances

My Ph.D research is focused on the rational design and investigation of advanced electrocatalysts toward ORR, OER, HOR, and HER with a promising activity and durability employed in practical energy storage and conversion applications, e.g. fuel cells, water electrolyzers, and rechargeable metal-air batteries. My research strategy is to understand the mechanisms of listed reactions first, followed by catalyst rational design, and finally employ the self-synthesized catalysts in fuel cells and water electrolyzers (coupled HOR&ORR, and HER&OER) to investigate their corresponding activity on practical energy storage and conversion devices. In **Chapter 3**, the N- and S- dual doped mesoporous carbon materials (N-S-CMK-3) were rationally synthesized serving as electrocatalytic ORR catalysts, featuring the high surface area with highly organized hierarchical mesoporous structures, which could desirably facilitate the diffusion of O_2 fuel. This N-S-CMK-3 exhibits remarkable ORR activity and durability in direct alcohol fuel cells (alkaline environment). Therefore, the synergistic effect of doped N and S atoms to ORR activity of carbon material was investigated to explain the promotion of ORR activity with N and S atoms incorporation. **Chapter 4**, carbon supported amorphous NiFe nanoparticles were rationally synthesized as highly active OER catalysts, and exhibited promising OER activity with remarkable durability for long-term electrocatalytic OER tests. In my future work, I would like to rationally synthesize the ORR/OER bifunctional catalysts as hybrid of doped carbon and NiFe materials insitu grown on carbon fiber as a flexible oxygen electrode, which is expected to show promising performance electrocatalytic ORR and OER in metal-air batteries and fuel cells. **Chapter 5** introduces the bcc structured PdCu nanoparticles as the highly active HOR catalyst, and elucidate the crystalline structure transformation effect on significantly enhanced HOR activity in

alkaline electrolyte, which was investigated by using in-situ high energy x-ray diffraction characterization and further confirm density functional theory calculation.

1.9 References

1.   BP Energy Outlook 2035. **2015**.

2.   BP Energy Outlook 2016 edition. **2016**.

3.   Balat, M., Potential importance of hydrogen as a future solution to environmental and transportation problems. *Int. J. Hydrog. Energy.,* **2014,** *29*, 573-588.

4.   Alotto, P.; Guarnieri, M.; Moro, F., Redox flow batteries for the storage of renewable energy: A review. *Renew. Sust. Energ. Rev.,* **2014,** *29*, 325-335.

5.   Dunn, B.; Kamath, H.; Tarascon, J. M., Electrical Energy Storage for the Grid: A Battery of Choices. *Science,* **2011,** *334*, 928-935.

6.   Bruce, P.; Freunberger, S.; Hardwick, L.; Tarascon, J.-M., $Li–O_2$ and Li–S batteries with high energy storage. *Nat. Mater.,* **2011,** *11*, 19-29.

7.   Norskov, J. K.; Rossmeisl, J.; Logadottir, A.; Lindqvist, L.; Kitchin, J. R.; Bligaard, T.; Jonsson, H., Origin of the overpotential for oxygen reduction at a fuel-cell cathode. *J Phys Chem B* **2004,** *108*, 17886-17892.

8.   Stamenkovic, V.; Mun, B. S.; Mayrhofer, K. J. J.; Ross, P. N.; Markovic, N. M.; Rossmeisl, J.; Greeley, J.; Norskov, J. K., Changing the activity of electrocatalysts for oxygen reduction by tuning the surface electronic structure. *Angewandte Chemie-International Edition,* **2006,** *45*, 2897-2901.

9.   Chen, W.; Kim, J.; Sun, S.; Chen, S., Electrocatalytic Reduction of Oxygen by FePt Alloy Nanoparticles. *The journal of physical chemistry. C,* **2008,** *112*, 3891-3898.

10.   Yano, H.; Kataoka, M.; Yamashita, H.; Uchida, H.; Watanabe, M., Oxygen reduction activity of carbon-supported Pt-M (M = V, Ni, Cr, Co, and Fe) alloys prepared by nanocapsule method. *Langmuir,* **2007,** *23*, 6438-6445.

11.   Huang, X. Q.; Zhao, Z. P.; Cao, L.; Chen, Y.; Zhu, E. B.; Lin, Z. Y.; Li, M. F.; Yan, A. M.; Zettl, A.; Wang, Y. M.; Duan, X. F.; Mueller, T.; Huang, Y., High-performance transition metal-doped Pt3Ni octahedra for oxygen reduction reaction. *Science,* **2015,** *348*, 1230-1234.

12.   Brankovic; Adzic, R. R.; Adžić, R. R.; Brankovic, S. R.; Wang, J. X.; Adžić, R. R., Metal monolayer deposition by replacement of metal adlayers on electrode surfaces. *Surf Sci,* **2001,** *474*, L173-L179.

13.   Adzic, R. R.; Zhang, J.; Sasaki, K.; Vukmirovic, M. B.; Shao, M.; Wang, J. X.; Nilekar, A. U.; Mavrikakis, M.; Valerio, J. A.; Uribe, F., Platinum monolayer fuel cell electrocatalysts. *Top Catal.,* **2007,** *46*, 249-262.

14.   Bashyam, R.; Zelenay, P., A class of non-precious metal composite catalysts for fuel cells. *Nature,* **2006,** *443*, 63-66.

15.   Wu, G.; More, K.; Johnston, C.; Zelenay, P., High-Performance Electrocatalysts for Oxygen Reduction Derived from Polyaniline, Iron, and Cobalt. *Science,* **2011,** *332*, 443-447.

16.   Gong, K. P.; Du, F.; Xia, Z. H.; Durstock, M.; Dai, L. M., Nitrogen-Doped Carbon Nanotube Arrays with High Electrocatalytic Activity for Oxygen Reduction. *Science,* **2009,** *323*, 760-764.

17.   Zhang, L. P.; Xia, Z. H., Mechanisms of Oxygen Reduction Reaction on Nitrogen-Doped Graphene for Fuel Cells. *J. Phys. Chem. C,* **2011,** *115*, 11170-11176.

18.   Rossmeisl, J.; Logadottir, A.; Norskov, J. K.; Nørskov, J. K., Electrolysis of water on (oxidized) metal surfaces. *Chemical physics,* **2005,** *319*, 178-184.

19.   Rossmeisl, J.; Rossmeisl, J.; Zhu, H.; Zhu, H.; Norskov, J. K.; Nørskov, J. K., Electrolysis of water on oxide surfaces. *J. Electroanal Chem,* **2007,** *607*, 83-89.

20.   Man, I. C.; Su, H.-Y.; Calle-Vallejo, F.; Hansen, H. A.; Martínez, J. I.; Inoglu, N. G.; Kitchin, J.; Jaramillo, T. F.; Nørskov, J. K.; Rossmeisl, J., Universality in Oxygen Evolution Electrocatalysis on Oxide Surfaces. *ChemCatChem,* **2011,** *3*, 1159-1165.

21.   McCrory, C. C. L.; Jung, S.; Peters, J. C.; Jaramillo, T. F., Benchmarking Heterogeneous Electrocatalysts for the Oxygen Evolution Reaction. *J. Am. Chem. Soc.,* **2013,** *135*, 16977-16987.

22.   Lyons, M. E. G.; Brandon, M. P., The Oxygen Evolution Reaction on Passive Oxide Covered Transition Metal Electrodes in Aqueous Alkaline Solution. Part 1-Nickel. *Int. J. Electrochem Sc.,* **2008,** *3*, 1386-1424.

23. Li, X. H.; Walsh, F. C.; Pletcher, D., Nickel based electrocatalysts for oxygen evolution in high current density, alkaline water electrolysers. *Phys Chem Chem Phys,* **2011,** *13*, 1162-1167.

24. Louie, M. W.; Bell, A. T., An Investigation of Thin-Film Ni-Fe Oxide Catalysts for the Electrochemical Evolution of Oxygen. *J. Am. Chem. Soc.,* **2013,** *135*, 12329-12337.

25. Suntivich, J.; May, K. J.; Gasteiger, H. A.; Goodenough, J. B.; Shao-Horn, Y., A Perovskite Oxide Optimized for Oxygen Evolution Catalysis from Molecular Orbital Principles. *Science,* **2011,** *334*, 1383-1385.

26. Bo, Z.; Xue, L. Z.; Oleksandr, V.; Riccardo, C.; Michal, B.; Max, G. M.; Li, L. H.; Ji, X. X.; Min, L.; Li, R. Z; F. Pelayo, G. A.; Cao, T. D.; Feng, J. F.; Ming, J. Y.; Emre Y.; Ning, C.; Tom, R.; Peng, F. L.; Yu, H. L.; Phil, D. L.; Alyf, J.; Huolin, L. X.; Hua, G. Y.; Aleksandra, V.; Edward, H. S.; Homogeneously dispersed, multimetal oxygen-evolving catalysts. *Science,* **2016,** *352*, 333-337.

27. PEM Fuel Cell Electrocatalysts and Catalyst Layers Fundamentals and Applications, Zhang, J (Ed.), 2008.

28. J. K. Norskov, T. Bligaard, A. Logadottir, J. R. Kitchin, J. G. Chen, S. Pandelov, U. Stimming, Trends in the Exchange Current for Hydrogen Evolution. *J. Electrochem. Soc.,* **2005,** *152*, J23-J26.

29. J. Durst, C. Simon, F. Hasche, H. A. Gasteiger, Hydrogen oxidation and evolution reaction kinetics on carbon supported Pt, Ir, Rh and Pd electrocatalysts in acidc media. *J. Electrochem. Soc.,* **2015,** *122*, F190-F203.

30. A. Bonnefont, A. N. Simonov, S. N. Pronkin, E. Yu. Gerasimov, P. A. Pyrjaev, V. N. Parmon, E. R. Savinova, Hydrogen electrooxidation on PdAu supported nanoparticles: An experimental RDE and kinetic modeling study. *Catalysis Today,* **2013,** *202*, 70-78.

31. S. M. Alia, Y. S. Yan, Palladium coated copper nanowires as a hydrogen oxidation electrocatalyst in base. *J. Electrochem. Soc.,* **2015,** *162*, F849-F853

32. JD. Strmcnik, M. Uchimura, C. Wang, R. Subbaraman, N. Danilovic, D. Vliet, A. P. Paulikas, V. R. Stamenkovic, N. M. Markovic, Improving the hydrogen oxidation reaction rate by promotion of hydroxyl adsorption. *Nature chemistry,* **2013,** *5*, 300-306.

33.   Y. Wang, G. W. Wang, G. W. Lin, B. Huang, J. Pan, Q. Liu, J. J. Han, L. Xiao, J. T. Lu, L. Zhuang, Pt-Ru catalyzed hydrogen oxidation in alkaline media: oxophilic effect or electronic effect?. *Energy & Environmental Science,* **2014,** *58*, 177-181.

CHAPTER 2. EXPERIMENTAL DETAILS

2.1 Electrochemical cell setups

2.1.1 Three-electrode half-cell system with rotating disk electrode (RDE) and rotating ring-disk electrode (RRDE)

To investigate the ORR and OER reactions that occur at specific electrode, the three-electrode system was proposed, and the experimental cell is called as three-electrode half-cell. As shown in **Figure 2.1**, three different electrodes normally consist of a working, counter and referent electrode. The interested reaction will be happened at the surface of working electrode under specific applied potential, while the counter electrode could serve as the electron balancer to protect the normal running of interested reaction (on working electrode) with target reaction rate, and the reference electrode could work as a standard to control the applied potential on working electrode.
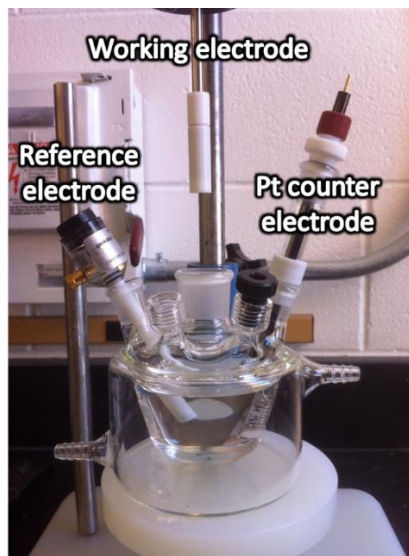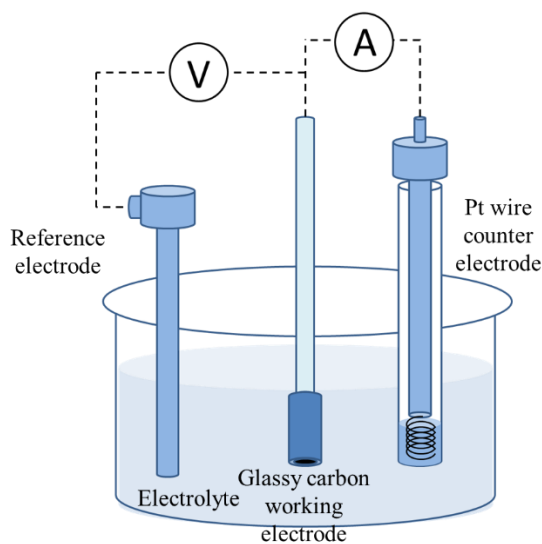
Figure 2.1 Structrue of three-electrode half-cell system.

The reference electrode of a known potential, which has the ideal nonpolarizability, usually locates near the working electrode. A high input impedance is employed to protect the negligible current passing through the reference electrode. Consequently, the potential

difference between working and reference electrode will not change with the system current varying, and the applied potential on working electrode will be controlled versus the potential on reference electrode. Common reference electrodes include 1) Standard hydrogen electrode (SHE); 2) Reversible hydrogen electrode (RHE); 3) Silver / Silver Chloride electrode (Ag/AgCl); 4) Mercury / Mercury oxide electrode (Hg/HgO).

As compared to the reference electrode, the counter electrode should isolate from the main test solution chamber by using a fritted glass tube, and the cation or anion in solution can be exchanged through the porous glass bottom. The platinum (Pt) and graphite carbon are the most common counter electrode materials, due to their high oxidation potential and robust stability in both acidic and alkaline environment.

The working electrode is more complex to be fabricated, due to the diversity of investigated materials (nanomaterial, film, bulk, etc.). Bulk materials could directly serve as working electrode, while the nanomaterials and films could be deposited on conductivity substrate to compose a working electrode. In order to test ORR and OER activity of specific materials, the glassy carbon imbedded rotating disk electrode (GC-RDE) was used as working electrode in my three-electrode half-cell test system. In the presence of rotation, the spinning disk drives the fluid at its surface along with it and flings the solution outward from the center in a radial direction (**Figure 2.2**), which is caused by centrifugal force. Consequently, the reactant (O_2 for ORR, OH- for OER) will be supplied constantly under the fixed electrode rotation rate, and offer the most important test condition for electrochemical properties characterization for ORR and OER. Besides the RDE, there is another rotating ring-disk electrode (RRDE) that could be also used for ORR and OER electrochemical characterization. An extra Pt ring electrode was surround to disk electrode,

and the different potential can be simultaneously applied on disk and ring electrode, respectively, building up a system to insitu analyze the product generated from disk electrode by using collected ring electrode current. (The structure of RDE and RRDE is shown in **Figure 2.2**)
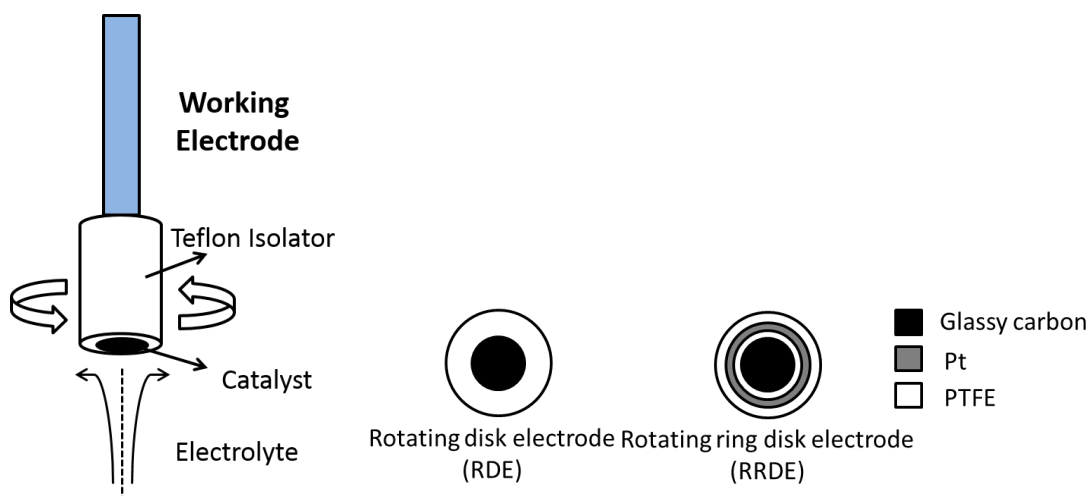
Figure 2.2 Shematic resultant flows for rotating disk electrode (RDE) and rotating ring-disk electrode (RRDE).

2.1.2 Three-electrode H-type cell system

On the other hand, the H-type cell is also consisted of working, counter and reference electrode, whereas the counter electrode is completely isolated from the working and reference electrode chamber by using ion-exchange membrane (**Figure 2.3**). The cation (e.g. H^+) or anion (e.g. OH^-) could selectively diffuse through the membrane to the other chamber, and react at the other electrode surface.
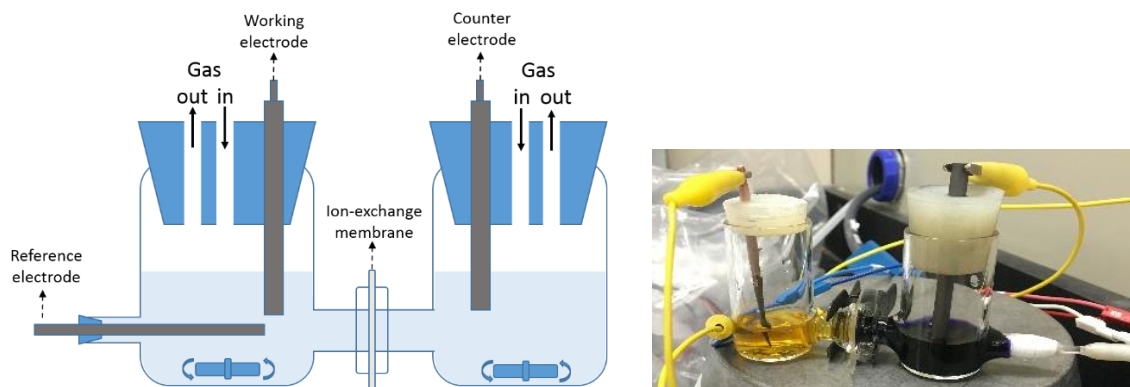
Figure 2.3 Shematic of three-electrode H-type cell system.

2.1.3 Anion-exchange membrane fuel cell (AEMFC)

The performance of electricity generation of chemicals and the corresponding chemical energy conversion efficiency were investigated by a Scribner fuel cell test system (850e). The core part of fuel cell test station is mass flow controller and humidifier. The target gas will flow through mass flow controller to humidifier, and further supply to fuel cell hardware after humidifying under specific dew point. The fuel cell hardware consists of stainless steel end plates, graphite flow channel plates, current collector. The membrane electrode assembly (MEA), which is mechanically sandwiched anode electrode, membrane, and cathode electrode, was fabricated based on the typical procedure discussed at section 2.2.2. As shown in **Figure 2.4**, the fuel cell hardware was attached, and the MEA is located at the center of cell for fuel cell performance characterization. The H_2 oxidation / alcohol oxidation and O_2 reduction reaction will be happened at anode and cathode electrode surface, respectively. The performance of electricity generation from AEMFCs was evaluated by a polarization scan at various cell temperatures and backpressure.
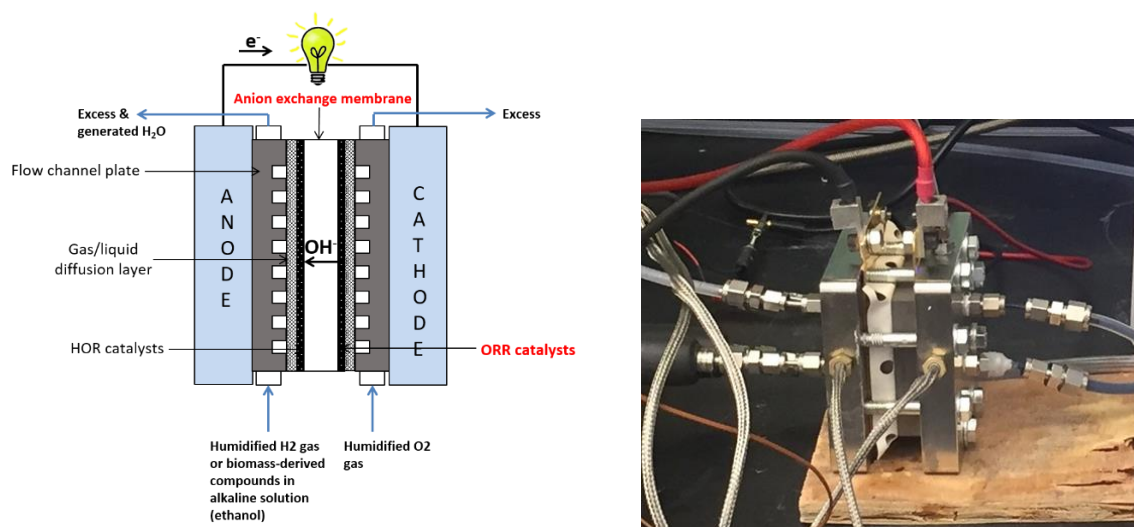
Figure 2.4 Shematic of anion-exchange membrane fuel cell (AEMFC).

2.2 Electrode preparation

2.2.1 Rotating disk electrode (RDE) and Rotating ring disk electrode (RRDE)

The RDE and RRDE are the most common working electrode used in three-electrode half-cell system, as shown in **Figure 2.5**. The disk electrode can directly serve as electrode (e.g. glassy carbon disk, gold disk, silver disk), or work as catalysts substrate. The investigated catalysts can be deposited on disk surface to fabricate the working electrode. Prior to catalyst deposition, the disk was polished using 1.0 µm and then 0.05 µm alumina suspension to obtain a mirror like clean surface. A 1.0-2.0 mg ml^{-1} solution of catalyst ink was prepared by dispersing investigated catalysts (e.g. N-S-CMK-3 in Chapter 3) in mixture of iso-propanol and 5 wt% Nafion solution (one-propanol : Nafion = 9 : 1), followed by ultrasonication until no aggregation was visible. Then, 10-30 µL of ink was dropped onto the surface of disk, and a uniform catalyst film was obtained after 30 min ambient temperature drying in air.
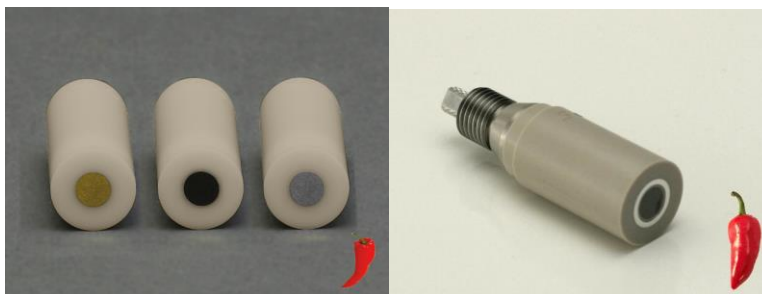
Figure 2.5 Graphic of rotating disk electrode (RDE) and rotating ring-disk electrode (RRDE). Copyright Pine Research Instrumentation (www.pineresearch.com), used with permission

2.2.2 Membrane electrode assembly (MEA)

MEA was a sandwiched-like assembly of anode electrode, solid ion-selective membrane, and cathode electrodes. The anode and cathode electrode were fabricated by coating the catalysts-ionomer mixture on gas/liquid diffusion layer. A catalyst ink containing 95 wt% of as-prepared catalyst and 5 wt% of Nafion was manually sprayed on a carbon cloth gas/liquid diffusion layer. With the heating treatment, the catalysts-ionomer was remained on the carbon cloth, while the ink solvent (e.g. iso-propanol) was fully evaporated, and the uniform catalyst-ionomer layer was successfully coated on gas/liquid diffusion layer. The MEA was then assembled by mechanically sandwiching anode and cathode electrode on separate side of ion-selective membrane (**Figure 2.6**).
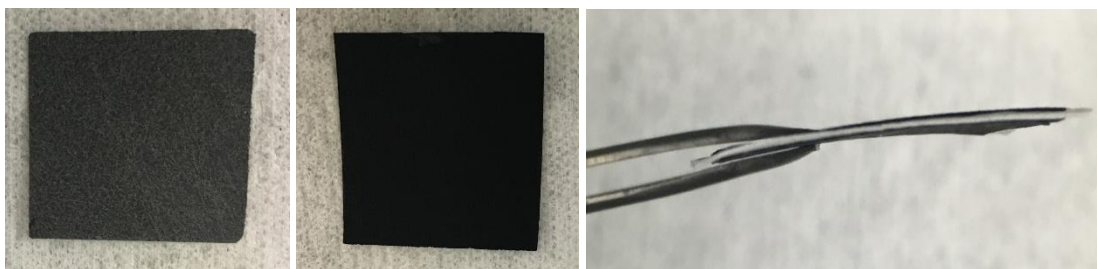
Figure 2.6 Graphic of carbon fiber paper (gas/liquid diffusion layer), electrode fabricated by catalysts coating on carbon fiber paper, and membrane electrode assembly (MEA).

2.3 Advanced catalysts synthesis

2.3.1 Wet-chemistry based synthesis for nanostructured catalysts [27, 28]

The electrocatalytic performance of electrode for oxygen reaction (both OER and ORR) is significantly affected by electrochemical surface area (ECSA) with corresponding exposed active sites. In terms of bulk electrode, the insufficient surface area could be far from satisfactory to drive the reaction reaching a practical usable level. Therefore, nanoscaled materials become more attractive, featuring high surface area with controllable crystal facets exposing. In addition, the nanoscaled metallic catalysts could exhibit unique catalytic properties that are quite different from their bulk of counter parts due to the optimized electronic properties. Subsequently, development of accurate methods for synthesizing efficient nanoscaled catalysts has been extensively investigated in the last few decades, and numerals researches have been focused on the synthesis of nanomaterials with tailored size, shape (0D particle,1D rod, wire, etc.) and crystalline structure.

Wet-chemical route, so-called "nanocapsule", have emerged as a promising approach to accurately control the size, shape, structure and crystal facets of nanoscaled metal materials. The normal synthesis process of nanocapsule method consists of several steps, including metal salt precursor dissolving and mixing with surfactant, metal ion reducing with nucleus generation, metal nucleus growth, as well as metal nanoparticle deposition on substrate (not necessary). The general synthesis scheme is shown in **Figure 2.7**, and the example of carbon supported Pt (Pt/C) nanoparticles synthesis through nanocapsule approach was described.
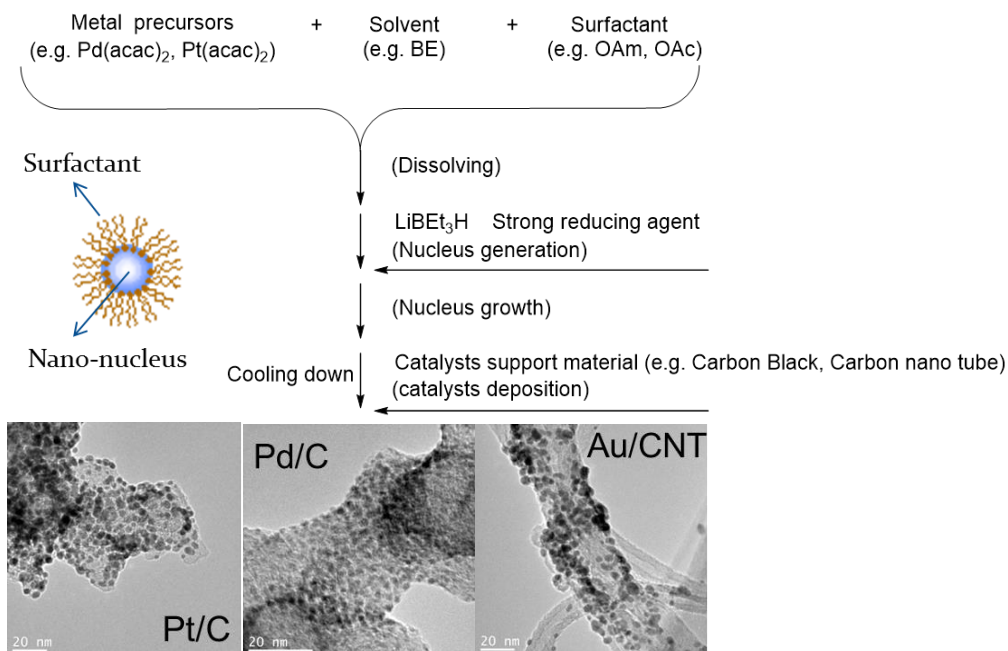
Figure 2.7 General route of organic solvent based wet-chemistry synthesis approaches.

Example: For the preparation of Pt/C (40 wt%), 0.5mmol Pt(acac)₂, 200 µL of oleylamine, and 200 µL of oleic acid were first dissolved in a mixture of 146.3 mg Vulcan XC-72R carbon black and 40 mL of benzyl ether at 60 °C under a N₂ protection. As the temperature was increased to 120 °C, 1.0 mL of LiBEt₃H was quickly injected into the system. The temperature was held for 30 min, and then slowly increased to 180 °C and held for an additional 30 min. After holding, the solution was cooled down to room temperature and collected by filtration, washed with copious ethanol, and dried in vacuum oven at 60 °C overnight.[27]

This wet-chemistry method provides a relatively high temperature condition at which the thermolytic reduction can be achieved. With the so-called "hot-injection" of strong reducing agent, the metal seeds will be generated and further grown to nanoparticle. However, due to the too strong reducing ability of discussed reducing agent (e.g. LiBEt₃H), most of the metal source could be instantly reduced to metal seed after the reducing agent

injection, and the generated morphology and crystalline structure of nanoparticle could be hard to controlled. Therefore, weak reducing agents (e.g. $Fe(CO)_5$, $W(CO)_6$, etc.) are very often to use. Wang et al. used the $Fe(CO)_5$ as weak reducing agent, and obtained the PtFe nanowires and nanorods,[27] whereas only nanoshpere PtFe could be gained when it using $LiBEt_3H$ strong reducing agent. In addition, surfactant is another important role that could significantly change obtained structure of nanomaterials. An example is the formation of Au decahedron in the presence of OAm surfactant, where the lack of the C=C bong in octadecylamine was suggested to limit its coordination with AuCl, thereby more nanospheres were formed.[28]

However, synthesis of metal oxide OER catalysts, such as NiO_x, Co_3O_4, remains a big challenge for as discussed wet-chemistry synthesis method. Although, the synthesized metal could be further oxidized through heat treatment in air or oxygen gas, particle agglomeration issue still inhibits the application of wet-chemical route. In addition, as compared to the noble metal, the non-noble metal, e.g. Ni, Fe, Co, has relatively weak binding force with surfactants, and the lack effective protection mainly causes the aggregation of metal nucleus to form large particles with wide size distribution. Therefore, another synthesis approach, "hydrothermal synthesis", was preferred to directly prepare the metal oxide OER catalysts with specific morphology and crystalline structure.

2.3.2 Hydrothermal synthesis for nanostructured catalysts[29-32]

It is well known that hydrothermal method is a typical solution-based approach, which exploits water or a solvent under elevated temperatures and pressures above its critical point to increase the solubility and reactivity of almost all inorganic substances, thereby permitting the subsequent crystallization of the dissolved material/precursor ions from

solution under these conditions. Compared with the synthesis in the organic solvents, a water-based system should provide a relatively green chemical alternative to the preparation of various nanomaterials because it does not involve toxic organic solvents. The acceptable advantages of this method include easily controllable reaction conditions, the relatively low cost and high yield, the relatively low reaction temperature (in general < 250 °C), easily controlled size, structure and shapes of the products, etc. Furthermore, during the process of hydrothermal reaction, one of the promising and popular strategies of shape and size control is to carefully select an appropriate organic/inorganic additive with functional groups acting as complex agent or structure-directing agent, which has the similar function as the surfactant in wet-chemistry synthesis process.

The example of carbon supported $Ni(OH)_2$ particle synthesis through hydrothermal synthesis approach was described (cited from Ref 33, and used with permission).

Example: In a typical procedure of $Ni(OH)_2$ synthesis, 1 mmol $Ni(NO_3)_2$ $6H_2O$, 4 mmol Na_2CO_3, and 12ml $NH_3·H_2O$, were added into 10 ml of ethylene glycol in a beaker under magnetic stirring. After 10 min of stirring, the mixture changed into a dark blue solution. Afterward, the precursor solution was transferred into a Teflon-lined stainless steel autoclave with a volume of 50 mL. Thermal treatment was performed on the Teflon liner in an electric oven at 170 °C for 16 h. After the autoclave was cooled naturally to room temperature in air, samples were collected and washed by centrifugation at least three times using deionized water and one time using pure ethanol (200 proof). The as-synthesized samples were then dried in a normal oven at 60 °C overnight to remove the absorbed water and ethanol for the subsequent fabrication and characterization.[33]

Varying the organic additive can significantly change the final structure of obtained crystalline materials, and the different solvent with low boiling point (e.g. H_2O, ethanol) could also change the morphology of synthesized catalysts ascribing to the pressure change in autoclave liner. Yan and his co-workers tried to use H_2O, ethanol, and acetone as solvent for $Ni(OH)_x$ synthesis by using hydrothermal synthesis method. Interestingly, only ethanol solvent can generate α-$Ni(OH)_2$ with hollow sphere structure, while H_2O and acetone only can get β-$Ni(OH)_2$ nanoplates, and β-$Ni(OH)_2$ nanoparticles, respectively.[34] On the other hand, Feng et al. was succeeded to synthesize the highly ordered $Ni(OH)_2$ nanoplates in the presence of an ammonia fluoride additives, while the more disordered $Ni(OH)_2$ nanosheets could be obtained without NH_4F in system.

2.4 Physical characterizations

2.4.1 Scanning and transmission electron microscopy (STEM)

JEOL 2100 200 kV scanning and transmission electron microscope (STEM) was employed to characterize the morphology, structure, and composition of catalysts with an operation voltage of 100 to 200 kV. The STEM sample was prepared by dropping diluted as-prepared catalyst ink on carbon film coated Au or Cu grid sample holder. After ink solvent evaporation, the nanoscaled catalysts was uniformly deposited on sample holder, can be used for STEM characterization. The average particle size and dispersion of metal catalysts (e.g. NiFe in Chapter 4) on carbon supporting materials were revealed from STEM images. Histograms of particle size were obtained by randomly measuring over 200 particles from representative regions on STEM images. The crystalline structure was obtained through selected area electron diffraction (SAED) mode on STEM, and the sharp circle in SAED pattern was used for crystal facet determination.

2.4.2 Scanning electron microscopy (SEM)

Quanta 250 field-emission scanning electron microscope (SEM) coupled with the element energy-dispersive X-ray spectrometer (EDS) were empolyed to characterize the catalyst mophology and the surface element distribution with an operation voltage of 5 to 15 kV.

2.4.3 X-ray diffraction (XRD)

XRD patterns of investigated catalysts were collected by Rigaku Ultima IV X-ray diffraction (XRD) with Cu Kα radiation (λ = 1.5406 Å) at a tube current of 44 mA and a tube voltage of 40 kV. A silicon substrate of zero background was used to hold the film of catalysts. The average particle size of crystalline metallic materials (e.g. NiFe in Chapter 5) can be calculated by Debye-Scherrer formula: [35]

$$L = \frac{0.9\lambda_{K_\alpha}}{B_{2\theta}\cos\theta_{max}}$$

where L is the mean crystal size (diameter of nanostructures), $\lambda_{K\alpha}$ is the wavelength of X-ray (1.5406 Å), $B_{2\theta}$ is the full width at half-maximum of the peak, and θ_{max} is the Bragg angle.

And the lattice parameter (α_{fcc}) is calculated by the following equation:[35]

$$\alpha_{fcc} = \frac{\sqrt{2}\lambda_{K_\alpha}}{\sin\theta_{max}}$$

2.4.4 X-ray photoelectron spectroscopy (XPS)

X-ray photoelectron spectroscopy (XPS) with Mg K alpha X-ray (1253.6 eV) (Kratos Amicus/ESCA 3400) was used to determine the heteroatom concentrations and its corresponding status through different binding energy peak. Due to the close binding

energy of the same elements with different valence state, a broad peak could be obtained, which is needed to further split by using CasaXPS software.

2.4.5 Inductively coupled plasma atomic emission spectroscopy (ICP-AES)

ICP-AES was employed to analyze the bulk elements composition of the as-prepared catalysts, as well as the metal loading of the carbon deposited catalysts. A certain amount of catalyst (10 mg) was carefully measured and dissolved in 4.0 ml Aqua Regia (A strong oxidative acid formed by mixing concentrated nitric acid and hydrochloric acid with the volume ratio of 1:3). The solvent was then accurately diluted to 15 ml for the composition analysis.

2.4.6 Raman microscopy

A DXR Raman microscope (Thermo Scientific, Waltham, MA, USA) was used for spectra acquisition with 780 nm excitation at 14 mW laser power, 10× objective, and 50 μm slit aperture (resolution is 4-8 cm^{-1}). The exposure time is 30 s.

2.4.7 Brunauer-Emmett-Teller (BET) specific surface area determination

Brunauer-Emmett-Teller (BET) specific surface area and pore volume of the samples were characterized by using N_2 adsorption/desorption measurement, which was carried out on a Quantachrome Autosorb iQ gas sorption analyzer, and the pore size distribution was calculated based on the NL-DFT model assuming a slit-shape pore structure.

2.5 Electrochemical Characterization

Electrochemical techniques include chronoamperometry (CA), cyclic voltammetry (CV), and linear sweep voltammetry (LSV), etc. CA record current that related to Faradaic reactions undetr constant potential as a function of time. Cyclic voltammetry can be

considered as potential swept from low to high boundaries of multiple cycles with time and the i-E curve is recorded directly. LSV is a single scan of potential that varies linearly with time at a slow scan rate that allows the electrochemical reactions occurring near the electrode approach a quasi-steady state. In addition, because the characterization will be conducted on liquid solution, the electrolyte resistance between the working and reference electrode in three-electrode system should be compensated, thereby the electrochemical impedance spectroscopy (EIS) is necessary prior to other electrochemical properties characterizations. Useful information about electrocatalysts and complicate electrocatalytic reactions can be by deliberately designing the electrochemical experiments and detail discussions will be made in the following.

2.5.1 Electrochemical properties characterization of ORR (Chapter 3)

The ORR performance of the catalyst was investigated by cyclic voltammetry (CV) test, which was performed at 50 mV s^{-1} scan rate after purging the electrolyte with N_2 and O_2 for 30 min respectively, followed by the linear sweep voltammetry (LSV) toward ORR activity evaluation in O_2-saturated electrolyte with 10 mV s^{-1} scan rate at different rotating rate from 2000 rpm to 400 rpm by using RDE. The obtained CV and LSV polarization curves will be used for ORR properties analysis, including, E_{onset} & $E_{1/2}$ determination, electron transfer vale (*n*) calculation, kinetic controlled limiting & mass transfer controlled limiting current density determination, etc.

The overall electron transfer numbers per oxygen molecule involved in the typical ORR process were calculated from the slopes of the Koutecky-Levich plots using the following equations:

38

$$\frac{1}{J} = \frac{1}{J_L} + \frac{1}{J_k} = \frac{1}{B\omega^{1/2}} + \frac{1}{J_k}$$

$$B = 0.2nFC_o(D_o)^{2/3}\upsilon^{-1/6}$$

$$J_k = nFkC_o$$

where J is the measured current density, J_k and J_L are the kinetic and diffusion limiting current densities, ω is the electrode rotating speed in rpm, B is the reciprocal of the slope, n is the number of electrons transferred per oxygen molecule, F is the Faraday constant (96485 C mol^{-1}), D_o is the diffusion coefficient of O_2 in 0.1 M KOH (1.9×10^{-5} cm s^{-1}), v is the kinetic viscosity (0.01 cm^2 s^{-1}), and C_o is the concentration of O_2 (1.2×10^{-3} mol L^{-1}). The constant 0.2 is adopted when the rotating speed is in rpm, and k is the electrontransfer rate constant.

Rotating ring-disk electrode (RRDE) was employed to measure the concentration of HO_2^- intermediate and electron transfer number per oxygen (n) with scanning rate of 10 mV s^{-1} at rotating rate of 1600 rpm. The HO^{2-} intermediated, generated on the surface of disk electrode (0.19625 cm2 geometric surface area), can be immediately oxidized on Pt-ring electrode surface at 0.8 V vs. RHE applied potential. The electron transfer number n and HO_2^- intermediate production percentage (HO_2^- %) were determined as follows:

$$n = 4\times\frac{I_d}{I_d + I_r / N}$$

$$HO_2^-\% = 200\times\frac{I_r / N}{I_d + I_r / N}$$

where I_d is the disk current; I_r is the ring current, and N is the ring current collection efficiency which was determined to be 23%.

2.5.2 Electrochemical properties characterization of OER (Chapter 4)

Electrochemical characterizations and tests were performed in an electrochemical cell. A rotating disk electrode (RDE) and rotating ring disk electrode (RRDE) were used for examination of OER kinetics without interference of mass transfer effects, and for analysis of OER Faradaic efficiency, respectively.

The OER activity of Ni-Fe catalysts was first characterized by using cyclic voltammetry (CV). The 1.0 M KOH electrolyte was deaerated by pure oxygen gas for 30 min prior to each experiment. The surfactant removal was firstly carried out by scanning from -0.8 to 0.65 V (vs. MMO) with 1000 mV s^{-1} scan rate for 50 cycles, followed by catalyst activation in a potential range of 0 to 0.65 V (vs. MMO) with scan rate of 50 mV s^{-1} for 10 cycles. The polarization curves were subsequently obtained using a scan rate of 5 mV s^{-1} between 0 and 0.8 V (vs. MMO).

The Turnover Frequency (TOF) is defined as per total metal atoms including subsurface metal per second, and the equation is shown as follows: which has been widely used in previous works.

$$TOF = \frac{I}{4 \times F \times m}$$

where I is measured current at a certain overpotential; F is the faraday constant with a value of 96485 C mol^{-1}; m is the number of moles of the total active metals drop-casted on the glassy carbon electrode.

This TOF is estimated by assuming all of the active metal atoms in the catalysts drop-casted on the glassy carbon electrode are catalytically active for OER. However, this is a gross underestimate of the real TOF, which should be the lower bound, TOF$_{min}$, because

the porous structure of carbon supporting materials could inhibit the perfect connection between the electrolyte and catalysts, and some of subsurface active material atoms might not be accessible for catalyzing the OER.

The RRDE was employed to measure the OER Faradaic efficiency over the Ni-Fe catalysts with different compositions. The collection efficiency, N, of RRDE was determined by the current ratio between the ring and disk in 0.01 M $K_3Fe(CN)_6$ + 0.1 M KOH electrolyte, which was 23±1%. This result agrees well with 25% collected efficiency calculated according to the geometry of RRDE. Pure nitrogen gas flowed into 1.0 M KOH electrolyte prior to each test for 30 min and remained throughout the electrochemical experiments to purge the system. Because of the low magnitude of ring current, the Pt ring was polished with diamond slurry (1 μm MetaDi Supreme) before the ring current collection in order to minimize the interference of the contaminants. 5 μl of 1 mg ml^{-1} catalyst ink was dropped onto the surface of disk electrode, followed by adding 3 μl diluted Nafion solution (0.05 wt %) on the top. In order to determine the background current of ring electrode, the open circuit potential of OER was applied to the disk electrode where no faradaic reaction occurs, while the Pt ring electrode was held at -0.6 V vs. MMO. The background ring current determined was typically lower than 50 μA. Then, the applied voltage was held at several potentials in the OER kinetic-limited region for 1 min, meanwhile the ring current was collected under -0.6 V vs. MMO.

2.6 References

27.   Wang, C.; Hou, Y.; Kim, J.; Sun, S., A General Strategy for Synthesizing FePt Nanowires and Nanorods. *Angewandte Chemie (International ed.),* **2007,** *46*, 6333-6335.

28.   Ma, Y.; Zeng, J.; Li, W.; McKiernan, M.; Xie, Z.; Xia, Y., Seed-Mediated Synthesis of Truncated Gold Decahedrons with a AuCl/Oleylamine Complex as Precursor. *Adv. Mater.,* **2010,** *22*, 1930-1934.

29.   Li, C.; Lin, J., Rare earth fluoride nano-/microcrystals: synthesis, surface modification and application. *J. Mater. Chem.,* **2010,** *20*, 6831-6847.

30.   Yin, Y.; Alivisatos, A. P., Colloidal nanocrystal synthesis and the organic–inorganic interface. *Nature,* **2005,** *437*, 664-670.

31.   Tao, A.; Habas, S.; Yang, P., Shape Control of Colloidal Metal Nanocrystals. *Small,* **2008,** *4*, 310-325.

32.   Xia, Y.; Xiong, Y.; Lim, B.; Skrabalak, S., Shape-Controlled Synthesis of Metal Nanocrystals: Simple Chemistry Meets Complex Physics? *Angewandte Chemie (International ed.),* **2009,** *48*, 60-103.

33.   Feng, Y. Y.; Zhang, H. J.; Zhang, Y.; Li, X.; Wang, Y., Ultrathin Two-Dimensional Free-Standing Sandwiched NiFe/C for High-Efficiency Oxygen Evolution Reaction. *Acs Appl. Mater. Inter.,* **2015,** *7*, 9203-9210.

34.   Gao, M. R.; Sheng, W. C.; Zhuang, Z. B.; Fang, Q. R.; Gu, S.; Jiang, J.; Yan, Y. S., Efficient Water Oxidation Using Nanostructured alpha-Nickel-Hydroxide as an Electrocatalyst. *J. Am. Chem. Soc.,* **2014,** *136*, 7077-7084.

35.   Zhang, Z. Y.; Xin, L.; Qi, J.; Chadderdon, D. J.; Li, W. Z., Supported Pt, Pd and Au nanoparticle anode catalysts for anion-exchange membrane fuel cells with glycerol and crude glycerol fuels. *Appl Catal B-Environ* **2013,** *136*, 29-39.

CHAPTER 3. N- AND S- DOPED MESOPOROUS CARBON AS METAL-FREE CATHODE CATALYSTS FOR DIRECT BIORENEWABLE ALCOHOL FUEL CELLS[1]

3.1 Introduction

With increasing energy demands, declining petroleum reserves and increasing environmental pressure, having clean, sustainable, reliable and technical viable energy resources is one of the most significant challenges facing human society, industry and the economy.[1,2] Sustainable energy conversion and storage technologies, such as fuel cells, metal-air batteries, etc., attract enormous attention and have been intensively studied and developed given their potential for high energy-conversion efficiency and environmental advantages.[3-6] However, the sluggish oxygen reduction reaction (ORR), one of the half electrochemical reactions occurring at the cathode side, results in significant overpotential even at open circuit voltage operation (>250 mV), and largely limits the fuel cell's working efficiency and output power density.[6, 7] The noble metal-based catalysts, *e.g.* Pt, have been found to be the best ORR catalysts at low temperatures, but they suffer from several serious issues including their limited reserves on the earth, high cost and instability under the fuel cell operation environment.[4,7] For direct alcohol fuel cells, noble metal-based ORR catalysts further have an alcohol poisoning issue, which is originated from the crossover of alcohol fuel from the anode to cathode.[6,8] With the alcohol crossover, electrochemical oxidation of alcohol competes with the ORR at the cathode and results in a mixing potential, thus reducing the fuel cell operating voltage and efficiency. Therefore, there is a clear and urgent need to seek for alternative noble metal-free or even metal-free cathode catalysts

---

[1] The material contained in this chapter was previously published in RSC Journal of Materials Chemistry A, 2016, 4, 83, "N- and S- Doped Mesoporous Carbon as Metal-Free Cathode Catalysts for Direct Biorenewable Alcohol Fuel Cells" by Qiu, Y.†, Huo, J. J.†, Jia, F., Shanks, B. H., Li, W. Z. († *equal contribution*) Reproduced by permission of The Royal Society of Chemistry shown in **Appendix B**

with high ORR activity, low economic cost, robust stability and high tolerance towards alcohol fuels.

One strategy is to lower the noble metal content in the ORR catalysts. Adzic and co-workers reported the underpotential deposition method to fabricate a Pt monolayer on Au and Co.[9, 10] MPt (M=Fe, Co etc.) alloys and core-shell (noble metal core) catalysts were also investigated to reduce the noble metal content.[8, 11] Another strategy is to replace Pt by transition metal macrocycle catalysts prepared through pyrolysis processes. Although these catalysts demonstrated competitive ORR activity relative to Pt, they suffer significant activity loss due to instability of the transition metal in the acid electrolyte.[12] Recently, nitrogen doped carbon has been discovered as a metal-free ORR catalyst in a high pH medium. For example, metal-free nitrogen-doped carbon nanotubes were shown to have remarkable ORR activity and durability.[13] It has been reported that the carbon materials could become non-electron-neutral by incorporating N atoms into the graphitic framework. The electronic property tuning effect of N atoms can significantly change the charge density and spin density of carbon atoms; thus benefiting the adsorption of oxygen and subsequent reduction reaction on carbon.[13, 14] Besides nitrogen, other elements, such as S, B and P, etc., can also be incorporated into the carbon framework as a dopant or co-dopant with N to further enhance the ORR activity based on the synergistic effects between the two dopants.[15-19] Unfortunately, some undesired structures/phases (e.g. boron nitride, BN) could be formed under high temperature annealing conditions, and can significantly lower the ORR activity of the catalysts.[14, 20] Thus, rational choice of dual-dopants and its corresponding precursors play an important role in obtaining high ORR activity. However,

few reports explain the criterion for choosing heteroatom precursors or investigate the precursor effect on ORR activity over heteroatom-doped nanocarbons.

Among nanocarbon materials, heteroatom-doped carbon nanotubes and graphene, one or two dimensional carbon networks with outstanding electric conductivity, have demonstrated excellent ORR performance, and have emerged as promising ORR catalyst candidates.[21-23] However, their relatively low electrochemical surface area (ECSA) and randomly formed oxygen-inaccessible microspores may lead to internal diffusion issues in practical single fuel cell cathode applications.[6, 24] In comparison, mesoporous carbon nanostructures are more advantageous to serve as the cathode catalyst in a real fuel cell setting, because they feature not only high conductivity, but also well-ordered porous structure and tunable uniform mesopores (e.g. 4-20 nm) with a high ECSA (>1000 m^2 g^{-1}).[25-27] Heteroatom (*e.g.* N) containing hydrocarbons are potentially attractive to serve as the carbon precursor; but some of them are very expensive with price even comparable to noble metals.[28-30] Thus, carbon precursor cost should also be taken into consideration for the catalyst preparation and utilization in fuel cells.

Heteroatom-doped carbons are rarely directly employed as cathode catalysts in H_2/O_2 fuel cell, which is probably due to the membrane-electrode-assembly (MEA) fabrication issues,[7, 31] underperforming the electricity generation of H_2/O_2 fuel cells. For low temperature fuel cells directly fed with biomass-derived alcohols, such as ethanol and polyols, they are also attractive because they do not need a fuel reforming system and rigorous MEA fabrication process.[32, 33] In addition, the direct biorenewable alcohol fuel cells can simultaneously convert chemical energy into electrical energy and co-produce desirable biobased chemicals with the advantages of high efficiency, quiet operation and

low CO_2 emission.[5, 8] Therefore, they are poised to take a significant role in our future energy landscape. US DOE has identified the top ten important chemicals, including ethanol, polyols (glycerol, sorbitol, etc.),[34] which can be economically derived from biomass, and can serve as building blocks for chemicals, fuels and energy production in the future.

Herein, we report a nitrogen and sulfur dual-doped, metal-free mesoporous carbon (N-S-CMK-3) with outstanding electrocatalytic activity for ORR and its utilization as a cathodic catalyst in a direct biorenewable alcohol fuel cell, which exhibits remarkable performance and operation stability as compared with a noble metal Pt/C cathode fuel cell. A ubiquitous environment-friendly renewable biomass compound, glucose, serves as the carbon sources. Highly active N and S are introduced from ammonia (NH_3) and thiophene precursors, which can efficiently prevent N-S-CMK-3 from having clogged inside pores and channels thereby obtaining a highly organized mesoporous structure with high surface area. Simultaneously generating macropores (pore diameter > 200 nm) together with mesopores improves the adsorption of O_2 and increases the electrocatalytic activity for ORR. After ruling out the transition metal (Fe) effect, high ORR activity and fuel cell performance can be largely ascribed to the synergistic effect of N and S atoms with specific structures (e.g. graphitic-N and C-S-C). The high ORR activity of N-S-CMK-3 with robust stability and excellent tolerance of alcohol crossover in the direct alcohol alkaline fuel cell is superior to that of noble metals and holds promise of serving as cathode catalyst for other energy conversion and storage devices, such as the H_2/O_2 fuel cells and metal-air batteries.

3.2 Experimental

3.2.1 Material Preparation

The synthesis of CMK-3 uses SBA-15 as the template. For the synthesis of SBA-15,[35] Pluoronic P123 (5.0 g) was dissolved in a hydrochloric solution (190 mL, 1.6 M) with 350 rpm stirring at 35 °C. After the dissolution of P123, tetraethyl orthosilicate (11.0 g) was added into the solution and stirred at 35 °C for another 24 h. The solution was then moved into a polytetrafluoroethylene bottle for an additional 24 h treatment at 100 °C. After that, the solid was filtered and washed with deionized water (18.2 MΩ) and dried in an oven overnight. A final calcination in air at 550 °C for 6 h was used to remove the surfactant. Then, SBA15 (2.8 g) was mixed with deionized water (15 g), glucose (3.5 g), and sulfuric acid (0.39 g). The mixture was treated at 100 °C for 6 hours, and then at 160°C for another 6 hours. Deionized water (15 g), glucose (2.24 g), and sulfuric acid (0.25 g) was again added, mixed, and treated under the same condition described above. The sample was then heated at 900 °C and kept for 10 h under flowing nitrogen. The sample was treated with 10% hydrofluoric acid in ethanol solution (50% by volume) to remove silica. After filtration and drying, the base CMK-3 was obtained.

The nitrogen and sulfur dual-doped N-S-CMK-3 catalysts were synthesized under high temperature annealing. 0.5 g thiophene and 0.5 g iron chloride ($FeCl_3$) were dissolved into 15 ml of ethanol with magnetic stirring, followed by directly adding 0.5 g CMK-3, and the mixture was left under magnetic stirring at ambient temperature for 12 h. The pre-treated CMK-3 was obtained by filtrating and washing with deionized water for 5 times to remove iron chloride residue followed by drying at 80 °C for 12 h. After completely removing the liquid solution, the pre-treated CMK-3 was annealed in ambient pressure NH_3 gas with a

60 ml min^{-1} flow rate. The temperature was kept at 700, 800 and 900 °C for 2 h, respectively, after a heating rate of 5 °C min^{-1}. After cooling down to room temperature, the sample was subjected to a 6.0 M hydrochloric acid treatment to further remove the Fe residue, and the final N-S-CMK-3 was obtained by washing with deionized water to a pH of 7 and drying at 60 °C for 12 h. Single-doped N-CMK-3 and S-CMK-3 were synthesized by using similar method discussed above without thiophene or NH$_3$ dopants, respectively.

3.2.2 Physical Characterization

Composition was measured using aninductively coupled plasma mass spectrometry (ICP-MS, PerkinElmer). The sample was prepared by dissolving 10 mg of catalyst in 4 mL of fresh aqua regia, followed by diluting to 250 mL with deionized water (18.2 MΩ). The XRD patterns were obtained from a Rigaku Ultima IV X-ray diffraction (XRD) systems with Cu Kα radiation (λ = 1.5406 Å), with a tube current of 44 mA and a tube voltage of 40 kV. JEOL 2100 200 kV scanning and transmission electron microscope (STEM) and corresponding element energy-dispersive X-ray spectrometer (EDS) were utilized to determine the catalyst structure and element concentration. JEOL 5800LV and FEI Quanta 250 field-emission scanning electron microscope (SEM) were used for macro morphology determination. X-ray photoelectron spectroscopy (XPS) with Mg K alpha X-ray (1253.6 eV) (Kratos Amicus/ESCA 3400) was also used to determine the heteroatom concentrations and its corresponding status through different binding energy peak. Surface area and porosity characterization were performed via nitrogen physisorption in a Micromeritics ASAP 2020 operated at -196 °C. The specific surface areas were calculated using the Brunauer-Emmett-Teller (BET) equation and the pore volume was determined at a relative pressure of 0.973. A DXR Raman microscope (Thermo Scientific, Waltham, MA,

USA) was used for spectra acquisition with 780 nm excitation at 14 mW laser power, 10×
objective, and 50 μm slit aperture (resolution is 4-8 cm^{-1}). The exposure time is 30 s.

3.2.3 Electrochemical Characterization

The electrochemical tests were carried out both in the half-cell and fuel cell reactors. The
half-cell test was conducted in a three-electrode setup consisting of a rotating disk electrode
(working electrode), a coiled platinum counter electrode, which was isolated by a fritted
glass tube from the main test electrolyte, and a Hg/HgO reference electrode with 0.1 M
KOH filling solution. Potential was applied by using a multi-channel potentiostat
(Biological).To fabricate the working electrode, a 2.0 mg ml^{-1} solution of catalyst ink was
prepared by dispersing N-S-CMK-3 in mixture of iso-propanol and 5 wt% Nafion solution
(one-propanol : Nafion solution = 9 : 1 v/v), followed by ultrasonication until no
aggregation was visible. Then, 30 μL of ink was dropped onto the surface of a glassy carbon
electrode with a catalyst loading of 0.306 mg cm^{-2}, and a uniform catalyst film was obtained
after 30 min ambient temperature drying in air. In order to compare the ORR performance
of N-S-CMK-3 to other control samples, the electrodes of Pt/C, CMK-3 and mono-element
doped CMK-3 were fabricated by using the same method discussed above. The ORR
performance of the catalyst was investigated by cyclic voltammetry (CV) test, which was
performed at 50mV s^{-1} scan rate after purging the electrolyte with N$_2$ and O$_2$ for 30 min
respectively, followed by the linear sweep voltammetry (LSV) toward ORR activity
evaluation in O$_2$-saturated electrolyte with 10mV s^{-1} scan rate at different rotating rate from
2000 rpm to 400 rpm.

Rotating ring-disk electrode (RRDE) was employed to measure the concentration of HO$_2^-$
intermediate and electron transfer number per oxygen (n) with scanning rate of 10 mV s^{-1}

at rotating rate of 1600 rpm. The HO_2^- intermediated, generated on the surface of disk electrode (0.19625 cm2 geometric surface area), can be immediately oxidized on Pt-ring electrode surface at 0.8 V vs. RHE applied potential. The electron transfer number n and HO_2^- intermediate production percentage (HO_{2-} %) were determined as follows:[28]

$$n = 4 \times \frac{I_d}{I_d + I_r / N}$$

$$HO_2^- \% = 200 \times \frac{I_r / N}{I_d + I_r / N}$$

where I_d is the disk current; I_r is the ring current, and N is the ring current collection efficiency which was determined to be 23%.[54]

All experimental results for the ORR activity in this paper were reported as current density versus applied potential (vs RHE), and the current densities were normalized using geometric surface area of a glassy carbon electrode with 5 mm diameter. The Hg/HgO reference electrode was calibrated with respect to the reversible hydrogen electrode (RHE) before use. The calibration was conducted in standard three-electrode system with Pt wire as the working and counter electrodes, and the Hg/HgO electrode as the reference electrode. The 0.1 M KOH electrolyte was purged and saturated with high purity H_2.for 30 min before calibration, and LSV test was then run at a scan rate of 0.5 mV s^{-1}, and the potential range of -0.93 V to -0.85 V vs Hg/HgO, where the current crossed zero is taken to be the thermodynamic potential for the hydrogen electrode reactions. The result is E(RHE) = E(Hg/HgO) + 0.888 V in 0.1 M KOH electrolyte.

The fuel cell tests were performed on a Scribner Fuel Cell System 850e (Scribner Associates, USA), and the fuel cell fixture with an active area of 5 cm^2 was purchased from

Fuel Cell Technology Inc. The cathode electrode composed of 70 wt% N-S-CMK-3 catalyst and 30 wt% AS-4 ionomer was mixed and directly sprayed onto an A-201 anion exchange membrane to obtain a catalyst loading of 2.0 mg cm^{-2}, while commercial Pt/C blended with 5wt% PTFE solution (Pt/C : PTFE = 9 : 1 w/w) was sprayed onto a PTFE-untreated carbon cloth liquid diffusion layer with a 1.0 mg$_{pt}$ cm^{-2} catalyst loading. The membrane electrode assembly (MEA) was constructed by pressing the anode carbon cloth with anion exchange membrane, which has been sprayed with cathode catalyst. 2.0 M KOH with 1.0 M fuel (glycerol, ethanol or sorbitol) was pumped into the anode compartment at 1.0 ml min^{-1}, while high purity O$_2$ (99.999%) regulated at 400 ml min^{-1} was fed to cathode side with 30 psi backpressure.[44] The cell temperature was kept at 50 °C, and the relative humidity for both anode and cathode is 100 %. The MEA was activated at 0.1 V cell voltage until the current density got stable. The I-V polarization curve was obtained by applying a constant voltage and collecting corresponding current density.

The overall electron transfer numbers per oxygen molecule involved in the typical ORR process were calculated from the slopes of the Koutecky-Levich plots using the following equations:[14,30]

$$\frac{1}{J} = \frac{1}{J_L} + \frac{1}{J_k} = \frac{1}{B\omega^{1/2}} + \frac{1}{J_k} \qquad (1)$$

$$B = 0.2nFC_o(D_o)^{2/3}\upsilon^{-1/6} \qquad (2)$$

$$J_k = nFkC_o \qquad (3)$$

where J is the measured current density, J_k and J_L are the kinetic and diffusion limiting current densities, ω is the electrode rotating speed in rpm, B is the reciprocal of the slope, n is the number of electrons transferred per oxygen molecule, F is the Faraday constant

(96485 C mol^{-1}), D_o is the diffusion coefficient of O$_2$ in 0.1 M KOH (1.9×10^{-5} cm s^{-1}), v is the kinetic viscosity (0.01 cm^2 s^{-1}), and C_o is the concentration of O$_2$ (1.2×10^{-3} mol L^{-1}). The constant 0.2 is adopted when the rotating speed is in rpm, and k is the electrontransfer rate constant.

3.3 Results and discussion

3.3.1 Material synthesis and characterization

The well-ordered mesoporous carbons, N-S-CMK-3, were synthesized via carbonization and subsequent N and S doping processes, as shown in **Figure 3.1**. Glucose served as the carbon source to mix with the mesoporous SBA-15 silica template,[35] prior to calcination. Hydrofluoric acid (HF) was used to etch away the SBA15 template to obtain pure CMK-3 mesoporous carbons. Then, a mixture of CMK-3 and thiophene as well as iron(III) chloride (FeCl$_3$) was annealed at 800 °C under anhydrous ammonia (NH$_3$) gas purging, to facilitate heteroatom N and S doping into the graphitic framework of CMK-3. The N-S-CMK-3 mesoporous carbons were finally exposed to hydrochloric acid (HCl) washing and overnight vacuum drying (For synthesis details, see Experimental section).

In this work, glucose was chosen as the carbon precursor for mesoporous carbon synthesis owning to its unbranched carbon structure that facilitates formation of a stable and well-ordered mesoporous structure with narrow pore size distribution through carbonization.[27] Glucose can be ubiquitously obtained in large quantities at low price, while some previously reported heteroatom-containing carbon precursors (e.g. Ferrocene, Vitamin B12, PDI) have 10 fold higher price.[28–30] Together with its additional advantages of non-toxicity and non-volatility, glucose is a promising green carbon precursor for mesoporous carbon synthesis. We chose ammonia and thiophene as the N and S dopant precursors based on

consideration of their small molecular weight, simple molecular structure and high N/C

and S/C ratios (1.0 and 0.5, respectively). These precursors can not only largely prevent

pore clogging by CN and CS species in the doping process, but also facilitate formation of

high N and S content mesoporous carbon with very large surface area ($>1000 \text{ m}^2 \text{ g}^{-1}$), since

ammonia etching can assist in the formation of extra macropores (pore diameter $>$ 200

nm).[36] Single and multi-doped CMK-3 carbons were prepared for comparison through the

same processes as described above, and a commercial Pt/C, the best-known ORR catalyst,

was also studied as the baseline performance in this work.
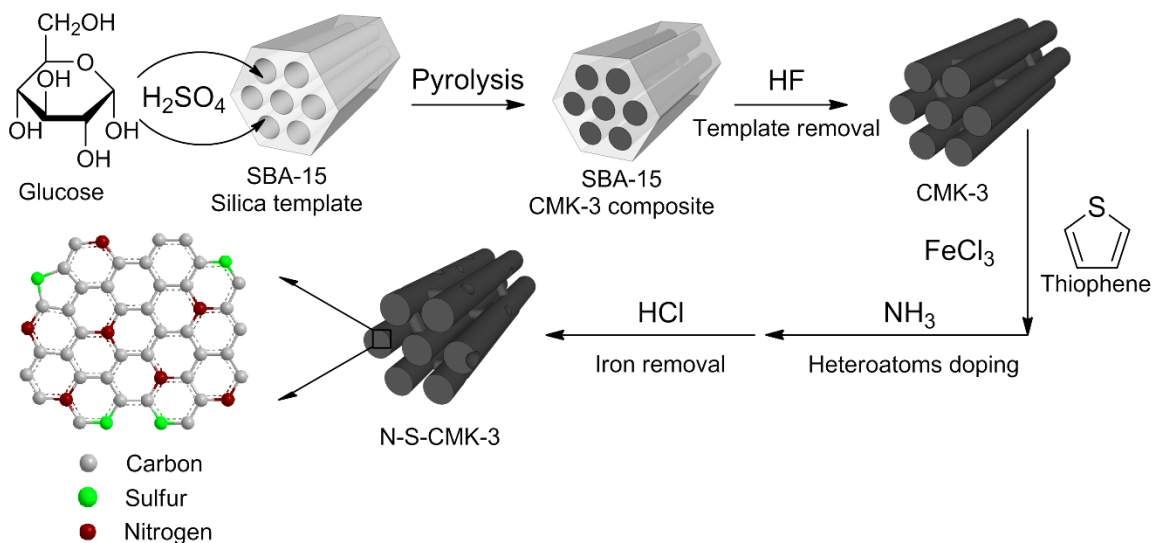
Figure 3.1 Schematic of the synthesis of metal-free mesoporous N-S-CMK-3 catalysts.
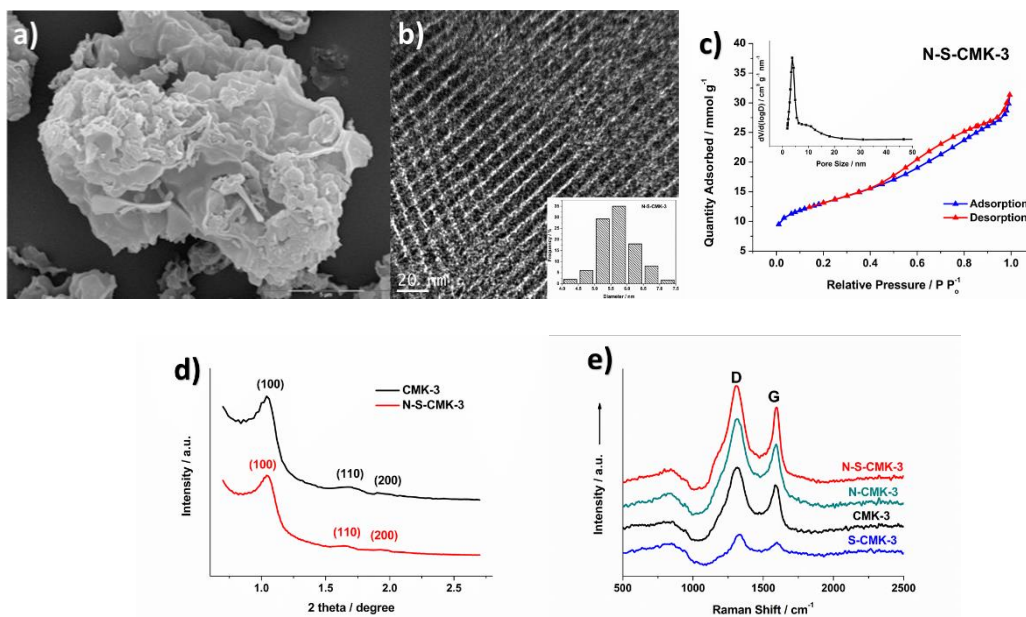
Figure 3.2 a) SEM image **b)** TEM image and **c)** Nitrogen adsorption-desorption isotherms and pore size distribution **(Inset)** of N-S-CMK-3 800 °C; **d)** Small-angle XRD patterns of N-S-CMK-3 800 °C and CMK-3; **e)** Raman spectra of N-S-CMK-3 800 °C, N-SCMK-3, S-CMK-3 and CMK-3.

The as-synthesized mesoporous N-S-CMK-3 catalysts were first characterized using scanning electron microscopy (SEM), as shown in **Figure 3.2a**. The morphology of the N-S-CMK-3 was irregular with visible macropores on the surface, which had no distinguishable morphology change compared with that of CMK-3 (**Figure S1**). The underlying highly organized hierarchical porous structures were observed by transmission electron microscopy (TEM) characterization (**Figure 3.2b**). The TEM images revealed an average carbon rod diameter of 6 nm, which is consistent with the pore size of the SBA-15 template (**inset in Figure S3a**), indicating successful carbonization of glucose within the silica template. However, it is interesting to note that the carbon structure varied when the heteroatom doping temperature increased from 700 °C to 900 °C (**Figure S2**). At a doping temperature of 700 °C, apparent clogging from the thiophene derived CS species during the doping process became more serious and the carbon sheets were randomly formed,

which could undesirably decrease the surface area and pore volume of carbon catalysts, leading to a ORR performance drop.[37] The doping temperature of 900 °C appeared to facilitate the decomposition of the mesoporous carbon and a resulting porous structure was dominantly observed instead of the organized hierarchical porous structures (**Figure S2**), because of the overreaction of ammonia with carbon during the heteroatom doping process. Ammonia etching of the carbon may follow the reactions shown below:[36]

$$2NH_3 \rightarrow N_2 + 3H_2 \qquad\qquad\qquad \textbf{(4)}$$

$$C + 2H_2 \rightarrow CH_4 \qquad\qquad\qquad\qquad \textbf{(5)}$$

The ammonia etching can be regulated by tuning the doping temperature. A moderate etching rate at around 800 °C (doping temperature) favors the formation of macropores and not only diminishes the CS species clogging effect, but also significantly increases the surface area of the resulting N-S-CMK-3 mesoporous carbon. To better investigate the temperature effect on catalysts structure, the BET surface areas of the N-S-CMK-3 catalysts were measured to be 784 m^2 g^{-1} with (N-S-CMK-3 700 °C), 1023 m^2 g^{-1} (N-S-CMK-3 800 °C) and 921 m^2 g^{-1} (N-S-CMK-3 900 °C), all of which were lower than the 1126 m^2 g^{-1} of CMK-3, but much higher than previously reported carbon nanotube and graphene ORR catalysts, such as mesoporous graphene and carbon hybrids[11,17] (the BET surface area and total pore volume of all the as-synthesized CMK-3 based catalysts are shown in **Table S1**). Therefore, 800 °C was determined to be the optimal doping temperature to prepare well-ordered mesoporous N-S-CMK-3. The surface texture of the N-S-CMK-3 catalysts was investigated by N_2 adsorption-desorption isotherms (type IV), and the typical hysteresis loops was observed to reveal the mesoporous nature of the well-

ordered N-S-CMK-3 catalysts. The pore diameter of N-S-CMK-3 was centered at 3.7 nm according to the Barrett-Joyer-Halenda (BJH) model (**inset in Figure 3.2c**),[38] which is close to the dominant pore diameter of 3.8 nm for pure CMK-3 (inset in Figure S3b); whereas larger mesopores with pore size ranging from 4.8 nm to 15.0 nm and macropores (>200 nm) were only obtained in N-S-CMK-3 after heteroatom doping. This wide pore size distribution further confirms the ammonia etching reaction with the N-S-CMK-3 mesoporous carbon. Zhang et al. reported that the combination of macropores and large mesopores could enhance the rate of desolation and adsorption of O_2 and increase the electrocatalytic activity for ORR.[39] Consistent with that report, the N-S-CMK-3 (800 °C) with the unique mesoporous and extra macroporous structures exhibits the highest ORR performance among all investigated CMK-3 based catalysts as shown follows.

The well-ordered mesoporous carbon structure was also verified by wide-angle XRD measurement, as shown in **Figure 3.2d**. Three well-resolved diffraction peaks were observed in the small-angle XRD pattern of N-S-CMK-3, which can be assigned to (100), (110), and (200) reflections of 2D-hexagonal arrangements, and was very similar to that of the pristine CMK-3. Furthermore, two broad diffraction peaks centered at 25° and 44°, corresponding to the graphite (002) and (101) facets,[30] were observed in both the N-S-CMK-3 and CMK-3 wide-angle XRD patterns (**Figure. S4**), indicating no significant structure change during the N-, S-doping process, and these are in good agreement with the results observed from TEM images.

More structural information for N-S-CMK-3 was obtained from Raman spectroscopy (**Figure 3.2e**). Two typical bands observed at 1340 cm^{-1} and 1580 cm^{-1} can be assigned to the D- and G- bands, corresponding to the disordered carbon structure and interplane sp^2-

hybridized graphitic carbon sheet, respectively.[30,40] The I_D/I_G ratio of N-S-CMK-3 is similar to that of CMK-3 and lower than that of N-CMK-3 and S-CMK-3, suggesting a more graphitic structure with relatively low defect sites for the N-S-CMK-3 sample.

To determine heteroatoms content in as-synthesized N-S-CMK-3, catalysts were characterized by energy-dispersive X-ray spectroscopy (EDS). The EDS spectra reveal the presence of N, S and O atoms in the graphitic framework, while no Fe signal was observed (**Figure S5a**), indicating the Fe was removed by hydrochloric acid (HCl) washing and the high ORR activity could be only ascribed to the N-S-CMK-3 catalyst. Moreover, the EDS elemental mapping in conjunction with the TEM images illustrates a homogeneous distribution of N and S in the N-S-CMK-3 catalyst (**Figure S5b-d**). X-ray photoelectron spectroscopy (XPS) was further used to characterize N, S and O valence states. From **Figure 3.3a**, the content of the elements were determined by XPS to be 3.84 atom% of N, 0.83 atom% of S and 1.14 atom% of O, and negligible 0.12 atom% of Fe in N-S-CMK-3 for the 800 °C heteroatom doping temperature. Although the small amounts of Fe were quantified, no Fe signal was observed using the higher solution spectrum of XPS (**Figure S6a**), suggesting the removal of Fe through HCl washing. The Fe result from XPS could be due to the signal to noise resolution limitation of XPS. The high-resolution S_{2p} spectrum was found to be fitted into two peaks centered at 163.5 eV and 165.0 eV, representing to $S_{2p\ 3/2}$ and $S_{2p\ 1/2}$; whereas SO_x groups, which have been reported inactive for ORR, was not found (**Figure 3.3b**).[41, 42] Similarly, the high-resolution N_{1s} spectra showed three nitrogen forms existed, which can be typically illustrated as pyridinic-N (398.3 eV), pyrrolic-N (399.9 eV), graphitic-N (401.2 eV) and N^+-O^- (403.6 eV) structures, as shown in **Figure 3.3c**.[19, 28, 43] The C_{1s} high-resolution spectrum was deconvoluted into single peaks

corresponding to 284.5 eV (C1) for sp^2-hybridised carbon atoms bonded to neighboring

carbon and hydrogen atoms, 285.5 eV (C2) for C-N-C and C-S-C, and 288.0 eV (C3) for

different oxygen-containing groups (e.g. COOH, C=O, and C-OH),[28] further confirming

that N and S were successfully doped into the CMK-3 carbon framework (**Figure S6b**).

Inductively coupled plasma-mass spectrometry (ICP-MS) was also used to further test the

content of Fe residue in N-S-CMK-3 catalysts. The Fe concentration was detected as only

0.09 wt%, which is close to the ICP-MS detection limit, further indicating successful Fe

elimination for the N-S-CMK-3 mesoporous carbon.
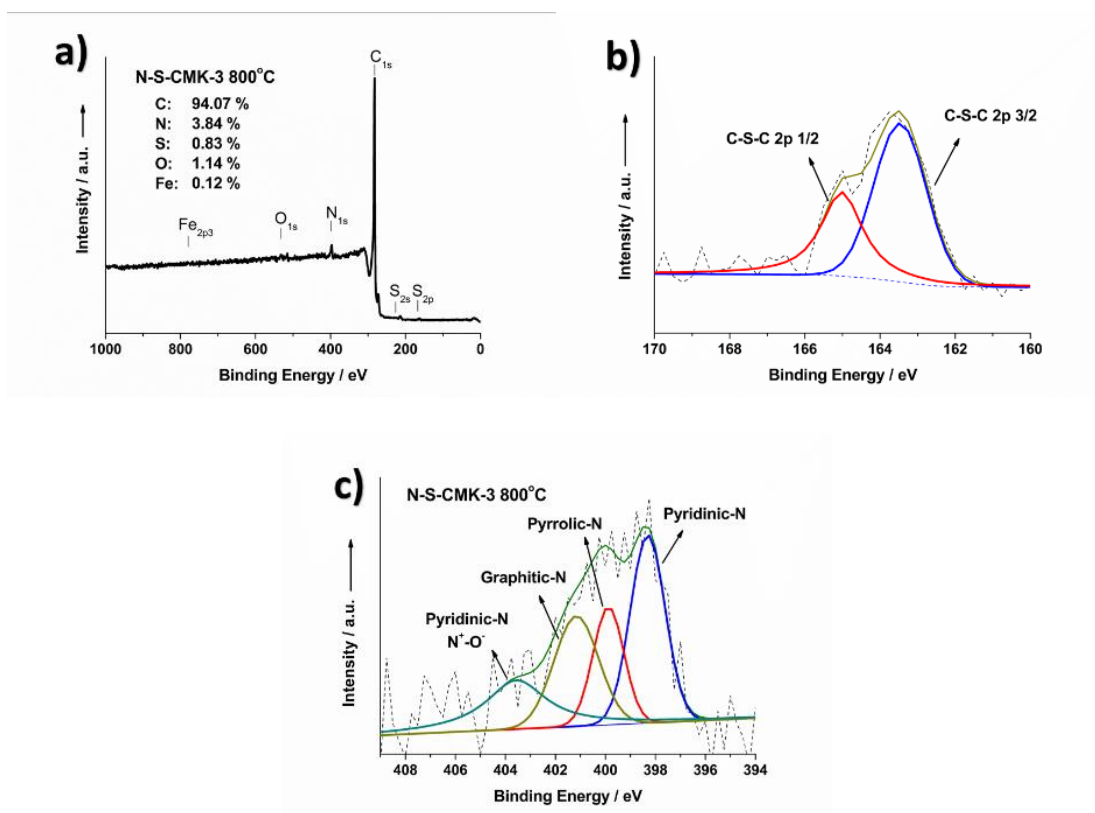
Figure 3.3 a) XPS survey spectrum; high-resolution spectra of **b)** S$_{2p}$ and **c)** N$_{1s}$ of N-S-CMK-3 800 °C.

3.3.2 Electrocatalytic analysis in half cell

Before electrocatalytic ORR activity investigation, the Hg/HgO reference electrode was calibrated with respect to the reversible hydrogen electrode (RHE), and the result is $E_{(RHE)}$ = $E_{(Hg/HgO)}$ + 0.888 V in 0.1 M KOH electrolyte, as shown in **Figure S7**.

All applied potential reported in this paper was versus the reversible hydrogen electrode (RHE).

The ORR electrocatalytic activity of N-S-CMK-3 was first investigated by cyclic voltammetry (CV) tests, as shown in **Figure S8**. Featureless voltammetric currents without an obvious redox peak were obtained when the 0.1 M KOH electrolyte was saturated with N_2 (short dash curve), as a result of the well-known typical capacitance effect on porous carbon materials. In contrast, when an O_2-saturated electrolyte was used, a well-defined cathodic ORR peak, centered at 0.66 V with 5.45 mA cm^{-2} current density, was observed over as-synthesized N-S-CMK-3, demonstrating obvious ORR electrocatalytic activity. To obtain deeper insight of ORR steps on the N-S-CMK-3 catalysts, linear sweep voltammetry (LSV) tests were carried out at different rotating rate ranging from 2000 rpm to 400 rpm in 0.1 M KOH electrolyte saturated with O_2 (**Figure 3.4a**). The voltammetric profiles demonstrate the current density increased as the applied potential became more negative, and the CMK-3 based catalysts were first investigated with different annealing temperature.

As shown in **Figure 3.4b**, N-S-CMK-3 800 ℃ exhibited the best ORR performance with the highest limiting current density of 5.50 mA cm^{-2} at 0.5 V and the most positive onset potential of 0.92 V among three N-S-CMK-3 catalysts annealed by different temperature. The possible reason is that the N-S-CMK-3 800 ℃ maintained the largest surface area

(1023 m2 g^{-1}) after heteroatom doping, while 700 °C and 900 °C led to surface area reduction to 784 m^2 g^{-1} and 921 m^2 g^{-1}, respectively (**Table S1**). In addition, an apparent clogging with the thiophene derived CS species occurred at 700 °C doping process, which could undesirably decrease the surface area and pore volume of carbon catalysts, and lead a O$_2$ diffusion issue for ORR; while 900 °C doping temperature can cause overreaction of ammonia with mesoporous carbon and result in decomposition of porous structure, which was predominantly observed instead of the organized hierarchical porous structures in SEM images (**Figure. S2**). Thus, the highly ordered mesoporous structure with extra macropores was formed by moderate etching reaction of NH$_3$ at 800 °C doping temperature, which provided the largest surface area and benefited the best ORR performance among these three N-S-CMK-3 catalysts.

Comparative studies of solely doped N-CMK-3, S-CMK-3, and pristine CMK-3 as well as with Pt/C were also conducted using the same LSV method. As shown in **Figure 3.4c**, with N or S solely doped into CMK-3 carbon frameworks, the onset potential (potential at which J = 0.1 mA cm^{-2}) increased from 0.79 V (CMK-3) to 0.83 V (S-CMK-3) and 0.87 V (N-CMK-3), respectively, and their corresponding ORR current density at 0.5 V raised from 1.98 (CMK-3) to 2.88 (S-CMK-3) and 3.30 (N-CMK-3) mA cm^{-2}, respectively. Evidently, the ORR activity of CMK-3 was improved with involvement of heteroatoms, which could be attributed to the positive change in the charge density or/and spin density of neighbor carbon atoms (serving as ORR active sites), facilitating 4e$^-$ transfer ORR. Furthermore, by simultaneously incorporating N and S, the ORR activity of N-S-CMK-3 was further enhanced, and exhibited an ORR current density of 5.50 mA cm^{-2} at 0.5 V and an onset potential of 0.92 V with Tafel slope of 68 mV dec^{-1}, which were comparable to the best-

known ORR catalyst, Pt/C (**Figure. S9**). In addition, only a 33 mV half-wave potential difference ($E_{1/2}$) was observed between the N-S-CMK-3 and Pt/C, indicating promising potential of N-S-CMK-3 to be an alternative to Pt/C as ORR catalysts.

The ORR catalytic activity of various catalysts was further compared in **Table S2**, including transition-metal based carbon materials (e.g. Fe-N/C, Mn_3O_4/porous glassy carbon) and metal free carbon materials (e.g. N–S mesoporous graphene, N–S doped graphene/CNT).[14,21,43-46] Chen et al. reported the N and S doped graphene-CNT with an onset potential of 0.85 V and electron transfer number of 3.8,[21] which are lower than that of N-S-CMK-3 reported in this work, probably due to the uniform mesoporous structure with high surface area (1023 m^2 g^{-1}). Liu et al. synthesized the heteroatom doped carbon materials ($FeSO_4$-PEI) exhibited a decent Tafel slope,[45] but its onset potential, 0.79 V, with electron transfer number of 3.8 affects its feasibility as a highly active ORR catalyst. Obviously, among the catalysts summarized in **Table S2**, N-S-CMK-3 provided more positive onset potential, higher ORR limiting current density, and sharper Tafel plot, all of which further confirmed its intrinsic high catalytic activity towards ORR. It should be noted that the onset potential and Tafel slope exhibited by ORR catalysts are very sensitive to its loading, and the reported catalyst loading is significantly varied from 0.0001 to 0.4 mg cm^{-2}, as summarized in **Table S2** (or to even higher value). Thus, the electron transfer number (n), obtained from RDE and RRDE, and mass-transport limiting current were investigated to further evaluate the intrinsic ORR kinetics of different ORR catalysts.

The electron transfer number (n) at a given applied potential was calculated by Koutecky-Levich (K-L) equation (for K-L equation details see Experimental section). The K-L plots (J^{-1} vs. $\omega^{-1/2}$) of the N-S-CMK-3 800 ^{o}C catalyst exhibited a high linearity, and the slopes

within investigated applied potentials (0.2 to 0.5 V) were approximately constant (inset in

Figure. 3.4a), implying a close n value for ORR at such potential range. Consequently, the

n value of N-S-CMK-3 800 ºC was determined to be 4.0 at such applied potential range,

which is same as the n value of Pt/C (**Figure S10**), suggesting a complete ORR process

with 4e⁻ transfer reduction to H_2O. In addition, the n value of solely doped N-CMK-3, S-

CMK-3 and blank CMK-3 were also calculated by using K-L equation. As shown in **Figure**

S10, the n value of CMK-3, S-CMK-3 and N-CMK-3 were calculated to be 2.2, 2.8 and

3.4 at 0.5 V vs. RHE, respectively, which are in good accordance to the trend of their

corresponding limiting current density as discussed above. The kinetic limiting current

density (J_k) at 0.5 V was also determined by K-L equation and was displayed in **Figure**

S10. Although both N-CMK-3 and S-CMK-3 showed moderate performance for ORR,

only N-S-CMK-3 exhibited an elegant ORR activity with complete 4e⁻ pathway (n=4) as

comparable to Pt/C. Remarkably, the J_k of N-S-CMK-3 (32.6 mA cm⁻²) slightly surpassed

that of Pt/C (25.6 mA cm⁻²) at 0.5 V and was much higher than that of N-CMK-3, S-CMK-

3 and CMK-3 samples.

To further investigate the ORR activity of N-S-CMK-3 and its corresponding reaction

mechanism, RRDE tests were conducted to directly measure the concentration of HO_2^-

intermediate and determine the electron transfer number (n) of catalysts. The generated

HO_2^- intermediate on the surface of disk electrode can be immediately oxidized on the

surface of Pt ring electrode at 0.8 V vs. RHE applied potential, thus RRDE is reliable to in

situ determine n toward the N-S-CMK-3 catalysts. As shown in **Figure 3.4d**, N-S-CMK-3

showed the lowest ring current density ascribing to the HO_2^- oxidation, and the HO_2^- yield

on disk electrode was below 1.5% in the potential range from 0.25 V to 0.6 V, while the

average HO_2^- yield of other CMK-3 based catalysts were 92% (CMK-3), 62% (S-CMK-3), 27% (N-CMK3), respectively (**Figure 3.4e**). The large amount of HO_2^- intermediate production could decrease the *n* and drastically reduce the ORR performance toward catalysts. Consequently, the average *n* value of N-S-CMK-3 at investigated potential was determined to be 3.96 without apparent change in such potential range (**Figure 3.4e**). This is much higher than those over other investigated catalysts (e.g. *n* = 3.45 for N-CMK-3, *n* = 2.76 for S-CMK-3, and *n* = 2.15 for CMK-3), which is in good accordance with the results obtained from the K-L equation calculation in RDE tests. The performance of non-doped and mono-doped CMK-3 were far from satisfactory. However, with both N and S heteroatoms doping into carbon structure of mesoporous CMK-3, the catalyst ORR activity was significantly improved. This could be ascribed to the additional S atoms doping into N-CMK-3, further leading the positive charge and asymmetric spin density of neighboring carbon atoms, which are serving as the ORR active sites (the details were discussed in Section 3.4 "Insights into the synergistic effect of N and S on ORR").[14, 47] The synergistic effect between N and S heteroatoms on neighbor carbons could facilitate the complete oxygen reduction reaction with $4e^-$ transfer, and decrease the HO_2^- intermediate yield. On the other hand, the high surface area (1023 $m^2\ g^{-1}$) of N-S-CMK-3 with a uniform structure combining mesopores and macropores could provide more active sites, which is beneficial to the utilization of O_2 fuel, leading to a higher ORR activity. However, when only S was doped, the clogging issue could severely decrease the surface area of S-CMK-3. Together with these possible reasons, the N-S-CMK-3 exhibited a higher ORR limiting current density, and showed the best ORR activity among all investigated CMK-3 catalysts in this work, which is competitive to the that for Pt/C, suggesting its great potential to serve as a

Pt/C alternative for ORR at the cathode side of fuel cells, Li-ion battery, and other energy storage and conversion devices.
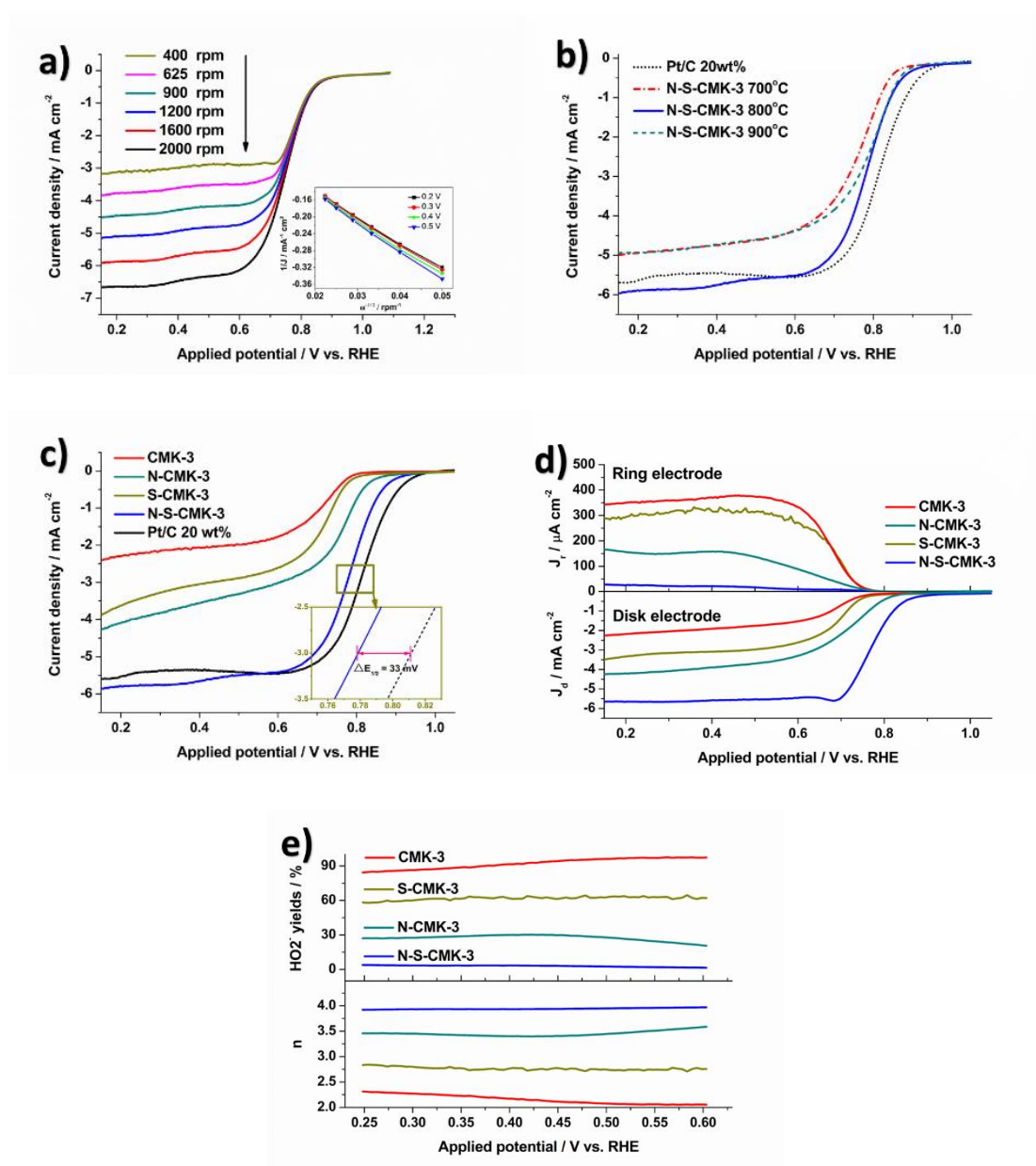
Figure 3.4 a) Polarization curves of LSV tests at different rotating speeds for N-S-CMK-3 800 °C conducted in in O_2-saturated 0.1M KOH solution at a scan rate of 10 mV s^{-1} (inset shows the corresponding K-L plots); **b)** Comparative polarization (RDE) curves for N-S-CMK-3 catalysts with different doping temperatures, and **c)** Comparative polarization curves for different catalysts with the same loading measured at 1600 rpm in O_2-saturated 0.1M KOH solution; **d)** Comparative polarization curves (RRDE) for different catalysts with the same loading measured at 1600 rpm in O_2-saturated 0.1M KOH solution; **e)** HO_2^- yields (top) during the ORR and the corresponding electron transfer nmber (n, bottom) of the prepared catalysts measured by RRDE.

Since the N-S-CMK-3 will be used as the cathode catalyst in direct alcohol fuel cell, the catalyst durability and alcohol fuel-crossover influence on ORR should be considered. The durability of the catalysts was first tested by cycling the catalyst between 0.1 V and 1.2 V at 10 mV s^{-1} scan rate under oxygen purging. After 3000 potential cycles, the N-S-CMK-3 exhibits a robust stability with only 46 mV of half-wave potential shift (**Figure 3.5a**), which is superior to 52 mV for the commercial Pt/C catalyst (**Figure S11**).

The stability of N-S-CMK-3 was further measured at a constant voltage of 0.5 V for 45000 s (12.5 hours). The results indicate slowly decreasing ORR performance with N-S-CMK-3 as 85.9% of the current was maintained after 45000 s. Conversely, Pt/C exhibits more serious performance degradation as only 76.1% of the current remained after an identical stability test (**Figure S12**). For fuel-crossover tolerance, glycerol, the coproduct (about 10 wt%) from biodiesel manufacturing, was added into the half cell reactor with the N-S-CMK-3 catalysts after 1800 s (chronoamperometry test at 0.6 V); comparative study of Pt/C catalysts was also carried out using the same method. Interestingly, when glycerol was added into electrolyte, the current density of N-S-CMK-3 had nearly no change, strongly indicating its high catalytic activity for ORR while being nearly inert towards glycerol oxidation (**Figure 3.5b**). Conversely, Pt/C exhibits an instantaneous current density spike due to its high activity toward glycerol oxidation, and thus its vulnerability to glycerol crossover.
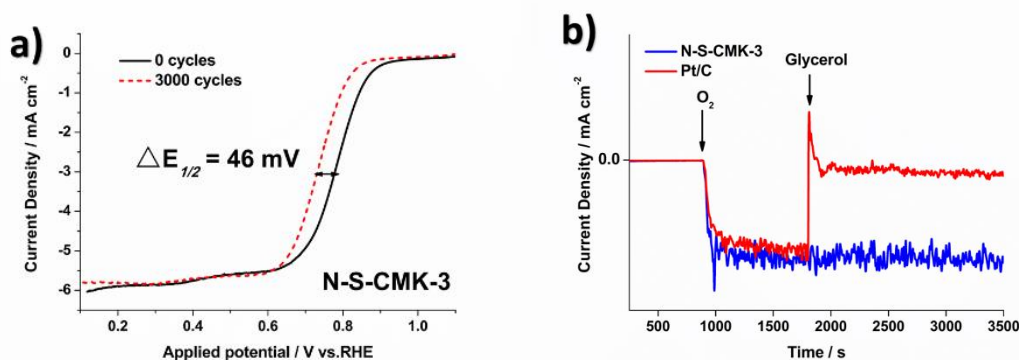
Figure 3.5 a) Polarization curves of N-S-CMK-3 800 °C before and after 3000 potential cycles in O_2-saturated 0.1M KOH solution; **b)** Glycerol crossover tolerance test of N-S-CMK-3 800 °C and commercial Pt/C conducted by chronoamperometic response at 0.6 V vs RHE.

3.3.3 Electrocatalytic analysis in single fuel cell

Single fuel cell performance is considered the ultimate catalyst evaluation method from both engineering and application points of view. The N-S-CMK-3 was fabricated into an alkaline membrane fuel cell, and its electrocatalytic activity toward ORR and single glycerol fuel cell performance tested. The steady-state polarization curves with different cathodic catalysts in the glycerol alkaline fuel cell are shown in **Figure 3.6a**. It is observed that the open circuit potential of the fuel cell with N-S-CMK-3, CMK-3 and Pt/C were 0.86 V, 0.70 V and 0.85 V, respectively. Due to the outstanding ORR electrocatalytic activity and apparent O_2 diffusion advantage, the glycerol alkaline membrane fuel cell with N-S-CMK-3 cathode yields a high peak power density of 88.2 mW cm^{-2}, which is much higher than that with the CMK-3 cathode, 42.4 mV cm^{-2}, and 84% of the fuel cell performance when compared with the best-known ORR catalyst, Pt/C, at cathode (105 mW cm^{-2} peak power density). It is worth to mention that the Fe loading would be extremely low (2.4 μg cm^{-2} cathode) as converted from 0.12 wt% of Fe determined by XPS. Based on the I-V curve analysis, the fuel cell with N-S-CMK-3 cathode displays Pt-like behavior both in kinetic dominated regime (current density < 50 mA cm^{-2}) and ohmic resistance controlled

regime (current density > 50 mA cm^{-2}),[44,45] implying a considerably high ORR activity and

less performance loss owing to the resistance to ionic current.
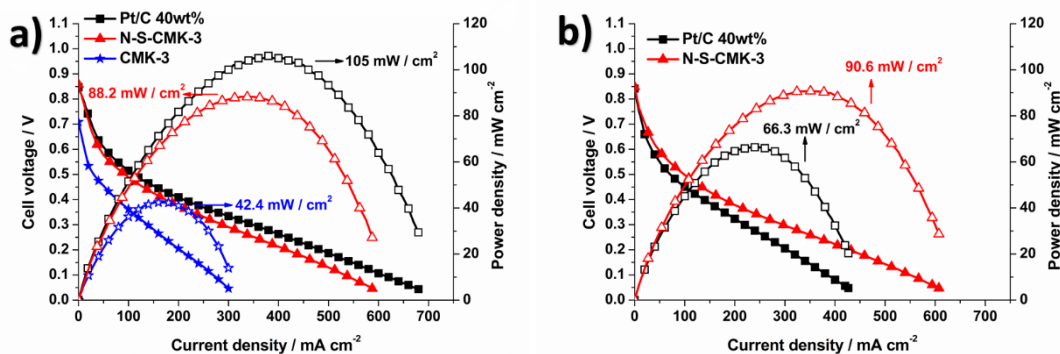
Figure 3.6 Polarization and power density curves before **a)** and after **b)** 2 h continuous current scanning of direct glycerol fuel cell with the N-S-CMK-3 cathode catalysts (loading 2.0 mg cm^{-2}) and Pt/C 40 wt% anode catalysts (loading 1.0 mgpt cm^{-2}) at 50 °C.

We also tested the fuel cell performance using other bioalcohol fuels, ethanol and sorbitol.

Ethanol is the first generation of biofuel and have been widely used as gasoline additive,[34]

while sorbitol is an important sugar alcohol that can be produced from cellulose hydrolysis

and potentially used as precursors to generate the biorenewable chemicals.[34,46,47] The N-S-

CMK-3 cathode alkaline fuel cell reached 80% of that with the Pt/C cathode alkaline fuel

cell using sorbitol, and even higher than that of Pt/C when ethanol is used as the fuel

(**Figure S13**). It should be noted that the catalyst layer for N-S-CMK-3 cathode is thicker

than that for Pt/C catalyst, which could affect the O_2 diffusion toward ORR on fuel cell

cathode side, leading to a slightly lower peak power density for N-S-CMK-3 cathode fuel

cell relative to the Pt/C cathode one. To further study the O_2 diffusion effect, different

backpressures (30 psi and ambient pressure) were used. From **Figure S14**, the peak power

density of N-S-CMK-3 cathode glycerol fuel cell was obtained as 82.7 mW cm^{-2}, which

has only 6.2% performance dropping in contrast to the 88.2 mW cm^{-2} achieved by using

30 psi backpressure. Thus, the O_2 diffusion issue is negligible when the backpressure

changes from 30 psi to ambient pressure. This good O_2 diffusion property can likely be attributed to its uniform mesoporous structure with a wide range of mesopores and macropores as well as the high surface area.

The durability of catalyst also serves as an important criterion to determine the suitability of N-S-CMK-3 in the cathodic side for ORR. As shown in **Figure 3.6b**, the glycerol fuel cell shows 90.6 mW cm^{-2} of peak power density after the 2 h scan current test, which is even slightly higher than the 88.2 mW cm^{-2} during initial performance and indicates robust stability and high selectivity to ORR in cathode of glycerol fuel cell. In contrast, the performance of the Pt/C cathode glycerol fuel cell was decreased dramatically from 105 mW cm^{-2} to 66.3 mW cm^{-2} (36.9% performance dropping) after 2 h, consistent with the ORR performance drop in the half cell fuel-crossover test, because glycerol could be readily oxidized on the Pt/C catalysts surface thereby decreasing the fuel cell performance after the fuel-crossover. Together with the excellent ORR performance in the glycerol alkaline fuel cell, good O_2 diffusion and expected durability, the as-synthesized N-S-CMK-3 could effectively serve as the cathodic catalyst in alkaline fuel cell.

3.3.4 Insights into the synergistic effect of N and S on ORR

To acquire the insight into synergistic effect of N and S heteroatoms on ORR activity, all of the CMK-3-based catalysts were characterized by XPS. The N/C and S/C atomic ratios were both significantly decreased from 6.40 atom% to 1.27 atom% and 1.11 atom% to 0.20 atom%, respectively, when the doping temperature was increased from 700 °C to 900 °C (**Figure 3.7a** and **Table S1**), which is similar to previous reports. The broad N1s peak was then deconvoluted into four peaks, assigned to pyridinic-N, pyrrolic-N, graphitic-N and N$^+$-O$^-$ (inactive to ORR) structures, respectively (**Figure S15** and **Figure 3.3c**).[19,43]

Interestingly, when combined with the ORR performance and electron transfer number, n, for the N-S-CMK-3 catalysts (**Figure 3.4b**), **Figure 3.7** reveals a correlation between the graphitic-N species and the ORR activity. For example, the N-S-CMK-3 (800 °C) with a higher proportion of graphitic-N centers favors higher ORR activity with complete 4e$^-$ transferred reaction, whereas those containing a lower portion of graphitic-N sites exhibit lower ORR activity for both the 4e$^-$ and 2e$^-$ reactions. In addition, although the graphitic-N content has been found to be close for N-CMK-3 and N-S-CMK-3 (**Figure 3.7b**), the N-CMK-3 without S doping exhibits moderate ORR activity with n of 3.0 at 0.5 V, which is much lower than that of N and S dual-doped N-S-CMK-3. Thus, it could be hypothesized that the doped graphitic-N and S atoms can increase both the catalyst activity toward ORR and the synergistic effect between N and S, thus greatly enhancing the ORR activity when combined in the N-S-CMK-3 catalysts. Qiao et al. carried out density functional theory (DFT) calculation to study synergistic effect of N and S on ORR performance.[14] The dual-doping graphitic-N and S into the carbon framework provides asymmetric spin and alters the charge density and spin density of neighbor carbon atom owning to the high electronegativity of N, 3.04 and a mismatch of the outermost orbitals of S; thus, it significantly uplifts the ORR activity.[41, 48-50] Based on the DFT calculation resulted discussed above, the graphitic-N and S cooperated in our N-S-CMK-3 could bring more ORR active sites and promote the catalyst's ORR activity to achieve comparable performance to the Pt/C catalyst.
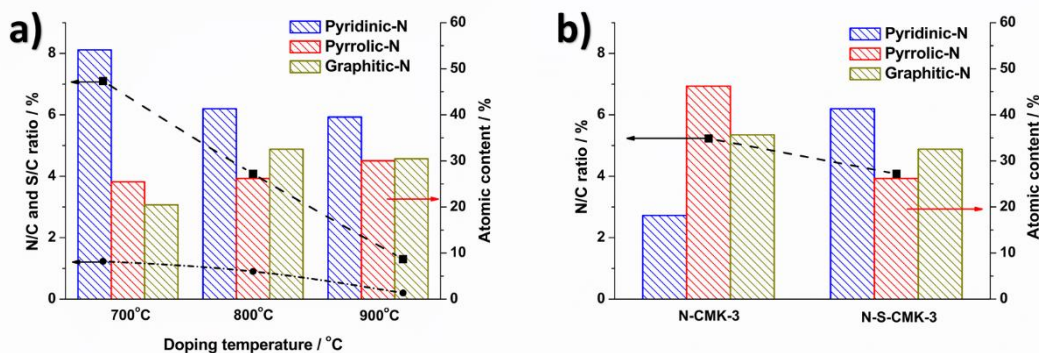
Figure 3.7 a) Histograms of different nitrogen-based functional groups content (right y axis) and N/C, S/C atomic ratios (left y axis) characterized on on the N-S-CMK-3, versus doping temperature; **b)** Histograms of different nitrogen-based functional groups content (right y axis) and N/C atomic ratios (left y axis) characterized on the N-CMK-3 and N-S-CMK-3, respectively.

3.4 Conclusions

In summary, we have demonstrated the successful synthesis of novel N- and S- dual-doped N-S-CMK-3 mesoporous carbons using biorenewable glucose as the carbon source and ammonia and thiophene as highly efficient N and S dopants. The high surface area (1023 $m^2 g^{-1}$), derived from a moderate NH_3 etching effect, and the synergistic effect of graphitic-N and S atoms resulted in remarkable electrocatalytic ORR activity. N-S-CMK-3 annealed at 800 °C exhibits the highest ORR activity (close to that of Pt/C) with 4.0 electron transfer number per oxygen and kinetic-limiting current density of 32.6 mA cm^{-2} at 0.5 V (vs RHE). By directly using N-S-CMK-3 as the cathode catalyst in single direct glycerol fuel cell, it exhibited 88.2 mW cm^{-2} peak power density without obvious O_2 diffusion limitation, which represents 84% of the initial performance of the one with a Pt/C cathode. More interestingly, the peak power density of the fuel cell with N-S-CMK-3 can maintain a peak power density at 90.6 mW cm^{-2} after two hours operation, while the one with Pt/C cathode lost its peak power density to 66.3 mW cm^{-2}. The robust stability and alleviation of fuel-crossover issue (resistance to alcohol oxidation) demonstrated in both half cell and single fuel cell tests strongly suggest the N-S-CMK-3 could be a promising substitute to replace noble metal

and serve as cathodic catalyst for alcohol alkaline fuel cells, H_2/O_2 fuel cells and likely other energy conversion and storage devices.

3.5 References

1.   A. J. Ragauskas, C. K. Williams, B. H. Davison, G. Britovsek, J. Cairney, C. A. Eckert, W. J. Frederick, J. P. Hallett, D. J. Leak, C. L. Liotta, J. R. Mielenz, R. Murphy, R. Templer, T. Tschaplinski, *Science* 2006, **311**, 484.

2.   M. I. Hoffert, K. Caldeira, G. Benford, D. R. Criswell, C. Green, H. Herzog, A. K. Jain, H. S. Kheshgi, K. S. Lackner, J. S. Lewis, H. D. Lightfoot, W. Manheimer, J. C. Mankins, M. E. Mauel, L. J. Perkins, M. E. Schlesinger, T. Volk, T. M. L. Wigley, *Science* 2002, **298**, 981.

3.   B. C. H. Steele, A. Heinzel, *Nature* 2001, **414**, 345.

4.   F. Y. Cheng, *J. Chen, Chem Soc Rev* 2012, **41**, 2172.

5.   E. H. Yu, X. Wang, U. Krewer, L. Li, K. Scott, *Energ Environ Sci* 2012, **5**, 5668.

6.   J. R. Varcoe, P. Atanassov, D. R. Dekel, A. M. Herring, M. A. Hickner, P. A. Kohl, A. R. Kucernak, W. E. Mustain, K. Nijmeijer, K. Scott, T. W. Xu, L. Zhuang, *Energ Environ Sci* 2014, **7**, 3135.

7.   J. R. Varcoe, R. C. T. Slade, *Fuel Cells* 2005, **5**, 187.

8.   W. Z. Li, W. J. Zhou, H. Q. Li, Z. H. Zhou, B. Zhou, G. Q. Sun, Q. Xin, *Electrochim. Acta* 2004, **49**, 1045.

9.   S. R. Brankovic, J. X. Wang, R. R. Adzic, Surf Sci 2001, **474**, L173.

10.   R. R. Adzic, J. Zhang, K. Sasaki, M. B. Vukmirovic, M. Shao, J. X. Wang, A. U. Nilekar, M. Mavrikakis, J. A. Valerio, F. Uribe, Top Catal 2007, **46**, 249.

11.   S. J. Guo, S. Zhang, S. H. Sun, *Angewandte Chemie-International Edition* 2013, **52**, 8526.

12.   G. Wu, P. Zelenay, Accounts Chem Res 2013, **46**, 1878.

13.   K. P. Gong, F. Du, Z. H. Xia, M. Durstock, L. M. Dai, *Science* 2009, **323**, 760.

14.   J. Liang, Y. Jiao, M. Jaroniec, S. Z. Qiao, *Angewandte Chemie-International Edition* 2012, **51**, 11496.

15.   S. Y. Wang, E. Iyyamperumal, A. Roy, Y. H. Xue, D. S. Yu, L. M. Dai, *Angewandte Chemie-International Edition* 2011, **50**, 11756.

16.   J. T. Zhang, Z. H. Zhao, Z. H. Xia, L. M. Dai, *Nat Nanotechnol* 2015, **10**, 444.

17.   Z. Yang, Z. Yao, G. F. Li, G. Y. Fang, H. G. Nie, Z. Liu, X. M. Zhou, X. Chen, S. M. Huang, *Acs Nano* 2012, **6**, 205.

18.   G. Wu, K. L. More, C. M. Johnston, P. Zelenay, Science 2011, **332**, 443.

19.   H. L. Jiang, Y. H. Zhu, Q. Feng, Y. H. Su, X. L. Yang, C. Z. Li, *Chem-Eur J* 2014, **20**, 3106.

20.   L. J. Yang, S. J. Jiang, Y. Zhao, L. Zhu, S. Chen, X. Z. Wang, Q. Wu, J. Ma, Y. W. Ma, Z. Hu, *Angewandte Chemie-International Edition* 2011, **50**, 7132.

21.   D. C. Higgins, M. A. Hoque, F. Hassan, J. Y. Choi, B. Kim, Z. W. Chen, *Acs Catal* 2014, **4**, 2734.

22.   Y. X. Zhang, J. Zhang, D. S. Su, *Chemsuschem* 2014, **7**, 1240.

23.   W. W. Gao, X. Feng, T. Y. Zhang, H Huang, J. Li and W. B. Song, ACS Appl. Mater. Interfaces, 2014, 6, 19109.

24.   G. Merle, M. Wessling, K. Nijmeijer, *J Membrane Sci* 2011, **377**, 1.

25.   S. Jun, S. H. Joo, R. Ryoo, M. Kruk, M. Jaroniec, Z. Liu, T. Ohsuna, O. Terasaki, *J. Am. Chem. Soc.* 2000, **122**, 10712.

26.   S. H. Joo, S. J. Choi, I. Oh, J. Kwak, Z. Liu, O. Terasaki, R. Ryoo, *Nature* 2001, **412**, 169.

27.   S. Jun, S. H. Joo, R. Ryoo, M. Kruk, M. Jaroniec, Z. Liu, T. Ohsuna, O. Terasaki, *J. Am. Chem. Soc.* 2000, **122**, 10712.

28.   H. W. Liang, W. Wei, Z. S. Wu, X. L. Feng, K. Mullen, *J. Am. Chem. Soc.* 2013, **135**, 16002.

29.   J. X. Xu, Y. Zhao, C. Shen, L. H. Guan, *Acs Appl Mater Inter* 2013, **5**, 12594.

30.   R. L. Liu, D. Q. Wu, X. L. Feng, K. Mullen, *Angewandte Chemie-International Edition* 2010, **49**, 2565.

31.   F. Jaouen, E. Proietti, M. Lefevre, R. Chenitz, J. P. Dodelet, G. Wu, H. T. Chung, C. M. Johnston, P. Zelenay, Energ Environ Sci 2011, **4**, 114.

32.   V. Bambagioni, M. Bevilacqua, C. Bianchini, J. Filippi, A. Marchionni, F. Vizza, L. Q. Wang, P. K. Shen, *Fuel Cells* 2010, **10**, 582.

33.   E. Antolini, *J Power Sources* 2007, **170**, 1.

34.   J. J. Bozell, G. R. Petersen, Green Chem 2010, **12**, 539.

35.   D. Zhao, J. Feng, Q. Huo, N. Melosh, G. H. Fredrickson, B. F. Chmelka, G. D. Stucky, *Science.* 1998, **279**, 548.

36.   P. Chen, L. K. Wang, G. Wang, M. R. Gao, J. Ge, W. J. Yuan, Y. H. Shen, A. J. Xie, S. H. Yu, *Energ Environ Sci* 2014, **7**, 4095.

37.   H. Wang, X. J. Bo, Y. F. Zhang, L. P. Guo, *Electrochim. Acta* 2013, **108**, 404.

38.   D. Y. Zhao, Q. S. Huo, J. L. Feng, B. F. Chmelka, G. D. Stucky, *J. Am. Chem. Soc.* 1998, **120**, 6024.

39.   Z. Y. Zhang, G. M. Veith, G. M. Brown, P. F. Fulvio, P. C. Hillesheim, S. Dai, S. H. Overbury, *Chem. Commun.* 2014, **50**, 1469.

40.   A. H. Lu, F. Schuth, *Adv. Mater.* 2006, **18**, 1793.

41.   W. Kicinski, M. Szala, M. Bystrzejewski, Carbon 2014, **68**, 1.

42.   D. Y. Zhang, Y. Hao, L. W. Zheng, Y. Ma, H. X. Feng, H. M. Luo, *J Mater Chem A* 2013, **1**, 7584.

43.   L. Lin, Q. Zhu, A. W. Xu, *J. Am. Chem. Soc.* 2014, **136**, 11027.

44.   T. Y. Ma, J. R. Ran, S. Dai, M. Jaroniec and S. Z. Qiao, *Angew. Chem., Int. Ed.* 2015, **54**, 4646–4650.

45.   J. J. Shi, X. J. Zhou, P. Xu, J. L. Qiao, Z. W. Chen and Y. Y. Liu, *Electrochim. Acta*, 2014, **145,** 259–269.

46.   Y. Gorlin, C. J. Chung, D. Nordlund, B. M. Clemens and T. F. Jaramillo, *ACS Catal.,* 2012, **2**, 2687–2694.

47.   Q. Li, R. Cao, J. Cho and G. Wu, *Adv. Energy Mater.*, 2014, **4,** 1301415.

48.   Z. C. Wang, L. Xin, X. S. Zhao, Y. Qiu, Z. Y. Zhang, O. A. Baturina, W. Z. Li, *Renew Energ* 2014, **62**, 556.

49.   Q. G. He, Q. Li, S. Khene, X. M. Ren, F. E. Lopez-Suarez, D. Lozano-Castello, A. Bueno-Lopez, G. Wu, *J Phys Chem C* 2013, **117**, 8697.

50.   L. Xin, Z. Y. Zhang, J. Qi, D. J. Chadderdon, Y. Qiu, K. M. Warsko, W. Z. Li, *Chemsuschem* 2013, **6**, 674.

51.   E. L. Kunkes, D. A. Simonetti, R. M. West, J. C. Serrano-Ruiz, C. A. Gartner, J. A. Dumesic, *Science* 2008, **322**, 417.

52.   L. P. Zhang and Z. H. Xia, *J. Phys. Chem. C*, 2011, **115,** 11170-11176.

53.   S. Y. Wang, L. P. Zhang, Z. H. Xia, A. Roy, D. W. Chang, J. B. Baek and L. M. Dai, *Angew. Chem., Int. Ed.*, 2012, **51,** 4209–4212.

54.   Y. Qiu, L. Xin and W. Z. Li, *Langmuir*, 2014, **30,** 7893–7901.

CHAPTER 4 ELECTROCATALYTIC OXYGEN EVOLUTION OVER SUPPORTED SMALL AMORPHOUS NI-FE NANOPARTICLES IN ALKALINE ELECTROLYTE[2]

4.1 Introductions

As global demand of energy increasing rapidly, intensive research and development have been devoted to novel technologies for conversion and storage of sustainable energy sources, such as water splitting to H_2 fuel, CO_2 reduction to fuels, and biomass upgrading to biofuels.[1-8] However, the electrocatalytic oxygen evolution reaction (OER, $2H_2O \leftrightarrow 4H^+ + O_2 + 4e^-$ in acidic media, or $4OH^- \leftrightarrow 2H_2O + O_2 + 4e^-$ in basic media) often coupled with these processes at the anode is a slow reaction that requires an overpotential in substantial excess of its thermodynamic potential (1.23 V vs. RHE, at standard temperature and pressure) to deliver an acceptable current density, *e.g.* 10 mA cm^{-2} (based on 10% efficiency of solar-to-fuel conversion).[9-12] Many research efforts have been intensively focused on this reaction, targeting to seek more efficient OER electrocatalysts at lower overpotential to reduce input energy cost.[6, 11, 13] IrO_2 and RuO_2 have been identified as the most active catalysts for OER, however, the scarcity and high cost of these precious metals makes them undesirable for wide-spread applications.[2, 6, 14] Therefore, exploring efficient and durable catalysts based on earth-abundant metals has been the focal point of current researches. Although various first-row transition monometal oxides, such as CoO_x, and MnO_x with different structures were synthesized, and exhibited promising

---

[2] The material contained in this chapter was previously published in Langmuir (American Chemical Society), 2014, 30, 7893, "Electrocatalytic Oxygen Evolution over Supported Small Amorphous Ni-Fe Nanoparticles in Alkaline Electrolyte". Reprinted with permission from (Yang, Q., Xin, L., Li, W. Z., Electrocatalytic Oxygen Evolution over Supported Small Amorphous Ni-Fe Nanoparticles in Alkaline Electrolyte, 2014, 30, 7893). Copyright (2014) American Chemical Society, shown in **Appendix B**

activity towards OER,[15-20] they still underperformed the IrO_2 and RuO_2 due to the strength of M-O bond on their specific defect being too strong or too weak.[21] Therefore, more complex catalysts with multi-components have been studied.[22-24] For example, Suntivich et al. have demonstrated the intrinsic OER activities on a series of perovskite oxides through plotting a volcano- shape graph, and found that the $Ba_{0.5}Sr_{0.5}Co_{0.8}Fe_{0.2}O_{3-\delta}$ (BSCF) showed the highest activity for OER.[25] However, the large particle size (~200 nm) of perovskite oxides leads to quite small surface areas, thus limiting further mass activity enhancement. Recently, the Ni-Fe bimetallic system has been investigated and was found to be able to serve as efficient OER catalyst.[26-28] Dai and his coworkers successfully prepared a Ni−Fe layered double hydroxide-multiwall carbon nanotube (MWCNT) complex with an average size of 50 nm via a hydrothermal synthesis method. They proposed that the Fe^{3+} replaces Ni^{2+} in the crystalline α-$Ni(OH)_2$ of the layered double hydroxide structure, which results in high activity of OER.[29] Corrigan et al. electrodeposited iron impurity in nickel oxide thin film, and found that the directly incorporated iron can also increase the OER activity of Ni film catalyst.[30, 31] Subsequently, a variety of Ni-Fe-based catalysts of thin film geometry were prepared, such as evaporation-induced self-assembly (EISA) Ni-Fe oxide thin film by Grosso et al.[32] Landon et al. reported that in NiO and Fe_2O_3 coexisted thin film structure, the crystalline $NiFe_2O_4$ could be a contributing phase to the enhanced OER activity.[26] On the other hand, Bell et al. used in-situ Raman spectroscopy to demonstrate the oxidation states of Ni and Fe, as well as the corresponding structure of Fe in Ni-Fe thin film. The results also implied that the presence of Fe can also promote the OER activity in NiO_x film without observation of any crystalline $NiFe_2O_4$.[33] It has been well recognized that the catalyst surface area will

strongly influence the mass activity of catalysts. A nanoparticle catalyst with smaller size can provide more active sites to achieve a higher OER activity on a mass basis.[16, 34] In addition, catalysts with smaller nanoscale dimensions and higher OER activity can be readily fabricated into practical electrochemical cells. However, few researches so far have been focused on small Ni-Fe nanoparticles as an OER electrocatalyst.

Herein, we present synthesis of 4 nm amorphous Ni-Fe nanoparticles supported on XC-72 carbon black via a modified organic solution phase reduction method. Low crystallinity in NiO_x or FeO_x nanoparticles was characterized by XRD and TEM-SAED. The amorphous Ni-Fe structure has shown surprisingly high OER activity in alkaline media, which outperforms most Ni-Fe thin films previously reported and a commercial carbon supported Ir nanoparticle catalyst. Moreover, the high stability and Faradaic efficiency of OER achieved on the amorphous Ni-Fe nanoparticle catalysts suggest promising opportunities for practical sustainable energy conversion and storage applications in the future.

4.2 Experimental

4.2.1 Preparation of carbon supported Ni-Fe nanoparticles

All carbon black supported Ni-Fe nanoparticle catalysts were prepared through a modified organic solution phase nanocapsule approach, which has been reported elsewhere.[35-37] The brief synthesis procedure for the Ni-Fe catalysts with a metal loading of *ca.* 20 wt% is described as follows. Ni(acac)$_2$ (Aldrich Chemistry, 95%), Fe(acac)$_2$ (Aldrich Chemistry, 99.95%), and Vulcan XC-72 carbon black (FuelCell Store) were mixed in 25 ml benzyl ether (Alfa Aesar, 98%). The stoichiometry of each metal precursor was varied based on the targeting ratios of Ni to Fe. Note, the Fe precursor was added with 200% excess of the stoichiometric amount because Fe^{2+} could not be completely reduced under the synthesis

conditions. (*e.g.* for the synthesis of $Ni_{0.5}Fe_{0.5}O_x/C$, 0.25 mmol $Ni(acac)_2$+0.25×3 mmol $Fe(acac)_2$ was used). Then, the mixed solution was heated to 60 °C under nitrogen flow, and the surfactants (oleylamine OAM (Aldrich, 70%), oleic acid OAc (Aldrich, 95%)) were added into the system, followed by maintaining for 5 min to ensure complete dissolution of precursors and surfactants. As the temperature was further increased to 120 °C, $LiBEt_3H$ (1.0 M in THF, Acros Organics) was quickly injected, and held for 30 min. Then, the temperature was rapidly ramped to 180 °C and kept for an additional 1 h. The carbon supported Ni-Fe catalysts were finally collected after filtration, washing with copious ethanol (Pharmco-Aaper, 200 proof), and drying in a vacuum oven at 50 °C for 24 h.

4.2.2 Physical Characterizations

The metal loading and composition of catalyst was analyzed by inductively coupled plasma optical emission spectroscopy (ICP-OES Optima 7000 DV, Perkin-Elmer). The specimen was prepared by dissolving 10 mg of catalyst into 4 ml of fresh aqua regia, followed by diluting to 250 ml with the deionized water (18.2 MΩ). The catalyst crystallinity was characterized by using Scintag XDS-2000 θ/θ diffractometer with Cu Kα radiation (λ = 1.5406 Å), with a tube current of 35 mA and a tube voltage of 45 kV. Transmission electron microscopy (JEOL JEM-2010) was utilized to determine the catalyst morphology, size, and 135 diffraction pattern with an operation voltage of 200 kV

4.2.3 Electrochemical Characterization and OER tests

Electrochemical characterizations and tests were performed in an electrochemical cell (AFCELL3, Pine Instrument). A rotating disk electrode (RDE) and rotating ring disk electrode (RRDE) were used for examination of OER kinetics without interference of mass transfer effects, and for analysis of OER Faradaic efficiency, respectively. A coiled

platinum counter electrode, which was isolated by a fritted glass tube from the main test electrolyte, and Hg/HgO (MMO) reference electrode with 1.0 M KOH filling solution were used throughout the electrochemical characterizations. The 1.0 M KOH electrolytes prepared from bioxtra grade (Macron, 86%) and semiconductor grade (Aldrich, 99.99%) was used for testing the OER activity and Faradaic efficiency of Ni-Fe electrocatalysts, respectively. A 2.0 mg ml^{-1} solution of catalyst ink was prepared by dispersing carbon supported Ni-Fe nanoparticles in isopropanol, followed by ultrasonication until no aggregation was visible. The catalyst ink of 15 µl was then dropped onto the surface of glassy carbon electrode with a 0.19625 cm^2 area, and 10 µl of 0.05 wt% diluted Nafion solution (Ion Power, Inc., 5 wt%, 1100EW) was finally added on the top to fix the catalyst particles.

The standard electrode potential of Hg/HgO/1.0 M KOH (MMO) was 0.098 V vs. SHE based on the manufacturer's specification. Then, the potential of the Hg/HgO/1.0 M KOH reference electrode was calculated to be 0.924 V vs. the reversible hydrogen electrode (RHE) at pH 14. Thus, the reversible potential of water oxidation, 1.23V vs. RHE at pH 14 could be calculated as 0.306 V vs MMO at pH 14 (1.23 V - 0.924 V = 0.306 V). And the overpotential η was calculated using following equation:

$$\eta = E_{applied} - E_{rev} - R_u \times i \tag{1}$$

where $E_{applied}$ is the applied potential vs. MMO in 1.0 M KOH; R_u is the compensated resistance; i is measured current; E_{rev} is the reversible potential of OER vs. MMO (0.306 V vs.MMO at pH 14). The compensated resistance, R_u, between working and reference electrodes was determined to be ~15 Ω in 1.0 M KOH electrolyte by a single-point high-

frequency impedance method at 300 mV overpotential, and all the potentials reported were IR-compensated to 85%. [6, 29] All experimental results of OER activity on Ni-Fe catalysts were reported as current density versus iR corrected applied potential (vs. MMO) and overpotential. The current densities are normalized by using geometric surface areas.

Cyclic voltammetry: The OER activity of Ni-Fe catalysts was determined using cyclic voltammetry (CV). The 1.0 M KOH electrolyte was deaerated by pure oxygen gas for 30 min prior to each experiment. The surfactant removal was firstly carried out by scanning from -0.8 to 0.65 V (vs. MMO) with 1000 mV s^{-1} scan rate for 50 cycles, followed by catalyst activation in a potential range of 0 to 0.65 V (vs. MMO) with scan rate of 50 mV s^{-1} for 10 cycles. The polarization curves were subsequently obtained using a scan rate of 5 mV s^{-1} between 0 and 0.8 V (vs. MMO).

Calculation of the Turnover Frequency (TOF): The TOF is defined as per total metal atoms including subsurface metal per second, and the equation is shown as follows: which has been widely used in previous works.[3, 6, 10, 16, 33]

$$TOF = \frac{I}{4 \times F \times m}$$

(2)

where I is measured current at a certain overpotential; F is the faraday constant with a value of 96485 C mol^{-1}; m is the number of moles of the total active metals drop-casted on the glassy carbon electrode.

This TOF is estimated by assuming all of the active metal atoms in the catalysts drop-casted on the glassy carbon electrode are catalytically active for OER. However, this is a gross underestimate of the real TOF, which should be the lower bound, TOF$_{min}$, because

the porous structure of carbon supporting materials could inhibit the perfect connection between the electrolyte and catalysts, and some of subsurface active material atoms might not be accessible for catalyzing the OER.[3, 10, 16, 33]

Faradaic efficiency: The RRDE was employed to measure the OER Faradaic efficiency over the Ni-Fe catalysts with different compositions. The collection efficiency, *N*, of RRDE was determined by the current ratio between the ring and disk in 0.01 M $K_3Fe(CN)_6$ + 0.1 M KOH electrolyte, which was 23±1%.[38] This result agrees well with 25% collected efficiency calculated according to the geometry of RRDE. Pure nitrogen gas flowed into 1.0 M KOH electrolyte prior to each test for 30 min and remained throughout the electrochemical experiments to purge the system. Because of the low magnitude of ring current, the Pt ring was polished with diamond slurry (1 μm MetaDi Supreme) before the ring current collection in order to minimize the interference of the contaminants. 5 μl of 1 mg ml^{-1} catalyst ink was dropped onto the surface of disk electrode, followed by adding 3 μl diluted Nafion solution (0.05 wt %) on the top. In order to determine the background current of ring electrode, the open circuit potential of OER was applied to the disk electrode where no faradaic reaction occurs, while the Pt ring electrode was held at -0.6 V vs. MMO. The background ring current determined was typically lower than 50 μA. Then, the applied voltage was held at several potentials in the OER kinetic-limited region for 1 min, meanwhile the ring current was collected under -0.6 V vs. MMO.

4.3 Results and discussion

4.3.1 Material synthesis

The carbon supported amorphous Ni-Fe nanoparticles ($Ni_yFe_{1-y}O_x$/C) were prepared via a modified solution-phase nanocapsule method. The composition of Ni-Fe nanoparticles

were controlled by varying the ratio of two precursors ($Ni(acac)_2$ and $Fe(acac)_2$). $Fe(acac)_2$ with 200% excess was added in order to achieve the setting ratio and loading of Ni-Fe nanoparticles on the carbon black. The excess of Fe precursor was found to be necessary because Fe^{2+} could not be completely reduced under the synthesis conditions, which may be attributed to more negative redox potential of Fe^{2+}/Fe (-0.440 V vs. SHE) than noble metal catalysts, such as Pt^{2+}/Pt (1.200 V vs. SHE), Pd^{2+}/Pd (0.987 V vs. SHE), Au^{3+}/Au (1.498 V vs. SHE), etc. In addition, in contrast with noble metals, non-noble metals may have a relatively weak bonding strength with the surfactants (oleylamine and oleic acid), leading to poor control over particle size, morphology, and final composition of catalysts.[35] Through modifying the synthesis conditions, such as the molar ratio of precursors, temperature increasing rate, the duration of synthesis, etc., Fe precursor of 200% excess was found to be the optimum stoichiometry to ensure that the obtained molar ratios of Ni and Fe approach the setting compositions and metal loadings on the carbon black supporting materials, as confirmed by ICP-OES.

To obtain the amorphous structure of Ni-Fe nanoparticles, post-heat treatment was not performed. Nanoparticle aggregation, which often occurs at high temperatures and can lead to a significant decrease in the catalyst surface area and active sites, was minimized under such mild synthesis conditions of the nanocapsule method.[36]

On the other hand, the surfactants may bond at the metal surface, resulting in a blocking for catalytic active sites, which can strongly affect the oxygen evolution reaction (OER) performance of Ni-Fe catalysts. Therefore, copious ethanol was used to wash the catalysts, which has been found to enable surfactant removal to <5 wt% of final catalyst content.[36] In order to further minimize the interference of surfactant possibly presented after ethanol

washing, cyclic voltammetry scan with 1 V s^{-1} was performed until the anodic wave

become stabilized before obtaining the OER activity over the Ni-Fe electrocatalyst.

4.3.2 Physical characterization

The metal loadings (Ni + Fe) of all catalysts were calculated through the total weights of

Ni and Fe detected by ICP-OES divided by total weight of Ni_yFe_{1-y}/C determined by

weighing balance, as shown in the following equations:

$$\frac{(weight\ of\ Ni)_{determined\ by\ ICP-OES} + (weight\ of\ Fe)_{determined\ by\ ICP-OES}}{(Total\ weight\ of\ Ni_yFe_{1-y}/C)_{determined\ by\ balance}} = Metal\ loading$$

(3)

Because of the existence of small amounts of surfactant on the surface of as-prepared

catalysts, and the formation of FeO_x and NiO_x as the sample is exposed to the air, the metal

loadings (Ni + Fe) of all the catalysts has been found ~15 wt%, which is lower than the

setting loading of 20 wt% for all the samples.[39] The metal compositions of as-prepared Ni-

Fe catalysts were also obtained by ICP-OES, as shown in **Table 4** and the Ni:Fe molar

ratio varied from 0.83:0.17 to 0.25:0.75.

Table 5 Summary of actual Ni-Fe composition and average particle sizes of $Ni_yFe_{1-y}O_x/C$ catalysts.

Target Ni:Fe compsition	1:0	0.8:0.2	0.7:0.3	0.5:0.5	0.3:0.7	0:1
Actual Ni:Fe composition	1:0	0.83:0.17	0.69:0.31	0.46:0.54	0.25:0.75	0:1
Average particle size / nm	3.7	4.1	4.4	4.4	4.2	3.4

XRD was employed to characterize the crystallinity of supported Ni-Fe nanoparticles by

scanning from 10 to 100°, and the patterns are shown in **Figure 4.1**, and compared with

polycrystalline NiO (Joint Committee on Powder Diffraction JCPDS card 04-0835) and γ-

Fe_2O_3 (JCPDS card 39-1346) standards. Low intensity of all characteristic crystalline

diffraction peaks was observed, except for the peak related to the graphite (002) facet at

~25°, which suggests that the NiO_x, FeO_x, and $Ni_yFe_{1-y}O_x$ nanoparticles predominantly feature amorphous structures. For the NiO_x/C, only three weak peaks at 37.3°, 43.3°, and 62.9° were exhibited, representing the NiO (111), (200), and (220) facets, respectively. With the increasing Fe content, the characteristic peaks of γ-Fe_2O_3 (311), (400) facet at 35.6° and 44.2° were displayed, while the characteristic NiO diffraction peaks gradually disappeared. The two small sharp peaks of 23.2° and 25.8° are observed on FeO_x/C, which are probably assigned to the diffraction peaks of γ-Fe_2O_3 (210) and (211) facets. By analyzing all characteristic peaks in XRD patterns, it may be concluded that small amounts of γ-Fe_2O_3 with low crystallinity are contained in the predominantly amorphous phase in FeO_x and $Ni_yFe_{1-y}O_x$ nanoparticles.[40] However, due to the low intensity and close position of NiO and γ-Fe_2O_3 standard diffraction peaks, the XRD patterns could not reveal the exact crystalline phase in the low crystalline Ni-Fe nanoparticles. In addition, the XRD patterns provided no evidence for alloyed $NiFeO_x$ and $NiFe_2O_x$ crystals. Therefore, it further confirms that the hypothesized crystalline phases in Ni-Fe nanoparticles are γ-Fe_2O_3 rather than alloyed nickel iron oxides, and the Ni-Fe catalysts are predominantly amorphous.[41] After comparing a variety of standard crystalline Fe oxides (*e.g.* α-Fe_2O_3, γ-Fe_2O_3, Fe_3O_4), only the standard XRD pattern of γ-Fe_2O_3 is shown as the major crystalline phase in **Figure 4.1**.[40-43]

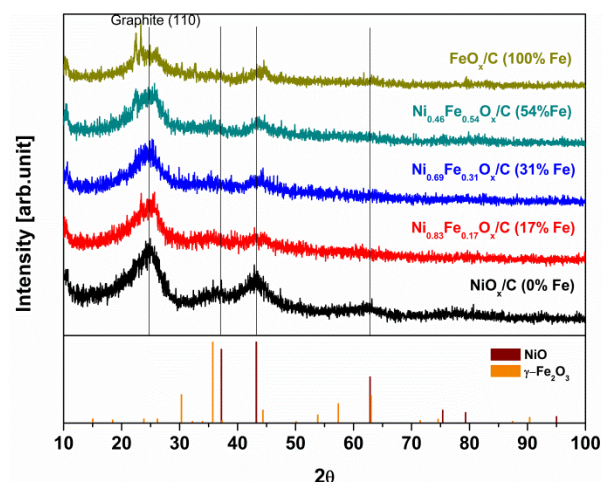**Figure 4.1** XRD patterns of as-prepared carbon supported NiO_x, FeO_x, $Ni_yFe_{1-y}O_x$ nanoparticles with different Fe content; Patterns of NiO [Joint Committee on Powder Diffraction (JCPDS) card 04-0835] and γ-Fe_2O_3 (JCPDS card 39-1346) standards are shown in the bottom.

TEM images were used to directly observe the Ni-Fe particle size and size distribution, and selected area electron diffraction (SAED) patterns were employed to investigate the amorphous structure of the Ni-Fe catalysts. From the TEM images and corresponding histograms, all Ni-Fe catalysts were found to be uniform nanoparticles with good dispersion and narrow size distribution (from 2.0 to 6.5nm), centered at *ca*. 4 nm based on counting of 250 randomly chosen particles in an arbitrarily chosen area, as shown in Figure 2. The average Ni-Fe nanoparticle diameters obtained from TEM are summarized in **Table 5**. In addition, if high crystalline nickel, iron oxides or Ni-Fe alloyed are present, one would expect either a matrix of sharp, bright disks in TEM-SAED patterns as shown in **Figure 4.2**. However, only blurred disks were observed, indicating a predominantly amorphous structure for the as-prepared Ni-Fe catalysts, which is consistent with XRD patterns. Some nearly unnoticeable bright spots with blurred circles were displayed in FeO_x/C, indicating that small amounts of low crystalline Fe oxides were contained in amorphous Ni-Fe phase.
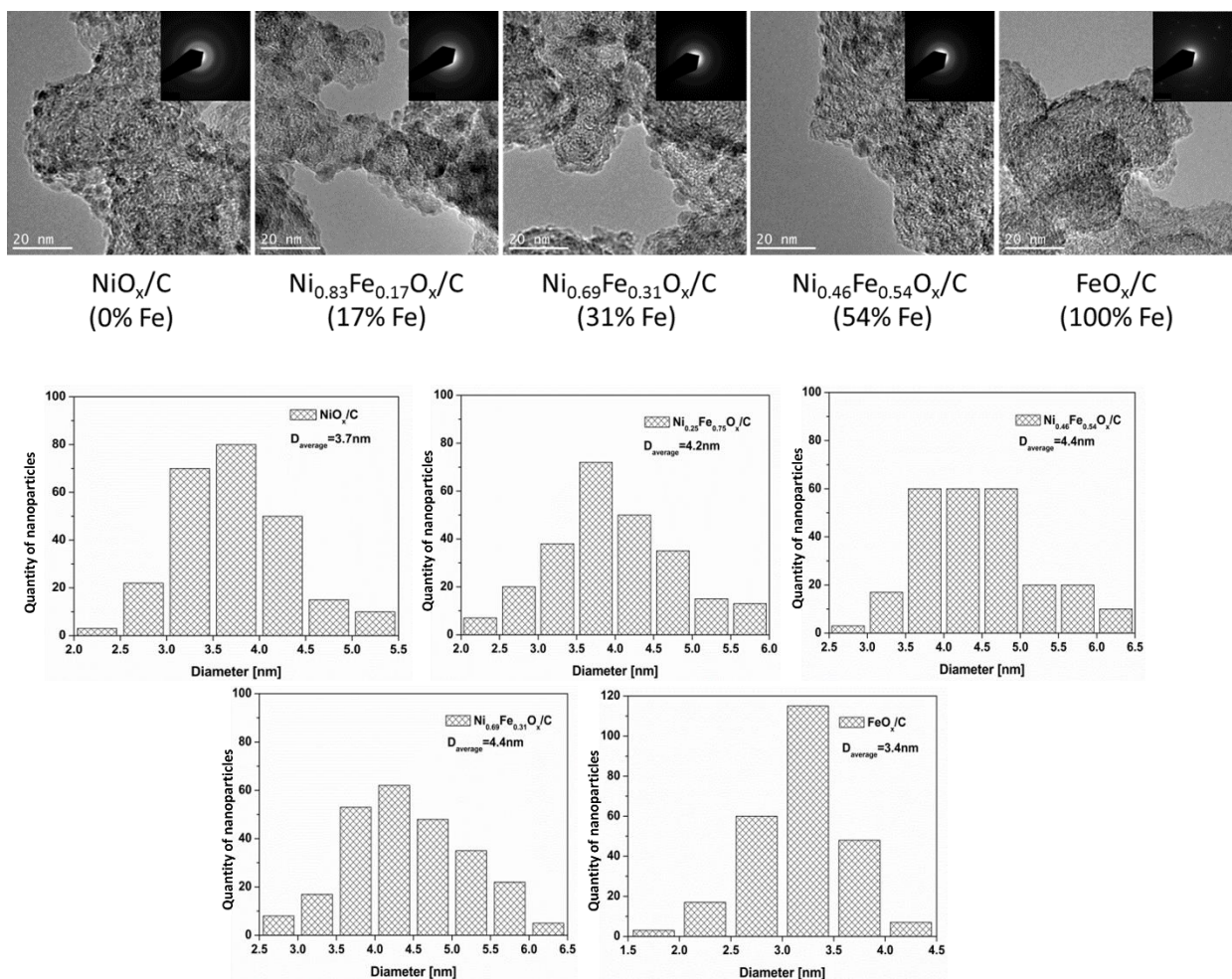
Figure 4.2 TEM images, corresponding selected area electron diffraction (SAED) patterns, and particle diameter histograms of carbon supported NiO_x, FeO_x, $Ni_yFe_{1-y}O_x$ nanoparticles.

4.3.3 Electrochemical Characterizations

Cyclic voltammetry of OER: The cyclic voltammograms of carbon supported amorphous Ni-Fe catalysts are shown in **Figure 4.3a**. In 1.0 M KOH electrolyte, the NiO_x/C and FeO_x/C catalysts exhibited significant differences in both characteristic redox peaks and OER activity. The NiO_x/C displayed redox peaks at the overpotential of 52 mV and 140 mV (0.358 and 0.446V vs MMO) during anodic and cathodic scan, which resulted from the transformation of $Ni(OH)_2$ and NiOOH ($Ni(OH)_2 + OH^- \leftrightarrow NiOOH + H_2O + e^-$) in alkaline electrolyte, whereas the FeO_x/C did not show any observable current density in the overpotential range <350 mV.[44, 45] However, it should be mentioned that Fe oxide also

has redox peaks at potentials between -1.2 and -0.6 V (vs. MMO) in alkaline electrolyte, which is out of the overpotential range studied.[46]
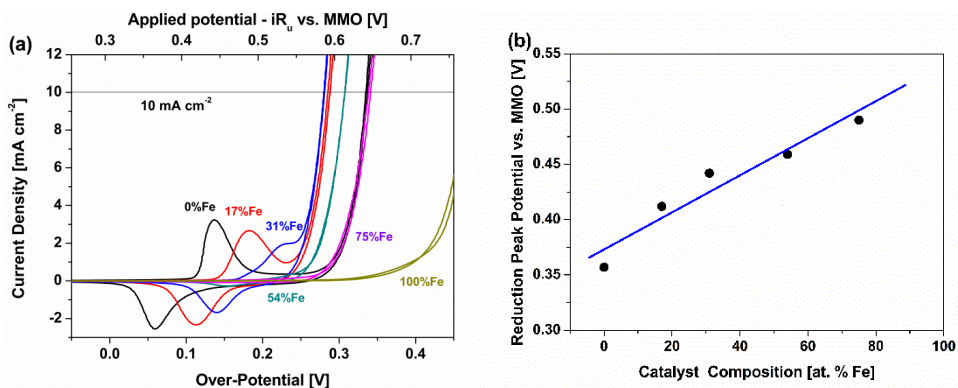

Figure 4.3 a) Cyclic voltammograms of carbon supported NiO_x, FeO_x, $Ni_yFe_{1-y}O_x$ nanoparticles collected at 5 mV s^{-1} and 1600 rpm in O_2 saturated 1.0 M KOH; **b)** Reduction peak potential as a function of the Fe content. Line demonstrates linear fit to the data.

For Ni-Fe bimetallic catalysts, the $Ni(OH)_2$/NiOOH redox peaks were positively shifted with increasing Fe composition, while the redox peaks area decreased simultaneously.[30, 31, 33, 36] When the Fe composition was above 54%, the electrochemical oxidation and reduction peaks became less pronounced, and the oxidation peak was even overlapped with the rapidly increased OER current. Addition of Fe may suppress the electrochemical oxidation of $Ni(OH)_2$ to NiOOH, and the number of electrons transferred per Ni atom could also be changed.[34] In order to reveal the effect of Fe content on OER activity of Ni-Fe catalysts, the reduction peak position as a function of Fe content was plotted, as shown in **Figure 4.3b**. A linear correlation between the position of the reduction peak and Fe content is obtained, where higher incorporated Fe content gives rise to a more positive shift of reduction peak. However, the OER activity of the Ni-Fe catalysts is not monotonically enhanced with increasing of Fe content. The $Ni_{0.69}Fe_{0.31}O_x$/C, which is examined with the optimal Fe content, exhibited the highest OER activity with a 280 mV overpotential at 10 mA cm^{-2} in 1.0 M KOH, compared to 335 mV overpotential observed on monometallic

NiO_x/C catalyst. The significant enhancement of the OER activity indicates that the Fe involved in the amorphous Ni-Fe catalyst closely interacts with Ni. When the Fe content was further increased, the OER activity of Ni-Fe catalysts decreases. For instance, the OER overpotential on $Ni_{0.25}Fe_{0.75}O_x$/C at 10 mA cm^{-2} increased to 341 mV, which is close to 335mV overpotential of monometallic NiO_x/C. This activity drop is probably ascribed to the decreasing of Ni active sites on catalyst surface with the addition of more Fe. However, due to the complex amorphous structure of Ni-Fe catalysts, the mechanisms of OER activity varying with Fe contents still needs to be further investigated. It should be mentioned that the optimal Fe content varies from 10 to 50% for different Ni-Fe OER catalysts, as reported in previous publications. This may be due to different catalysts morphology and structure (crystallization *vs*. amorphous) resulting from synthesis methods, and electrode preparation techniques.[15-20] In addition, the 280 mV overpotential on $Ni_{0.69}Fe_{0.31}O_x$/C catalyst at 10 mA cm^{-2} is also lower than the 305 mV overpotential on the well-known most active Ir/C, as shown in **Figure 4.4a**. Because IrO_x has been found to be unstable in basic solution in the high current density region, the recorded first cycle voltammogram was recorded for this comparison. Thus, the *ca.* 25 mV overpotential difference at 10 mA cm^{-2} between $Ni_{0.69}Fe_{0.31}O_x$/C and Ir/C indicates higher OER activity for the amorphous Ni-Fe catalysts. Moreover, in order to investigate the effect of carbon supporting material on $Ni_yFe_{1-y}O_x$/C OER activity, a blank CV test on carbon black (without metal nanoparticles) was carried out under the same experimental conditions. Interestingly, very low current density was observed at the overpotentials region of <450 mV, indicating a sluggish OER activity over the carbon black. Thus, the high OER

performance achieved on the reported $Ni_yFe_{1-y}O_x$/C catalysts is contributed by Ni-Fe

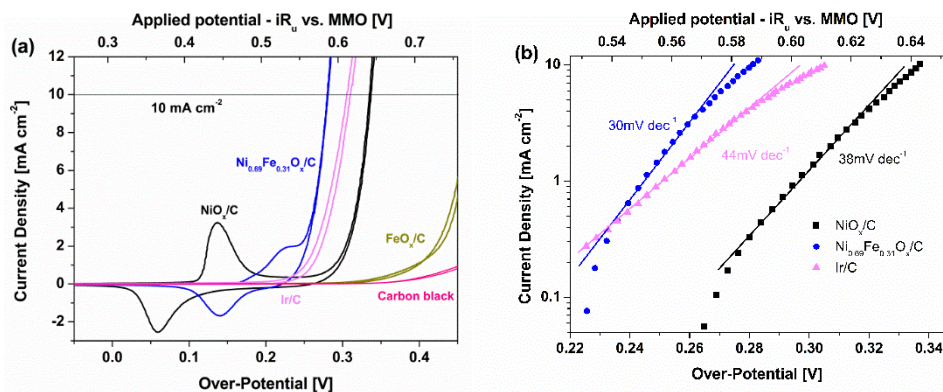bimetallic nanoparticles, rather than the carbon black supporting material.

Figure 4.4 a) Cyclic voltammograms of carbon supported NiO_x, FeO_x, $Ni_{0.69}Fe_{0.31}O_x$, Ir nanoparticles, and carbon black; **b)** Tafel plots of carbon supported Ir, NiO_x, and $Ni_{0.69}Fe_{0.31}O_x$ nanoparticles, collected at 5 mV s^{-1} and 1600 rpm in O_2 saturated 1.0 M KOH.

The Tafel plots for the carbon supported Ni-Fe and Ir catalysts in alkaline media are shown

in **Figure 4.4b**. The observed Tafel slope of $Ni_{0.69}Fe_{0.31}O_x$/C catalyst was about 30 mV

dec^{-1}, while those of NiO_x/C and Ir/C catalysts were 38 and 44 mV dec^{-1}, respectively. The

turnover frequency (TOF) of $Ni_{0.69}Fe_{0.31}O_x$/C catalyst at overpotential of 300 mV was also

calculated in 1.0 M KOH, assuming all of the active metal atoms in the catalysts drop-

casted on the glassy carbon electrode are catalytically active for OER: [3, 10, 16, 33, 48] The TOF

value of $Ni_{0.69}Fe_{0.31}O_x$/C was calculated to be 0.20 s^{-1}, which is similar to the previous

reported highest TOF of 0.21 s^{-1} for Ni-Fe thin film, and is roughly 10-fold higher than that

of reported IrO_x (0.0089 s^{-1}) catalyst, suggesting a high OER activity on amorphous Ni-Fe

nanoparticles.[48] It should be noted that the porous structure of carbon supporting materials

could affect the OER performance of the metal catalysts, since some of the Ni-Fe surface

active sites may not directly contact with the electrolyte. Therefore, the obtained TOF of

$Ni_{0.69}Fe_{0.31}O_x$/C catalyst should be the lowest boundary, and smaller than its actual TOF

value. Corrigan has reported the highest Tafel slope of 25 mV dec^{-1} for 10% Fe co-

precipitated Ni-Fe thin film, and shown a measured current of 100 mA at 287 mV overpotential in 1.0 M KOH.[30] [31] Based on their reported data, the TOF was calculated to be 0.07 s^{-1}, which is much smaller than that of the presented carbon supported amorphous $Ni_{0.69}Fe_{0.31}O_x$ nanoparticles. In addition, $Ba_{0.5}Sr_{0.5}Co_{0.8}Fe_{0.2}O_{3-\delta}$ (BSCF), reported by Suntivich et al., has a very high TOF of ~0.6 s^{-1} at 300 mV in 0.1 M KOH.[25] However, the large particle size of ~200 nm and 50 mV dec^{-1} Tafel slope of BSCF will limit its OER mass activity enhancement, particularly at high overpotential. The interaction effects between the Ni-Fe metal catalysts and the supporting material on the OER activity should be thoroughly investigated, because the porous structure of carbon black currently used may not give rise to the optimum contact between the metal catalytic sites and electrolyte. Nitrogen doped carbon nanotubes, 3D graphene or reticulated vitreous carbon could be more promising alternative supports, which are worthy of exploring in future research.

Faradaic efficiency: The Faradaic efficiency of OER can be determined by RRDE, where oxygen was produced at the center disk electrode and collected and reduced on the Pt ring electrode. Background Pt ring current was measured and corrected prior to the experiments, and then the disk electrode was applied to consecutive 1 min constant potential steps from 0.586 to 0.646 V (*vs*. MMO) at 1600 rpm rotation rate under N_2 gas blanket. The ring current was recorded at a constant potential of -0.6 V (vs. MMO), which was sufficiently negative to rapidly reduce the collected oxygen. It should be noted that only dissolved O_2 can be reduced at the surface of the ring electrode. Hence, the measured Faradaic efficiency could be lower than the actual value due to the undissolved oxygen bubbles.[6] The Faradaic efficiency can be determined as below:

$$Faradaic\ Efficiency = \frac{n_{app} \times i_r}{i_d \times N}$$

(4)

where n_{app} is apparent number of electrons; i_r and i_d are the measured ring and disk currents, respectively; N is the collection efficiency of RRDE, ~0.23 in this work.

Under the conditions of -0.6 V vs MMO in 1.0 M KOH on Pt ring electrode at rotation rate of 1600 rpm, the apparent number of electrons, n_{app} is calculated as 2, (n_{app}=ca. 2) which was reported by Jaramillo et al.[6] They investigated the apparent number of electrons for ORR on Pt ring electrode in 1.0 M KOH electrolyte, and found that the limiting ring current is strongly related to the apparent number of electrons and rotation rate of Pt ring electrode, based on the Levich equation of RRDE. [6, 49]

The disk and ring currents over $Ni_{0.69}Fe_{0.31}O_x$/C catalyst in 1.0 M KOH are plotted as a function of applied disk potential in **Figure 4.5**. The highest Faradaic efficiency, ~97%, was obtained at the applied disk potential of 0.586 V (vs. MMO), and decreased to 43% with the disk voltage increasing to 0.646 V (vs. MMO). The decreasing Faradaic efficiency might be ascribed to apparently undissolved oxygen bubbles generated at the relatively high applied potentials. Most of oxygen in the gas bubble cannot be collected by the Pt ring electrode. Thus, the 97% of Faradaic efficiency, achieved at achieved at 0.586 V (vs MMO) (obtained 1.0 mA cm^{-2} disk current density), is more representative to the OER efficiency on the Ni-Fe catalysts, because such a disk current density is sufficiently high to generate dissolved oxygen, while satisfactorily low to suppress local oxygen bubble formation at the surface of disk electrode. The Faradaic efficiency of ~97% suggests that the disk current is dominantly attributed to OER, rather than non-OER reactions (*e.g.* carbon corrosion, further oxidation of nanoparticle catalyst, *etc.*).
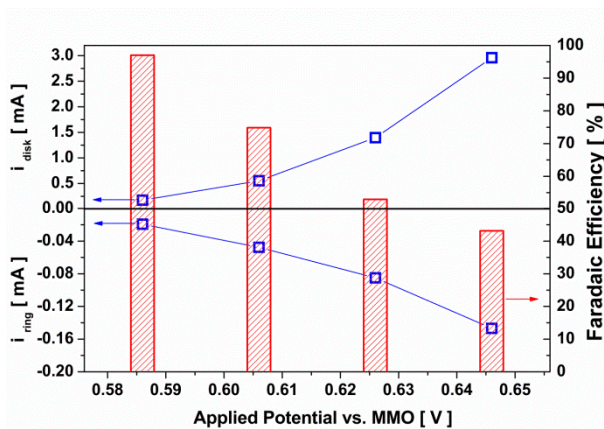
Figure 4.5 The Faradaic efficiency measurement for carbon supported $Ni_{0.69}Fe_{0.31}O_x$ catalyst in 1.0 M KOH at 1600 rpm under N_2 saturation. The disk and ring current of RRDE is plotted as a function of applied disk potential.

Catalyst Stability: The short term stability of the optimized $Ni_{0.69}Fe_{0.31}O_x$/C catalyst was investigated by chronoamperometry. Current density of 10 mA cm^{-2} was held for 6 hours at a rotation rate of 1600 rpm. The cyclic voltammogram was collected after each hour to study the change in the OER activity on $Ni_{0.69}Fe_{0.31}O_x$/C, and the results are shown in **Figure 4.6a**. It is exciting to observe that after a 6h test, the cyclic voltammograms show no apparent change, implying the Ni-Fe catalyst was not deactivated in 1.0 M KOH. Bell and his coworkers found that the redox couple of NiO_x thin film will shift to higher overpotential in alkaline media after several hours of anodization, which is ascribed to transformation of disordered γ-NiOOH to ordered β-NiOOH.[33] However, the slight increasing of redox peaks area without position shift of redox couple is observed in the $Ni_{0.69}Fe_{0.31}O_x$/C catalyst stability tests, which could be explained as the incorporated Fe can influence the transformation of disordered γ-NiOOH to ordered β-NiOOH, and more Ni surface sites will be exposed to electrolyte and became electrochemically active during the anodization.[16, 33]

In order to further investigate the stability of as-prepared Ni-Fe nanoparticle catalysts, TEM was employed to reveal the nanoparticle size change before and after 6 hours of anodization. The particle aggregation often occurs under high current density, and has been identified as one of the main reasons leading to the drop of catalyst activity, owing to the reduced electrochemical active surface area. However, it was interesting to observe nearly no catalyst particle aggregation after 6 hours constant current anodization, as shown in **Figure 4.6c** (TEM images for $Ni_{0.69}Fe_{0.31}O_x$/C before and after 6 hours OER test). The average $Ni_{0.69}Fe_{0.31}O_x$ particle size measured after 6 hours OER was about 4.6 nm, which is very close to the initial value of 4.4 nm for the fresh catalyst. This negligible size change of $Ni_{0.69}Fe_{0.31}O_x$ nanoparticles further confirms the robust stability for the presented small amorphous Ni-Fe nanoparticle catalysts.

In addition, the stability of commercial Ir/C in 1.0 M KOH has also been studied for comparison with the amorphous Ni-Fe nanoparticle catalysts. **Figure 4.6b** shows the overpotential as the function of time for carbon supported $Ni_{0.69}Fe_{0.31}O_x$ and Ir for 2 hours. The Ni-Fe catalyst exhibited a surprisingly high electrochemical stability: the overpotential of the $Ni_{0.69}Fe_{0.31}O_x$ catalyst at 10 mA cm^{-2} was maintained around 285 mV during the 2 hours test. The slight increase of overpotential during the first 60 minutes for Ni-Fe catalyst resulted from oxygen bubbles accumulating at the surface of electrode. After removal of the bubbles by lifting the working electrode out of the electrolyte and rotating it, the measured OER overpotential reduced to the initial value. On the contrary, the OER overpotential on iridium catalyst at 10 mA cm^{-2} was tremendously increased from 286 mV to 480 mV during 2 hours of anodization, indicating that Ir/C catalyst is very unstable in 1.0 M KOH. This could be explained by the oxidation of the surface IrO_x to water-soluble

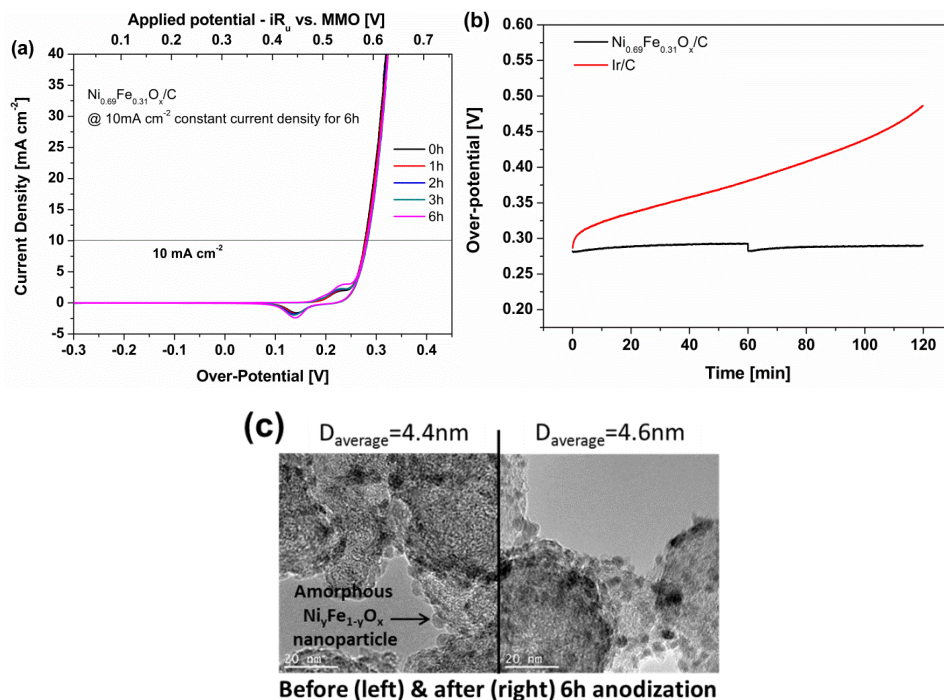IrO_4^{2-} or other water-soluble solvated Ir(VI) ions, which has been reported in previous literatures.[50-52]

Figure 4.6 a) Cyclic voltammograms of carbon supported $Ni_{0.69}Fe_{0.31}O_x$, nanoparticles, collected hourly at 5 mV s^{-1} and 1600 rpm in O_2 saturated 1.0 M KOH during 6 hours constant current density (10 mA cm^{-2}) anodization test; **b)** the plots of overpotential as a function of time for carbon supported $Ni_{0.69}Fe_{0.31}O_x$ and Ir catalysts recorded under 10mA cm^{-2} constant current density at 1600 rpm in O_2 saturated 1.0M KOH; c) TEM images of carbon supported $Ni_{0.69}Fe_{0.31}O_x$ before and after 6 hours constant current density anodization test.

4.4 Conclusions

We have successfully synthesized carbon supported amorphous Ni-Fe nanoparticle catalysts with an average size of 4 nm through a solution-phase reduction route. XRD and TEM-SAED characterizations showed that all Ni-Fe catalysts are predominantly amorphous containing small crystalline phase. The highest OER activity of catalysts was observed on 31% Fe content Ni-Fe bimetallic catalyst ($Ni_{0.69}Fe_{0.31}O_x$/C) in 1.0 M KOH, which exhibited 280 mV overpotential at 10 mA cm^{-2}. It was not only lower than the 335 mV overpotential with amorphous NiO_x/C catalyst, but also lower than the 305 mV

overpotential with commercial Ir/C. The Tafel slope of 30 mV dec^{-1} with the optimized $Ni_{0.69}Fe_{0.31}O_x$/C was comparable to those with the state-of-the-art Ir catalyst and Ni-Fe thin film in alkaline electrolyte. Moreover, an attractive 97% Faradaic efficiency implies that the majority of current density is attributed to the OER, rather than other side reactions. The OER overpotential maintained nearly constant at around 285 mV at 10 mA cm^{-2} during 6 hours anodization. TEM images further show the average Ni-Fe particle size did not apparently change (from 4.4 to 4.6 nm) and no obvious Ni-Fe nanoparticle aggregation was observed. All of these strongly indicate the robust stability of the small amorphous Ni-Fe nanoparticle catalyst for alkaline OER. The reported amorphous Ni-Fe nanoparticles with high OER efficiency and stability can potentially serve as the electrocatalysts to (photo)electrochemical cells for water splitting or CO_2 reduction applications.

4.5 References

1.   Bard, A. J.; Fox, M. A., Artificial Photosynthesis - Solar Splitting of Water to Hydrogen and Oxygen. *Accounts Chem Res* **1995,** *28* (3), 141-145.

2.   Walter, M. G.; Warren, E. L.; McKone, J. R.; Boettcher, S. W.; Mi, Q. X.; Santori, E. A.; Lewis, N. S., Solar Water Splitting Cells. *Chem Rev* **2010,** *110* (11), 6446-6473.

3.   Liang, Y.; Li, Y.; Wang, H.; Dai, H., Strongly Coupled lnorganic/Nanocarbon Hybrid Materials for Advanced Electrocatalysis. *J. Am. Chem. Soc.* **2013,** *135* (6), 2013-2036.

4.   Cook, T. R.; Dogutan, D. K.; Reece, S. Y.; Surendranath, Y.; Teets, T. S.; Nocera, D. G., Solar Energy Supply and Storage for the Legacy and Non legacy Worlds. *Chem Rev* **2010,** *110* (11), 6474-6502.

5.   Lewis, N. S., Toward cost-effective solar energy use. *Science* **2007,** *315* (5813), 798-801.

6.   McCrory, C. C. L.; Jung, S.; Peters, J. C.; Jaramillo, T. F., Benchmarking Heterogeneous Electrocatalysts for the Oxygen Evolution Reaction. *J. Am. Chem. Soc.* **2013,** *135* (45), 16977-16987.

7.	Xin, L.; Zhang, Z. Y.; Qi, J.; Chadderdon, D. J.; Qiu, Y.; Warsko, K. M.; Li, W. Z., Electricity Storage in Biofuels: Selective Electrocatalytic Reduction of Levulinic Acid to Valeric Acid or gamma-Valerolactone. *Chemsuschem* **2013,** *6* (4), 674-686.

8.	Qiu, Y.; Xin, L.; Chadderdon, D. J.; Qi, J.; Liang, C.; Li, W. Z., Integrated electrocatalytic processing of levulinic acid and formic acid to produce biofuel intermediate valeric acid. *Green Chem* **2014,** *16* (3), 1305-1315.

9.	Koper, M. T. M., Thermodynamic theory of multi-electron transfer reactions: Implications for electrocatalysis. *J Electroanal Chem* **2011,** *660* (2), 254-260.

10.	Kanan, M. W.; Nocera, D. G., In situ formation of an oxygen-evolving catalyst in neutral water containing phosphate and Co^{2+}. *Science* **2008,** *321* (5892), 1072-1075.

11.	Dau, H.; Limberg, C.; Reier, T.; Risch, M.; Roggan, S.; Strasser, P., The Mechanism of Water Oxidation: From Electrolysis via Homogeneous to Biological Catalysis. *ChemCatChem* **2010,** *2* (7), 724-761.

12.	Gorlin, Y.; Jaramillo, T. F., Investigation of Surface Oxidation Processes on Manganese Oxide Electrocatalysts Using Electrochemical Methods and Ex Situ X-ray Photoelectron Spectroscopy. *J Electrochem Soc* **2012,** *159* (10), H782-H786.

13.	Man, I. C.; Su, H.-Y.; Calle-Vallejo, F.; Hansen, H. A.; Martínez, J. I.; Inoglu, N. G.; Kitchin, J.; Jaramillo, T. F.; Nørskov, J. K.; Rossmeisl, J., Universality in Oxygen Evolution Electrocatalysis on Oxide Surfaces. *ChemCatChem* **2011,** *3* (7), 1159-1165.

14.	Lee, Y.; Suntivich, J.; May, K. J.; Perry, E. E.; Shao-Horn, Y., Synthesis and Activities of Rutile IrO_2 and RuO_2 Nanoparticles for Oxygen Evolution in Acid and Alkaline Solutions. *J Phys Chem Lett* **2012,** *3* (3), 399-404.

15.	Chou, N. H.; Ross, P. N.; Bell, A. T.; Tilley, T. D., Comparison of Cobalt-based Nanoparticles as Electrocatalysts for Water Oxidation. *Chemsuschem* **2011,** *4* (11), 1566-1569.

16.	Esswein, A. J.; McMurdo, M. J.; Ross, P. N.; Bell, A. T.; Tilley, T. D., Size-Dependent Activity of Co_3O_4 Nanoparticle Anodes for Alkaline Water Electrolysis. *The Journal of Physical Chemistry C* **2009,** *113* (33), 15068-15072.

17.	Pickrahn, K. L.; Park, S. W.; Gorlin, Y.; Lee, H.-B.-R.; Jaramillo, T. F.; Bent, S. F., Active MnOx Electrocatalysts Prepared by Atomic Layer Deposition for Oxygen Evolution and Oxygen Reduction Reactions. *Adv Energy Mater* **2012,** *2* (10), 1269-1277.

18.   Gorlin, Y.; Jaramillo, T. F., A Bifunctional Nonprecious Metal Catalyst for Oxygen Reduction and Water Oxidation. *J. Am. Chem. Soc.* **2010,** *132* (39), 13612-13614.

19.   Liang, Y.; Li, Y.; Wang, H.; Zhou, J.; Wang, J.; Regier, T.; Dai, H., Co_3O_4 nanocrystals on graphene as a synergistic catalyst for oxygen reduction reaction. *Nat Mater* **2011,** *10* (10), 780-786.

20.   Liu, Y.; Higgins, D. C.; Wu, J.; Fowler, M.; Chen, Z., Cubic spinel cobalt oxide/multi-walled carbon nanotube composites as an efficient bifunctionalelectrocatalyst for oxygen reaction. *Electrochem Commun* **2013,** *34* (0), 125-129.

21.   Man, I. C.; Su, H. Y.; Calle-Vallejo, F.; Hansen, H. A.; Martinez, J. I.; Inoglu, N. G.; Kitchin, J.; Jaramillo, T. F.; Nørskov, J. K.; Rossmeisl, J., Universality in Oxygen Evolution Electrocatalysis on Oxide Surfaces. *Chemcatchem* **2011,** *3* (7), 1159-1165.

22.   Li, Y.; Hasin, P.; Wu, Y., $Ni_xCo_{3-x}O_4$ Nanowire Arrays for Electrocatalytic Oxygen Evolution. *Adv Mater* **2010,** *22* (17), 1926-1929.

23.   Bockris, J. O.; Otagawa, T., Mechanism of Oxygen Evolution on Perovskites. *J Phys Chem-Us* **1983,** *87* (15), 2960-2971.

24.   Bockris, J. O.; Otagawa, T., The Electrocatalysis of Oxygen Evolution on Perovskites. *J Electrochem Soc* **1984,** *131* (2), 290-302.

25.   Suntivich, J.; May, K. J.; Gasteiger, H. A.; Goodenough, J. B.; Shao-Horn, Y., A Perovskite Oxide Optimized for Oxygen Evolution Catalysis from Molecular Orbital Principles. *Science* **2011,** *334* (6061), 1383-1385.

26.   Landon, J.; Demeter, E.; Inoglu, N.; Keturakis, C.; Wachs, I. E.; Vasic, R.; Frenkel, A. I.; Kitchin, J. R., Spectroscopic Characterization of Mixed Fe-Ni Oxide Electrocatalysts for the Oxygen Evolution Reaction in Alkaline Electrolytes. *Acs Catal* **2012,** *2* (8), 1793-1801.

27.   Li, X. H.; Walsh, F. C.; Pletcher, D., Nickel based electrocatalysts for oxygen evolution in high current density, alkaline water electrolysers. *Phys Chem Chem Phys* **2011,** *13* (3), 1162-1167.

28.   Potvin, E.; Brossard, L., Electrocatalytic activity of Ni-Fe anodes for alkaline water electrolysis. *Mater Chem Phys* **1992,** *31* (4), 311-318.

29.   Gong, M.; Li, Y.; Wang, H.; Liang, Y.; Wu, J. Z.; Zhou, J.; Wang, J.; Regier, T.; Wei, F.; Dai, H., An Advanced Ni-Fe Layered Double Hydroxide Electrocatalyst for Water Oxidation. *J. Am. Chem. Soc.* **2013,** *135* (23), 8452-8455.

30.   Corrigan, D. A., The Catalysis of the Oxygen Evolution Reaction by Iron Impurities in Thin-Film Nickel-Oxide Electrodes. *J Electrochem Soc* **1987,** *134* (2), 377-384.

31.   Corrigan, D. A.; Bendert, R. M., Effect of Coprecipitated Metal-Ions on the Electrochemistry of Nickel-Hydroxide Thin-Films - Cyclic Voltammetry in 1m Koh. *J Electrochem Soc* **1989,** *136* (3), 723-728.

32.   Grosso, D.; Cagnol, F.; Soler-Illia, G. J. D. A.; Crepaldi, E. L.; Amenitsch, H.; Brunet-Bruneau, A.; Bourgeois, A.; Sanchez, C., Fundamentals of mesostructuring through evaporation-induced self-assembly. *Adv Funct Mater* **2004,** *14* (4), 309-322.

33.   Louie, M. W.; Bell, A. T., An Investigation of Thin-Film Ni-Fe Oxide Catalysts for the Electrochemical Evolution of Oxygen. *J. Am. Chem. Soc.* **2013,** *135* (33), 12329-12337.

34.   Yeo, B. S.; Bell, A. T., Enhanced Activity of Gold-Supported Cobalt Oxide for the Electrochemical Evolution of Oxygen. *J. Am. Chem. Soc.* **2011,** *133* (14), 5587-5593.

35.   Zhang, Z. Y.; Xin, L.; Qi, J.; Chadderdon, D. J.; Li, W. Z., Supported Pt, Pd and Au nanoparticle anode catalysts for anion-exchange membrane fuel cells with glycerol and crude glycerol fuels. *Appl Catal B-Environ* **2013,** *136*, 29-39.

36.   Zhang, Z. Y.; Xin, L.; Sun, K.; Li, W. Z., Pd-Ni electrocatalysts for efficient ethanol oxidation reaction in alkaline electrolyte. *Int J Hydrogen Energ* **2011,** *36* (20), 12686-12697.

37.   Yano, H.; Kataoka, M.; Yamashita, H.; Uchida, H.; Watanabe, M., Oxygen reduction activity of carbon-supported Pt-M (M = V, Ni, Cr, Co, and Fe) alloys prepared by nanocapsule method. *Langmuir* **2007,** *23* (11), 6438-6445.

38.   Paulus, U. A.; Schmidt, T. J.; Gasteiger, H. A.; Behm, R. J., Oxygen reduction on a high-surface area Pt/Vulcan carbon catalyst: a thin-film rotating ring-disk electrode study. *J Electroanal Chem* **2001,** *495* (2), 134-145.

39.   Medway, S.L., Lucas, C.A., Kowal, A., Nichols, R.J., Johnson, D., In situ studies of the oxidation of nickel electrodes in alkaline solution. *Journal of Electroanalytical Chemistry* **2006,** *587* (2), 172-181.

40.   Cheng, W.; Tang, K. B.; Qi, Y. X.; Sheng, J.; Liu, Z. P., One-step synthesis of superparamagnetic monodisperse porous Fe_3O_4 hollow and core-shell spheres. *J Mater Chem* **2010,** *20* (9), 1799-1805.

41.   William D. Chemelewski Heung-Chan Lee, J.-F. L., Allen J. Bard, C. Buddie Mullins, Amorphous FeOOH Oxygen Evolution Reaction Catalyst for Photoelectrochemical Water Splitting. *J. Am. Chem. Soc.* **2014,** *136* (7), 2843-2850.

42.   Smith, R. D. L.; Prevot, M. S.; Fagan, R. D.; Zhang, Z. P.; Sedach, P. A.; Siu, M. K. J.; Trudel, S.; Berlinguette, C. P., Photochemical Route for Accessing Amorphous Metal Oxide Materials for Water Oxidation Catalysis. *Science* **2013,** *340* (6128), 60-63.

43.   Dickinson, M.; Scott, T. B.; Crane, R. A.; Riba, O.; Barnes, R. J.; Hughes, G. M., The effects of vacuum annealing on the structure and surface chemistry of iron:nickel alloy nanoparticles. *J Nanopart Res* **2010,** *12* (6), 2081-2092.

44.   Kostecki, R.; McLarnon, F., Electrochemical and in situ Raman spectroscopic characterization of nickel hydroxide electrodes. *J Electrochem Soc* **1997,** *144* (2), 485-493.

45.   Lyons, M. E. G.; Brandon, M. P., The Oxygen Evolution Reaction on Passive Oxide Covered Transition Metal Electrodes in Aqueous Alkaline Solution. Part 1-Nickel. *Int J Electrochem Sc* **2008,** *3* (12), 1386-1424.

46.   Lyons, M. E. G.; Brandon, M. P., The Oxygen Evolution Reaction on Passive Oxide Covered Transition Metal Electrodes in Alkaline Solution. Part III - Iron. *Int J Electrochem Sc* **2008,** *3* (12), 1463-1503.

47.   Singh, R. N.; Pandey, J. P.; Anitha, K. L., Preparation of Electrodeposited Thin-Films of Nickel Iron-Alloys on Mild-Steel for Alkaline Water Electrolysis .1. Studies on Oxygen Evolution. *Int J Hydrogen Energ* **1993,** *18* (6), 467-473.

48.   Trotochaud, L.; Ranney, J. K.; Williams, K. N.; Boettcher, S. W., Solution-Cast Metal Oxide Thin Film Electrocatalysts for Oxygen Evolution. *J. Am. Chem. Soc.* **2012,** *134* (41), 17253-17261.

49.   A.J.Bard, L.R.Fualkner.; In Electrochemical Methods: Fundamentals and Applications, 2nd Edition.; Wiley: New York, 2001.

50.   Minguzzi, A.; Fan, F. R. F.; Vertova, A.; Rondinini, S.; Bard, A. J., Dynamic potential-pH diagrams application to electrocatalysts for water oxidation. *Chem Sci* **2012,** *3* (1), 217-229.

51.	Guerrini, E.; Chen, H.; Trasatti, S., Oxygen evolution on aged IrO_x/Ti electrodes in alkaline solutions. *J. Solid State Electrochem.* **2007,** *11* (7), 939-945.

52.	Pourbaix, M.; In Atlas of Electrochemical Equilibria in Aqueous Solution.; Pergamon Press: Oxford, 1966.

CHAPTER 5 BCC-PHASED PDCU ALLOY AS HIGHLY ACTIVE ELECTROCATALYSTS FOR HYDROGEN OXIDATION IN ALKALINE ELECTROLYTE[3]

5.1 Introductions

Anion-exchange membrane fuel cells (AEMFCs) have attracted enormous attention in recent years largely because the high pH alkaline environments allow long-time operation of inexpensive non-precious metals and their alloys, which can significantly reduce the cost of fuel cell systems.[1, 2] In particular, for oxygen reduction reaction (ORR) at the cathode, non-noble metal catalysts have shown the comparable activity to that of the state-of-the-art ORR catalyst Pt in alkaline electrolyte, so that a replacement of the expensive noble-metal proton-exchange membrane (PEM) technologies by AEM technologies has attracted great attention.[3-5] However, the activities of the anode reaction, hydrogen oxidation reaction (HOR), are found to be at least two orders of magnitude lower on Pt-group metals in alkaline electrolyte (e.g. exchange current density $i_o \approx 1$ mA.cm^{-2}$_{Pt}$ at 40°C on Pt/C) than those in acidic electrolyte (e.g. $i_o \approx 600$ mA.cm^{-2}$_{Pt}$ at 80°C on Pt), consequently requiring much higher Pt-group metal loading for AEMFCs in comparison with PEMFCs.[6-8] Therefore, motivated by achieving a comparable anode HOR activity in AEMFCs to compete with proton exchange membrane fuel cells (PEMFCs), the mechanism of HOR on transition metals has been extensively studied.

Without considering the pH effect, Trasatti and Nørskov groups proposed an empirical correlation of the exchange current densities of HOR with respect to the hydrogen

---

[3] Unpublished Data (keep confidential). Collaborate with Dr. Le Xin (ISU); Dr. Yawei Li (Penn State University); Prof. Michael Janik (Penn State University); Dr. Qi Liu (Argonne National Laboratory); Dr. Fangmin Guo (Argonne National Laboratory); Dr. Yang Ren (Argonne National Laboratory); Prof. Shuang Gu (Wichita State University).

adsorption energies (derived from the differential standard Gibbs energy of hydrogen adsorption, ΔG_{H*}) on different metals, and a volcano relationship was constructed.[9-11] It has been demonstrated that the active HOR catalyst should bind hydrogen neither too strong nor too weak, thereby enabling all steps to thermo-neutral on such catalyst surface at the equilibrium potential. With a "well-compromised" hydrogen binding strength, Pt-group metals (e.g. Pt, Pd, Ir, Rh etc.) are considered as the highly active catalysts toward HOR. However, to address the distinct HOR catalyst activities in acidic and alkaline environments, it is important to gain deeper insights into the difference in the mechanism. As compared to the HOR in acidic media, the alkali-based HOR is more complicated, following the overall equation of $H_2 + 2OH^- = 2H_2O + 2e^-$ (While in acid, $H_2 = 2H^+ + 2e^-$). To date, there are still controversy over interpreting the inferior HOR performance in alkaline environments despite intense recent research efforts. Yan et al. correlated the experimentally measured HOR exchange current densities of a series of monometals in alkaline electrolyte with their calculated hydrogen binding energy (HBE), and found that most monometallic catalysts possess stronger hydrogen binding in base than that in acid.[12] Therefore, they suggested that the HBE still could be a major descriptor in alkaline electrolyte and that the slower kinetics can be mainly ascribed to a generally strengthened H binding in alkaline environments.[13, 14] On the other hand, Markovic et al. argued that the oxophilic nature of catalyst surfaces (OH binding energy) also played a significant role in alkaline HOR, and evidenced Ir and PtRu catalysts which outperformed Pt toward the H_2 oxidation in alkaline electrolyte.[15] They demonstrated that the oxophilic effect of Ru and Ir on the improvement of HOR activity resulted from both Ir and Ru favored OH adsorption at relatively low potentials, at which the adsorbed H could be oxidatively removed from

the electrode surface. Decoupling of HBE to HOR rate on Pt/Ru-C and Ru-C systems is also validated by electrochemical measurements and kinetic studies, where the researchers provided evidence of surface hydroxyl groups on Ru surface sites participating in a bifunctional mechanism.[16] The major discrepancy between the two categories of viewpoints is how to correlate HBE and OH binding energy with experimental data. Those who support HBE as the major descriptor believe that the underpotential-deposited hydrogen desorption peak potential is directly correlated with HBE and that the CO-stripping is related to the OH binding energy.[13, 14, 17, 18] Nevertheless, so far no DFT work has suggested that the strength of H binding to metals changes with pH change, and to the contrary, the work of Janik group has suggested that changing pH (and the accompanying change to include cations in the near surface region) contributes very little effect on H-metal interactions but instead on OH surface stability.[19] Their calculation is further corroborated by a recent experimental study suggesting that the "hydrogen region" on Pt stepped electrode is actually a "hydrogen-hydroxyl-cation" region and that the observed "hydrogen peak" shift with pH is caused by cation-hydroxyl coadsorption.[20]

Therefore, to develop the highly active HOR catalysts in alkaline media, the modification and optimization of both H and OH adsorption are the key rationale. Guided by the volcano relationship of HOR activity with HBE, Pt-group metal based binary catalysts are investigated, and the second metal has been introduced to reduce the strength of hydrogen adsorption on metal surface. Wong et al. rationally designed the Pt-M (M = Ru, Co, Fe, Cu, and Au) as HOR catalysts, and reported that the hydrogen bind on PtRu, PtFe, PtCo, and PtCu were more or less weakened with the second metal incorporation, whereas the PtAu was expected to demonstrate an increased hydrogen bind strength.[21]. In addition,

Greeley et al. demonstrated the transition metal substrate could significantly vary the hydrogen binding strength of Pd on surface, and Pd/PtRu shows an optimal hydrogen adsorption ability thereby exhibiting at an order of magnitude higher HOR exchange current density than other investigated Pd/M catalysts (M=Re, Ru, Ir, Rh, PtRu, Pt, Au).[22]

However, little research effort has been made to explore the crystalline structure of metal and metal alloy catalysts on their HOR activity in alkaline electrolyte. From the structural perspective, the crystalline structure with different lattice constant can significantly influence their corresponding hydrogen or hydroxyl anion adsorption strengths, thus altering their overall activity for a specific reaction (e.g. enhanced activity of ORR and ethanol oxidation reaction on bcc structured PdCuCo and PdCuNi materials).[23,]

Herein, we prepared $Pd_{50}Cu_{50}$ alloy nanoparticles (NPs) and characterized the HOR activity in 0.1 M KOH solution. The HOR activity exhibited a strong dependence on the annealing temperature. In particular, PdCu alloy NPs annealed at 500°C exhibits very high mass specific activities, outperforming all as-synthesized Pd, PdCu, and even commercial Pt catalysts. The PdCu crystalline structure transformation from face-centered cubic (fcc) to body-centered cubic (bcc) was observed as the thermal annealing temperature increasing from 200°C to 600°C, and the correlation of PdCu alloy crystalline structure with their HOR reaction performances and mechanisms (the strength of H and OH adsorption) was further investigated by DFT computations. It is demonstrated that compared to PdCu fcc model surfaces, H adsorption potential and OH adsorption potential on PdCu bcc model surface are closer to those on Pt model surface. Specifically, the much stronger OH adsorption on PdCu bcc surface renders the bcc phase to exhibit much better HOR catalytic performance than fcc phase, as demonstrated by our two factor volcano plot. Therefore, by

taken both H and OH adsorption into consideration, the bcc structured PdCu alloy under 500°C thermal annealing exhibits a remarkable HOR activity in alkaline electrolyte. These analyses of experimental results along with the theoretical modeling based on DFT, provide a solid evidence for contribution of enhanced HOR activity in alkaline media to the bcc structure of PdCu alloy, and shed lights into the property-activity relationship of bimetallic alloy crystalline structure and rational design of efficient electrocatalysts for the specific reaction.

5.2 Experimental

5.2.1 Materials.

Pd(acac)$_2$ (99%, Sigma Aldrich), Cu(acac)$_2$ ($\geq$99.9%, Sigma Aldrich), Oleylamine (70%, Sigma Aldrich), Oleic acid ($\geq$99%, Sigma Aldrich), benzyl ether (98%, Sigma Aldrich), LiBEt$_3$H (1.0 M lithium triethylborohydride in THF), 5 wt% Nafion solution (in iso-propanol, Ion Power), and KOH ($\geq$85%, Sigma Aldrich) were purchased and used without further purification for all experiments. Vulcan XC-72R carbon black (Fuel Cell store) as catalysts supporting materials were pre-treated at 120°C in Air and stored in vacuum oven at 80°C. UHP N2 (99.999%, Airgas), UHP H$_2$ (99.999%, Airgas), and UHP CO (99.99% were used for electrochemical property characterizations.

5.2.2 Synthesis of PdCu/C-raw, Pd/C catalysts

The PdCu/C (Pd:Cu atomic ratio = 1:1) samples were prepared through one-step wet-chemical method via a fast reduction of Pd^{2+} and Cu^{2+} in an organic solvent, which has been reported previously. (Yang, 2014, Langmuir). Typically, 68.0 mg of Vulcan XC-72R carbon black was dispersed in 40 ml of benzyl ether at room temperature, followed by ultra-sonication for 30min to obtain uniform mixture. The 0.1 mmol of Pd(acac)$_2$ and 0.1

mmol of Cu(acac)$_2$ were then dissolved into mixture with stirring. After 30 min UHP N$_2$ purging, the mixture was heated to 100°C, followed by adding 400 μL of oleylamine and 200 μL of oleic acid adding and holding for 10min to get uniform solution. As the temperature was increased to 150°C, 1.0 mL of LiBEt$_3$H solution was quickly injected into the system. The temperature was held for 10 min, and then quickly increased to 210°C. After holding for an additional 45 min, the final products were collected by filtration, washed with copious ethanol, and dried in vacuum oven at 60°C overnight. A control sample of, Pd/C, was synthesized via a similar method discussed above, except Cu(acac)$_2$ metal salt introduction.

5.2.3 Synthesis of PdCu/C-T (200°C to 600°C)

A 30 mg PdCu/C-raw sample was subjected to thermal annealing with different temperature from 200°C to 600°C with 10 °C/min heating rate under 100 ml/min UHP N2 purging condition for 4h. The obtained PdCu/C-T (T=200°C to 600°C) materials were finally stored in 20 ml-type glass vial.

5.2.4 Physical characterization

The Inductively coupled plasma-optical emission spectroscopy (ICP-OES, Perkin Elmer Optima 8000 instrument) was utilized to determine the Pd/Cu weight and atomic ratio of as-synthesized PdCu/C catalysts. 10 to 15 mg PdCu/C powders were dispersed into concentrated aqua regia with stirring for Pd and Cu dissolving, followed by the dilution with DI H$_2$O and filtering to obtain PdCu dissolved 4% aqua regia sample solution. Thermogravimetric (TGA, Discovery serie) and simultaneous modules were employed to measure the mass loss of PdCu/C catalysts in UHP N$_2$ has with heating rate of 5°C/min from 30°C to 620°C.

The ex-situ XRD patterns were obtained from a Rigaku Ultima IV X-ray diffraction (XRD) systems (1D acquisition mode) with Cu Kα radiation (λ = 1.5406 Å) at room temperature, with a tube current of 30 mA and a tube voltage of 40 kV. The in-situ XRD patterns were achieved at Argonne National lab 11-ID-C beam line with high energy radiation (λ = 0.774902 Å). The sample was heated from 200°C to 900°C with 2°C/min rate, and held 15s per 2°C for sample scanning.

JEOL 2100 200 kV scanning and transmission electron microscope (STEM) was utilized to determine the PdCu NPs dispersion, particle size, and size distribution of as-synthesized PdCu/C catlaysts. High-angle annular dark-field STEM (HAADF-STEM) imaging, element mapping, and line scanning was performed on Titan Themis 300 probe corrected TEM with a Super-X EDX detector from Sensitive Instrument Facility of Ames lab. To avoid the sample grid interference, the TEM sample of PdCu/C catalysts were prepared by using Au TEM grid. X-ray photoelectron spectroscopy (XPS) with Mg K alpha X-ray (1253.6 eV) (Kratos Amicus/ESCA 3400) was used to determine the Pd/Cu concentrations and their corresponding chemical/valence status through different binding energy peaks.

5.2.5 Electrode preparation

All electrocatalytic property characterizations were conducted in a three-electrode system using electrochemical potentiostat (VSP-300, Bio-Logic). A coiled Pt-wire, which is isolated by a fritted glass tube from the main test electrolyte, and a 0.1 M KOH filled Hg/HgO electrode were utilized as counter and reference electrode in the three-electrode system, respectively. To fabricate the working electrode, a 1.0 mg/ml of catalyst ink was prepared by adding PdCu/C powders in iso-propanol (IPA), followed by 30 min of ultra-sonication so as to fully disperse particles in the solvent. 20 µl of catalyst ink was drop-

casted onto the glassy carbon electrode surface with a Pd loading of 12.5 $\mu g_{Pd}/cm^2_{geo}$, and 10 μl of IPA diluted 0.05 wt% Nafion solution was finally dropped on the surface of PdCu/C. After 30 min air drying at ambient temperature, a uniform catalyst thin-film was obtained for following electrochemical measurements. The Pt/C and Cu/C RDE electrode were also fabricated with a Pt or Cu loading of 12.5 $\mu g_{active\ metal}/cm^2_{geo}$.

5.2.6 HOR activity measurement

Prior to electrocatalytic property testing, the Hg/HgO reference electrode was calibrated in standard three electrode system with Pt wire as working and counter electrode, and Hg/HgO electrode as the reference electrode. The 0.1 M KOH solution was purged with UHP H2 for 30 min to obtain H_2-saturated electrolyte, and the linear sweep voltammetry (LSV) test was conducted at a scan rate of 0.5 mV/s from -0.95 V to -0.85 V vs. Hg/HgO, where the current crossed zero is taken to be the thermodynamic potential for the hydrogen electrode reactions. All reported potential in this paper was versus the reversible hydrogen electrode (RHE), which was converted by using equation of $E_{(RHE)} = E_{(Hg/HgO)} + 0.918\ V$ in 0.1 M KOH electrolyte. All applied potentials in this paper were reported versus the reversible hydrogen electrode (RHE).

The electrochemical impedance spectroscopy (EIS) measurements were performed by applying an AC voltage with 5 mV amplitude in a frequency range from 300 KHz to 100 mHz and recorded at open circuit voltage (OCV) to compensate and correct the practical potential applied on the working electrode by using following equation:

$$E_{iR-free} = E_{applied} - iR$$

where $E_{applied}$ is the applied potential on working electrode, i is corresponding measured current, R is internal resistance determined by EIS, and $E_{iR\text{-}free}$ is the internal-resistance free potential. The internal resistance of three-electrode system was measured to be ~40 Ohm in 0.1 M KOH solution.

All HOR activity measurements were carried out at room temperature. The 0.1 KOH alkaline electrolyte was purged with UHP H_2 gas at least 30 min prior to test to obtain H_2-saturated 0.1 M KOH solution. Cyclic voltammertry (CV) test was performed at 50 mV/s scan rate, while the HOR activity was evaluated by using linear sweep voltammetry (LSV) in H_2-saturated electrolyte with a 1 mV/s scan rate at 1600 rpm rotation. It is important to noted that H_2 could be absorbed into Pd lattice, thereby showing an extra HOR peak in its corresponding polarization curve. Thus, we have to use low scan rate to reveal the intrinsic activity of Pd-based catalysts toward HOR.

With iR-correction, the kinetic current of the HER/HOR, i_k, was calculated based on the Koutecky-Levich equation.

$$\frac{1}{i} = \frac{1}{i_k} + \frac{1}{i_d}$$

Where i is the measured current, and i_d is the limiting current. The i_k was then normalized by the geometric surface area of RDE disk ($0.19625 cm^2$) to obtain kinetic current density, J_k.

The mass activity (MA) was normalized by using the mass of active metal drop-casted on RDE surface. For alloyed PdCu/C catalysts, only Pd was considered as active metal, whereas Cu is inert toward HOR.

$$MA = i_k / M_{active\ metal}$$

where $M_{active\ metal}$ is the mass of active metal

The specific activity (SA) was normalized by using the ECSA of active metal drop-casted on RDE surface. For alloyed PdCu/C catalysts, only Pd was considered as active metal, whereas Cu is inert toward HOR.

$$SA = i_k / ECSA_{active\ metal}$$

where $ECSA_{active\ metal}$ is the electrochemical surface area of active metal

The exchange current (i_o), and mass and specific current densities ($i_{o,m}$ and $i_{o,s}$) of Pd/C, Pt/C, PdCu/C-200°C and PdCu/C-500°C were calculated by using following equations.

$$\frac{1}{i} = \frac{1}{i_k} + \frac{1}{i_d}$$

$$i_k = i_o \frac{F\eta}{RT}$$

The kinetic currents can be fitted into the linearized Butler-Volmer equation with the assumption that the summation of acnoidc and cathodic transfer coefficient equals to 1 ($\alpha_a + \alpha_c = 1$), and the results are shown in Table S4.

5.2.7 Electrochemical surface area (ECSA) measurement

The electrochemical surface area (ECSA) of Pd in PdCu/C was determined by using CO-stripping voltammograms. The PdCu/C electrode was first stabilized through cyclic voltammetry (CV) scanning at a scan rate of 100 mV/s for at least 50 cycles under UHP N_2 purging. Afterwards, UHP CO was purged for 20 min to obtained CO-saturated solution.

The electrode was subsequently held at 0.2V vs. RHE for 15 min in CO-saturated solution, followed by another 15 min with UHP N_2 purging. The CV was then conducted between 0.2V to 1.25 V vs. RHE with a 20mV/s scan rate.

5.2.8 Durability test of PdCu/C-500°C

The durability, another important criteria used to evaluate the catalysts, was also studied, which is rarely reported in previous HOR publications. In this work, the PdCu/C-500°C were spray-coated on the acid-treated carbon cloth to simulate the practical HOR electrode in HEMFCs, and the Pt/C electrode as control group was also investigated by using the same active metal loading to PdCu/C electrode. As shown in **Figure S3**, the measured current of PdCu/C-500°C catalyst was slight decreased, and retained about 88.0% performance compared to the initial current after 12h. However, the Pt/C electrode shows a rapid activity drop, and only remained 70.5% of initial performance after 12h. The activity degradation of the nano-scaled catalysts in long-term durability test could be attributed to three possible reasons: 1) metal leaching out; 2) particle agglomeration; and 3) crystalline structure change. To rule out the possible reason of particle agglomeration and structure change, we compare the XRD and TEM results before and after 12h durability test. As shown in **Figure S6**, the XRD pattern of PdCu/C electrode has no change after 12h test, where the bcc diffraction peaks were well maintained, suggesting a good stability of bcc structure of PdCu NPs under applied potential in the absence of phase transformation. The sharp peaks centered at 44.2°, 64.5°, and 81.9° should be assigned to AS-4 polymer reflections, which can be observed from XRD patterns of blank AS-4 sprayed electrode. The TEM images (**Figure S3b**) show the similar particle size before and after 12h chronoamperometry tests, indicating rare particle agglomeration. Therefore, the

performance drop could ascribe to leach-out of the Pd-Cu metal ions as evidenced by ICP-OES results that small amount of Pd and Cu were detected in the electrolyte after durability test.

5.2.9 Reference intensity ratio (RIR) method of quantitative analysis

The RIR method was used to estimate the fcc and bcc phase ratio in PdCu NPs from ex-situ XRD patterns. Since we only have two difference crystalline structure (defined as α and β), the RIR equation can be simplified as following:

$$X_\alpha = \frac{I_\alpha}{I_\alpha + I_\beta / K_\alpha^\beta} \text{ and } X_\beta = \frac{I_\beta}{I_\beta + I_\alpha / K_\alpha^\beta}$$

$$K_\alpha^\beta = \frac{K_{Al2O3}^\beta}{K_{Al2O3}^\alpha} = \frac{(I/I_c)_\beta}{(I/I_c)_\alpha}$$

$$(I/I_c)_{fcc} = 12.62; \ (I/I_c)_{bcc} = 16.94$$

where X_i is the weight fraction of phase i (fcc or bcc phase); I_i is the intensity of reflection of specific facet which is defined as I=100%; K is calculated by using above equation. I/Ic is the defined as the reference intensity ratio (RIR) for a 50:50 mixture of phase α and corundum (Al_2O_3), which is so called "RIR" value. In this work, we choose the fcc-PdCu (Fm-3m(225)) ICCD 04-015-2465 and bcc-PdCu (Pm-3m(221)) ICCD 04-015-2413 standard XRD card for RIR quantitative analysis, and fcc(111) as well as bcc(110) diffraction peaks were defined as I=100% line for fcc and bcc phase, respectively. The fcc/bcc phase ratio was estimated as shown in **Figure S5**.

5.2.10 Density functional theory (DFT) calculation

Density functional theory (DFT) calculations were used to investigate the adsorption and reaction energetics of *H, *OH and *H_2O on Pt, Pd and PdCu surfaces. These calculations were performed using the projected augmented wave (PAW) method as implemented in the Vienna *Ab* initio simulation package (VASP) 5.4.4. The electron interactions were described using the Perdew–Burke–Ernzerhof (PBE) exchange-correlation functional within the generalized gradient approximation (GGA) scheme. The kinetic cutoff energy for the plane-wave basis set was 700 eV. For geometric optimizations, the smearing method of Methfessel-Paxton (MP) and smearing widths of 0.2 eV were applied to all of the abovementioned metallic systems.

To construct the surface slabs required to model *H, *OH and H_2O adsorption, we first optimize the lattice constants of the corresponding bulk phases. For fcc-Pt unit cell with 4 Pt atoms, our test indicated that a $24 \times 24 \times 24$ Monkhorst–Pack k-point mesh led to an energy difference less than 0.001 eV/atom. The $24 \times 24 \times 24$ Monkhorst–Pack k-point mesh was also applied to fcc-Pd and bcc-PdCu (B2) unit cells. For fcc-PdCu bulk phase, previous studies proposed two kinds of ordered structures, namely, $L1_0$ and B13. Due to their different unit cell size, we applied $13 \times 13 \times 13$ and $6 \times 6 \times 6$ Monkhorst–Pack k-point mesh to achieve a similar computational accuracy. All bulk phases were optimized until the magnitude of the residual forces on the atoms was less than 0.001 eV Å^{-1}.

For *H adsorption, to investigate the coverage effect on the adsorption energy, 1×1, 2×1 and 3×1 rectangular unit cells was used for PdCu-B2(110), PdCu-$L1_0$(111) and PdCu-B13(111). The *H coverage was thus 1/2 ML, 1/4 ML and 1/6 ML, respectively. The same coverage was achieved on Pt(111) and Pd(111) using 1×2, 2×2 and 3×2 rectangular unit cells. $24 \times 18 \times 1$, $12 \times 18 \times 1$ and $8 \times 18 \times 1$ Monkhorst–Pack k-point meshes were

used to sample the corresponding reciprocal spaces. For *OH and *H_2O adsorption, a 3×1 rectangular unit cell for PdCu-B2(110), PdCu-L1$_0$(111) and PdCu-B13(111) and a 3×2 rectangular unit cell for Pt(111) and Pd(111) were found to be the smallest periodic unit that can repeat the hexagonal ice like water structure. 1/3 ML *OH and 1/3 ML *H_2O arrangement was achieved for *OH adsorption. All surface calculations used 4-layer slabs with the bottom two layers fixed to their bulk position, and the vacuum spaces between periodic images were set no less than 14 Å. The Pd enrichment in PdCu alloys observed by experiment was modelled by constructing a full Pd outermost layer. The structural optimization was regarded as complete when the magnitude of the forces on the atoms was less than 0.01 eV Å^{-1}. Dipole corrections were included in all surface calculations in the surface normal direction for both energies and forces. The frequencies of the surface adsorbed species were computed using finite difference method, and zero-point energy as well as vibrational entropy was computed with standard methods and harmonic oscillator approximation to covert electronic DFT energy into free energy. The entropy term of free molecular species was referred to JANAF thermodynamic table. All DFT calculations were spin-unpolarized. Coordinates of the optimized structures are available in the supporting information.

5.3 Results & Discussions

5.3.1 Catalysts Synthesis and Physical Characterizations

The PdCu NPs were synthesized followed a one-step wet-chemical method via a fast reduction of Pd^{2+} and Cu^{2+} precursors.[24] In order to mitigate the particle agglomeration, carbon support (carbon black) was introduced in the beginning of synthesis process, and as-prepared PdCu NPs can be deposited on carbon black yielding the PdCu/C-raw. As

shown in **Figure 5.1a**, PdCu NPs were found to be evenly dispersed on the surface of carbon black, and the particle size was well controlled at ca. 4.7 nm with a narrow size distribution (3.5-6.5 nm). Due to such a small particle size, only two representative diffraction peaks at 41.7° and 48.4 were distinguished from PdCu/C-raw XRD pattern, which can be indexed to (111) and (200) reflections of face-centered cubic (fcc) PdCu (ICCD 04-015-2414) (**Figure 5.1b**). A lack of monometallic Pd and Cu diffraction peaks indicates the well alloyed fcc-typed PdCu NPs in the absence of Pd-Cu phase segregation.
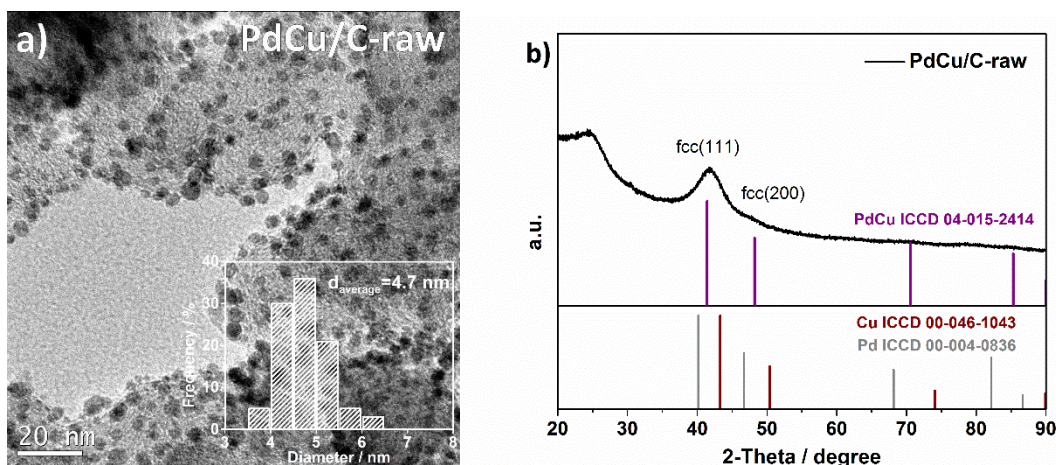
Figure 5.1 a) TEM image and **b)** XRD patterns of PdCu/C-raw.

5.3.2 Electrochemical Characterizations

The HOR activity of as-synthesized PdCu/C-raw, Pd/C, Cu/C, and commercial Pt/C, was evaluated by using rotating disk electrode (RDE) voltammetry in H_2-saturated 0.1 M KOH electrolyte. HOR/HER polarization curves were compensated by the electrolyte resistance measured before testing, and the kinetic current density, J_k, was calculated based on the Koutecky-Levich equation (**see supporting information**).[25] Although the kinetics of HOR in acid electrolyte was too fast to be determined by using RDE, the catalysts could not reach the Nernstain diffusion limited overpotential in the alkaline electrolyte, and therefore the RDE measurement enables to well describe the kinetics of HOR in base.[26] As shown

in **Figure 5.2a and 5.2b**, the Pd/C exhibits a moderate HOR activity among all investigated monometallic catalysts, which follows the order of Pt/C > Pd/C > Cu/C (nearly inactive toward HOR). The half wave potential of Pd/C was measured to be 0.069 V at 1600 rpm, and this is very close to the result of 0.070 V reported by Yan et al. [25] According to the assumption that incorporated Cu could optimize HBE and OH adsorption energy over Pd, the PdCu/C-raw was expected to show a higher HOR activity than that of Pd/C in alkaline solution. Unexpectedly, a fairly inferior HOR activity with a much larger half wave potential of 0.204V was obtained over PdCu/C-raw. We further applied thermal annealing to obtain PdCu/C-T samples (T=200°C, 300°C, 400°C, 500°C, and 600°C). Surprisingly, the HOR activity of thermal-treated PdCu/C samples were found to be much improved, and proportional to their thermal annealing temperature. PdCu/C-500°C exhibits the highest HOR activity with a much smaller half wave potential of 0.028 V as compared to 0.069 V of Pd/C and 0.047 V of Pt/C. With further increased annealing temperature, the HOR activity of PdCu/C-600°C ($E_{1/2}$=0.184 V) was largely reduced, which is very similar to those of PdCu/C-raw ($E_{1/2}$=0.204 V) and PdCu/C-200°C ($E_{1/2}$=0.145 V).

To obtain the surface-specified activity, we measured the electrochemical surface area (ECSA). Integration of PdO reduction peak was the most commonly used method to determining the ECSA of Pd-based catalysts.[27, 28] However, Cu^{1+} reduction peak was found to overlap the PdO reduction peak in the potential range of 0.420 V to 0.720 V (**Figure S1**), thus causing an overestimation for ECSA of as-synthesized PdCu/C catalysts.[29] Therefore, CO-stripping method was employed to measure the ECSA of active Pd (or Pt) for all investigated catalysts in this work, and all measured ECSA results were summarized

in **Table S1** (**CO-stripping measurement, see supporting information**).[28, 30] The specific

activity (SA) was then normalized by measured ECSA of active Pd (or Pt).
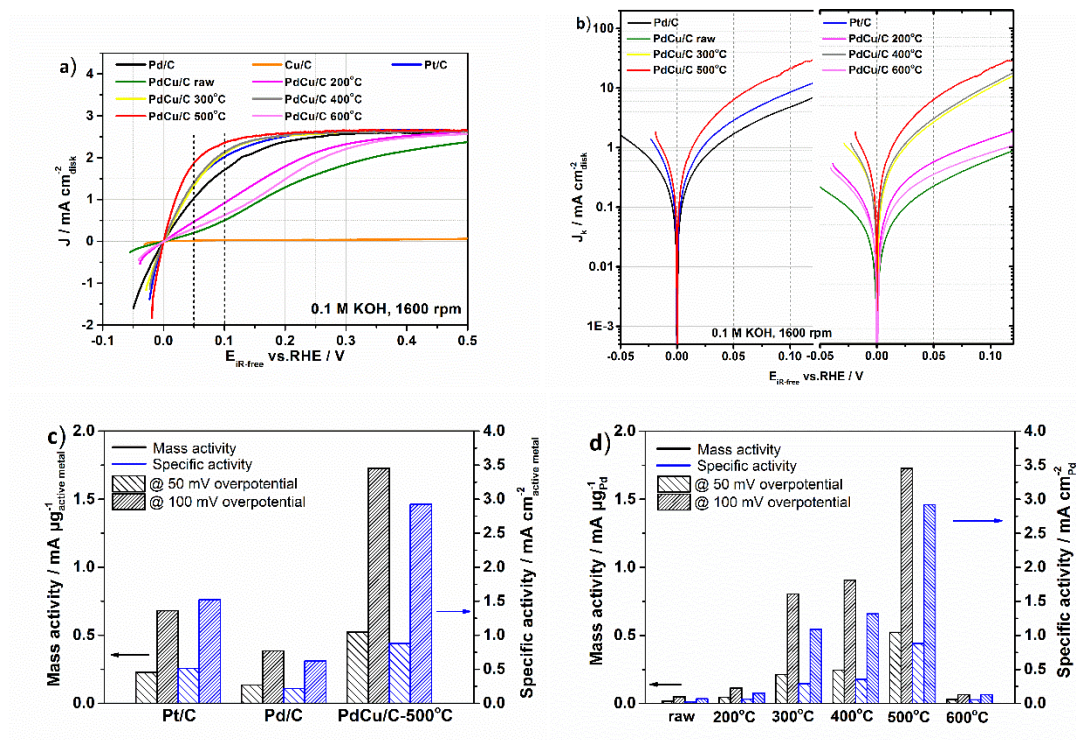
Figure 5.2 a) HOR/HER polarization curves **b)** measured kinetics current density on Pt/C, Pd/C, Cu/C and PdCu/C materials in H_2-saturated 0.1M KOH at 1 mV/s scan rate with 1600rpm rotating speed; **c)** and **d)** Comparison of HOR activity on Pt/C, Pd/C, and PdCu/C materials (SA was normalized by using ECSA of active metal obtained from CO-stripping test)

As shown in **Figure 5.2c and 5.2d**, the mass activity (MA) and the specific activity (SA)

were determined at 50 mV and 100 mV overpotential, respectively (**Details of MA and**

SA calculation, see Supporting information). Among all studied catalysts, PdCu/C-

500°C exhibits the highest MA of 0.522 mA $\mathrm{ug_{Pd}^{-1}}$ and SA of 0.883 mA $\mathrm{cm_{Pd}^{-2}}$ at 50mV

overpotential, which is about 2 times higher than those of Pt/C (MA of 0.229 mA $\mathrm{ug_{Pt}^{-1}}$,

SA of 0.514 mA $\mathrm{cm_{Pt}^{-2}}$) and 4 times higher than those of Pd/C (MA of 0.135 mA $\mathrm{ug_{Pd}^{-1}}$,

SA of 0.219 mA $\mathrm{cm_{Pd}^{-2}}$), respectively. Similar behavior was observed at 100mV

overpotential where the PdCu/C-500°C becomes more active for HOR. These results were

also compared with other HOR catalysts reported in previous work (**Table S2**), and it is

obvious that the activity of the as-synthesized PdCu/C-500°C stays on the top among reported noble metal based HOR catalysts. On the other hand, a robust stability of as-synthesized PdCu/C-500°C was also obtained by chronoamperometry test of 100 mV overptental for 12h in 0.1M KOH solution (**Figure S2**). By taking the low catalyst cost into consideration, as-synthesized PdCu/C-500°C catalysts would be quite promising to serve as the HOR catalysts in AEMFCs.

5.3.3 Structure analysis for elucidating enhanced HOR activity

To understand the reason of the improved HOR activity on PdCu/C-500°C after thermal annealing, the PdCu NPs composition as well as crystal structure were further analyzed. It is important to note that most organic complexes (surfactants) involved in the synthesis process were removed after heat treatment, and <3% surfactants were detected from all thermal annealed PdCu/C samples by TGA. As shown in **Figure S3**, two weight loss steps were observed, including the evaporation and desorption of absorbed water on catalyst surface at 70°C to 170°C and surfactant desorption and gradual decomposition at 170°C to 600°C.[31] With applying thermal annealing, PdCu/C-T (T=200°C to 600°C) catalysts exhibit very similar weight loss rate between 170°C to 600°C which is much slower than that of PdCu/C-raw sample. Therefore, the thermal annealing process is effective to remove the organic surfactants and water residue existed in PdCu catalysts, and it is clear that the low HOR activity of PdCu-raw and PdCu/C-200°C cannot be attributed to surfactant residue.
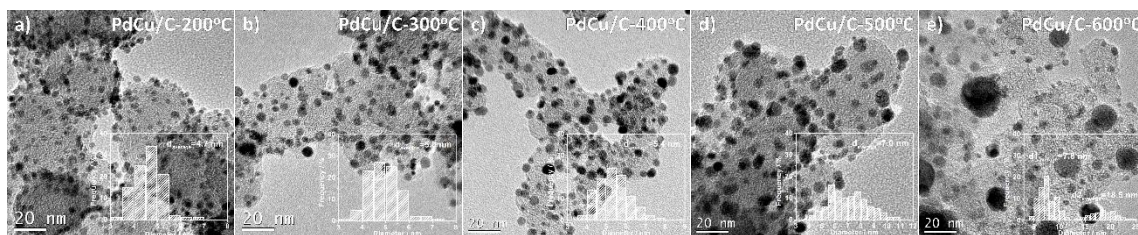
Figure 5.3 TEM images, particle diameter histograms and XRD patterns of PdCu/C-T (T=200°C to 600°C) catalysts
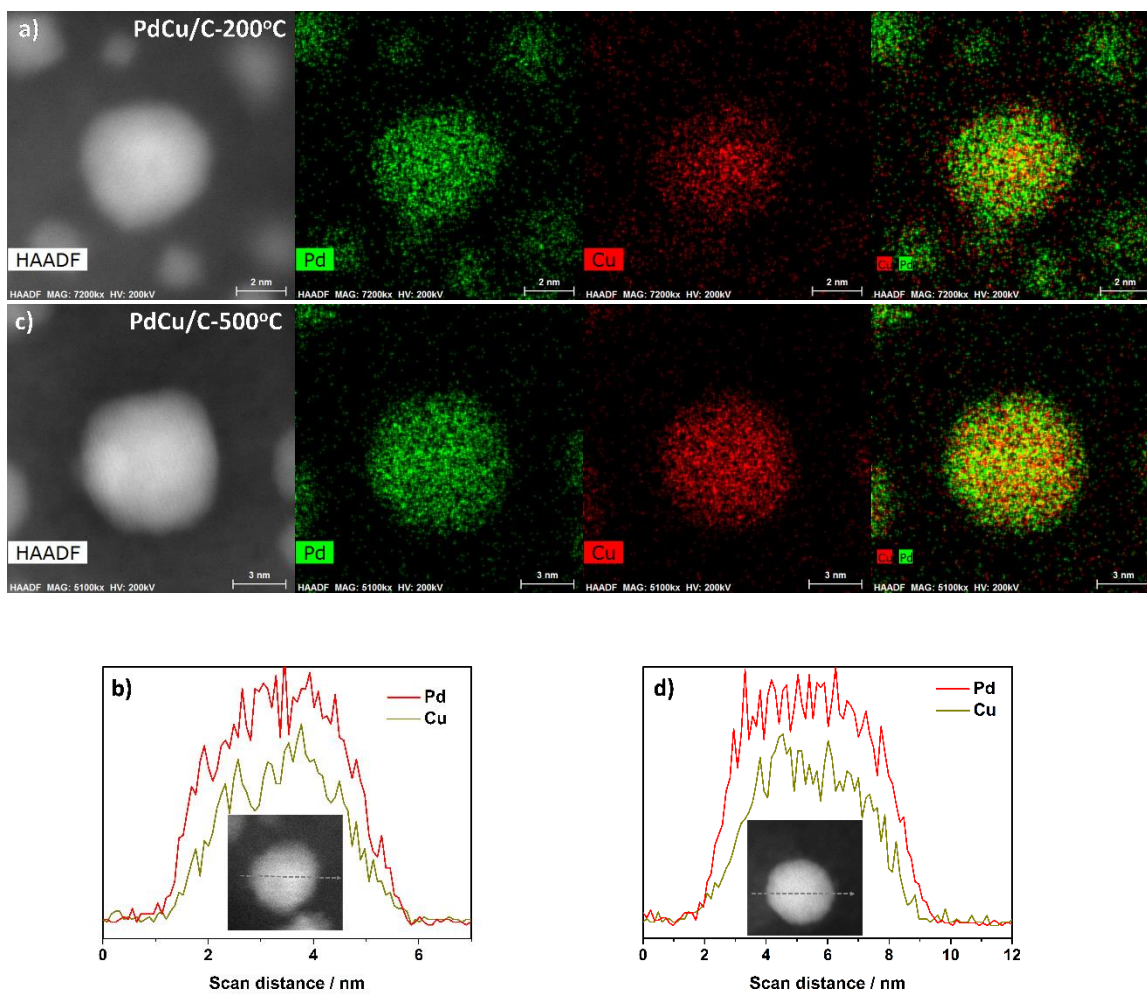
Figure 5.4 High-angle annular dark field scanning TEM (HAADF-STEM) images, element mapping, and corresponding line scanning images of **a-b)** PdCu/C-200°C, and **c-d)** PdCu/C-500°C

The transmission electron microscopy (TEM) images reveal a good dispersion of PdCu NPs on carbon support over all PdCu/C-T (T=200°C to 600°C) catalysts. Thanks to the

carbon support, very slight particle agglomeration was observed, and the PdCu particles

grew from 4.7nm (PdCu-200°C) to 7.0nm (PdCu-500°C) as shown in **Figure 5.3a-d**. When

the temperature was further increased to 600°C, seriously agglomerated PdCu particles

with ~18.5nm diameter were observed (**Figure 5.3e**). **Figure 5.4** shows the high-angle-

annular-dark-field STEM (HAADF-TEM) images and corresponding energy-dispersive X-

ray spectroscopy (EDS) element mapping and line scan images of representative PdCu NPs

treated by 200°C and 500°C. It is obvious that Pd and Cu species were uniformly

distributed throughout PdCu NPs, indicating a well alloyed PdCu NPs in the absence of

core-shell structure. A Pd-rich surface was observed on both PdCu/C-200°C and PdCu/C-

500°C samples from EDS element mapping and line scan images, which could be caused

by higher content of Pd in PdCu NPs. As confirmed by inductively coupled plasma optical

emission spectrometer (ICP-OES), the PdCu composition varies slightly from 56.5%/43.5%

(Pd/Cu) of PdCu/C-200°C to 55.8%/44.2% (Pd/Cu) of PdCu/C-600°C (**Table S3**). Less

than 1% Pd/Cu composition change observed on thermal annealed PdCu/C catalysts,

thereby making very little contribution to HOR activity enhancement of PdCu/C 500°C via

thermal annealing. The composition of well alloyed PdCu NPs was further studied by XPS.

As compared to Pd/C, Pd $3d_{5/2}$ and Pd $3d_{3/2}$ peaks of all PdCu/C samples shift to lower

binding energy of 335.3eV (Pd $3d_{5/2}$) and 340.6eV (Pd $3d_{3/2}$) (**Figure S4**), which can be

ascribed to smaller electron negativity of Cu than that of Pd.[32] However, no apparent

binding energy shift of Pd $3d_{5/2}$ and Pd $3d_{3/2}$ peaks was observed among all PdCu/C

catalysts as evidenced by XPS Pd narrow scan results of PdCu/C-raw and PdCu/C-T

(200°C to 600°C). These observations further indicate that thermal annealing has very little

effect on PdCu composition change and Pd and Cu chemical state changes, further, well

alloyed PdCu NPs can be maintained during thermal annealing in the absence of Pd-Cu phase segregation or core-shell structure formation. Therefore, the promoted HOR activity of PdCu/C-300°C, PdCu/C-400°C and PdCu/C-500°C cannot simply be attributed to their composition variation after heat treatment.
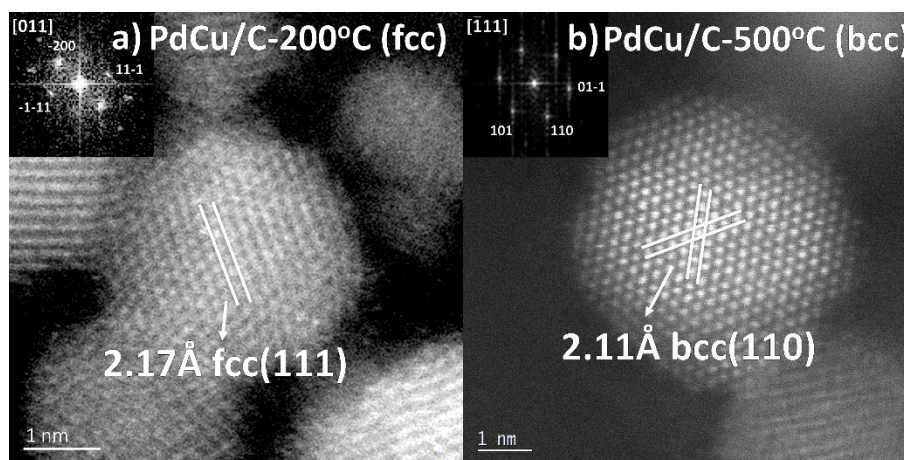
Figure 5.5 HAADF-STEM and corresponding FFT of **a)** PdCu/C-200°C and **b)** PdCu/C-500°C

The PdCu/C-200°C and PdCu/C-500°C were further characterized by HAADF-TEM along the [011] and [$\bar{1}$11] zone axis, respectively. As shown in **Figure 5.5a**, the average spacing of periodic lattice fringes were measured to be 2.17Å, which can be assigned to the (111) facet of face-centered cubic (fcc) structured PdCu NPs. In contrast, a body-centered cubic (bcc) structure was detected from PdCu/C-500°C sample, where a clearly super periodic bcc (110) facet with 2.11Å lattice spacing can be distinguished. From PdCu/C-200°C to PdCu/C-500°C, the different crystalline structure suggests an fcc/bcc phase transformation under different temperature thermal annealing. Therefore, X-ray diffraction characterization was used to study the crystalline structure of thermal annealed PdCu/C-T (T=200°C to 600°C) catalysts. From X-ray diffraction (XRD) patterns of pristine PdCu/C-raw (**Figure 5.6**), a broad peak at 41.7° was observed. As the heat treatment temperature increasing, this broad peak gradually shifted to higher angle, and a shoulder peak evolved

at 41.4°. In the end, the broad peak drastically split to two sharp peaks at 41.4° and 42.9° under 600°C thermal annealing, which can be assigned to fcc(111) (ICCC-000-048-1551) and CsCl-structure typed bcc(110) facet of PdCu (ICCC-04-015-2413). Moreover, the reflections of PdCu fcc(200), (220), and (311) facets were observed at 48.2°, 70.5°, and 85.3°, while the bcc (100), (200), and (211) facets were shown at 29.9°, 62.2°, and 78.5°, respectively. It turns out that the bcc structure of PdCu was formed via thermal annealing, which is indicated by the broad peak positive shift and the growth of corresponding bcc reflections at high angle region. Despite distinct fcc (111) and bcc (110) peak separation of PdCu/C-600°C, the integrated intensity of PdCu fcc (111) and bcc (110) peaks were overlapped over all investigated PdCu/C catalysts, and the temperature of phase transformation from fcc to bcc remains unclear. Therefore, an in-situ high energy XRD (HE-XRD) (0.774902 Å wavelength) were carried out with the protocol of ramped annealing from 200°C to 900°C at 2°C min^{-1} heating rate under UHP N_2 gas flow, as shown in **Figure 5.7**. A representative HE-XRD pattern collected at 600°C, where the peaks centered at 20.5°, 21.3°, and 23.8°, were clearly identified, which can be typically assigned to fcc(111), bcc(110), and fcc(200) facets, respectively. The short dash line in color map of in-situ XRD patterns reveals a peak shift of fcc(111) reflection to higher angle from 280°C, indicating a bcc phase formation in PdCu NPs. As further heating to 450°C, a slight peak shrink was observed, followed by the peak splitting at 500°C. Furthermore, the diffraction peak of bcc(110) facet gradually disappears, whereas the fcc(111) as well as fcc(200) reflections becomes stronger with temperature increasing to 900°C. Aligned with these observations, it is confirmed that partial fcc structured PdCu NPs was transformed to bcc-typed PdCu NPs at 280°C, and both fcc and bcc structured PdCu NPs coexist over a

broad temperature range up to 900°C, followed by a complete bcc structure transformation back to fcc structure. According to this phase transformation pathway, the PdCu/C-200°C could contain only fcc structured PdCu NPs, while both bcc and fcc structure can be maintained for as-synthesized PdCu/C-T (T=300°C to 600°C) samples in this work. In addition, the peak shrinking at 450°C implies the particle size increasing due to particle agglomeration, which is in good agreement with the TEM characterization results of PdCu/C-500°C and PdCu/C-600°C.

The broad peak centered at 20.7° was further deconvoluted into fcc(111) and bcc(110) peaks, and the relative fcc/bcc phase ratio was estimated as a function of thermal annealing temperature by using the Reference intensity ratio (RIR) quantitative analysis (**see detail of RIR quantitative analysis in supporting information**).[33, 34] As shown in **Figure S5**, very similar fcc/bcc structure ratios of 33.4%/66.6%, 31.8%/68.2%, and 37.8%/62.2% were obtained from PdCu/C-300°C, 400°C, and 500°C samples, respectively. However, the higher annealing temperature of 600°C results in a contrary fcc/bcc structure ratio of 71.3%/28.7%, indicating the fast phase transformation from bcc to fcc structure at such temperature. This phase transformation process of PdCu NPs was further confirmed by the Pd-Cu bulk interface based phase diagram which recognized that the chemically ordered B2 (bcc) phase was produced favorably in the intermediate temperature range of ca. 250°C to 510°C at equal atomic percentages of Cu and Pd.[35, 36]

Combining with the results of HAADF-TEM, in-situ and ex-situ XRD, as well as corresponding fcc/bcc phase estimation, it can be concluded that the bcc crystalline structure was primary in PdCu/C-300°C, 400°C, 500°C samples, while the PdCu/C-200°C and 600°C PdCu NPs were found to be dominated by fcc structure. In comparison with fcc

phase (3.766Å lattice parameter), the bcc structured PdCu NP contains a much smaller lattice parameter of 2.981Å, which may offer different HBE and OH adsorption energy on PdCu NPs surface, so as to influence its HOR activity. Therefore, it is highly possible to attribute the greatly enhanced HOR activity of PdCu/C 300°C/400°C/500°C to the evolution of bcc crystalline phase, thus density functional theory (DFT) calculation was utilized to investigate the H and OH adsorption energy on the specific crystal facet of bcc and fcc structured PdCu NPs, and further elucidate the crystalline structure effect on its HOR activity enhancement in alkaline electrolyte.
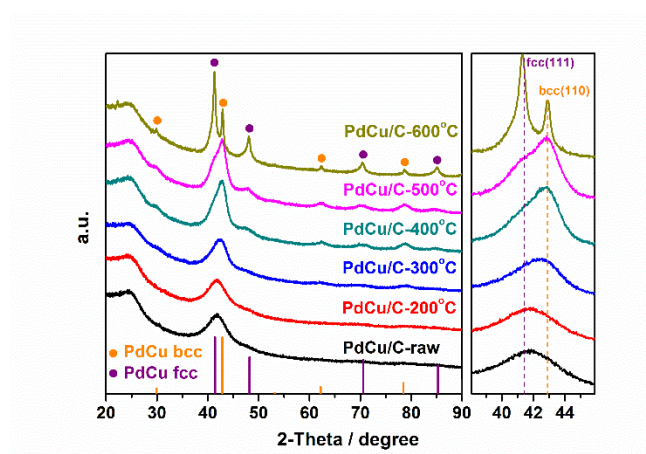
Figure 5.6 XRD patterns for PdCu/C catalysts
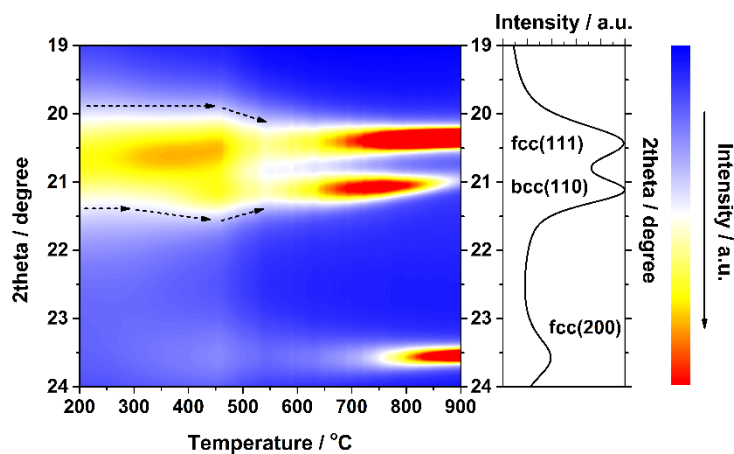
Figure 5.7 Color map of the intensity of peaks in the XRD patterns for PdCu/C-raw upon heating

5.3.4 DFT computation of PdCu catalysts for alkaline HOR

Aiming to acquire theoretical insights into the different HOR activity for PdCu bcc and fcc surfaces, we first calculated the equilibrium adsorption potential of both H and OH on those surfaces. Three representative models of PdCu bcc(110) and fcc(111) surfaces were created owing to their close packed structure with relatively low surface energy, and named to be PdCu-B2(110), PdCu-L1$_0$(111), and PdCu-B13(111), respectively, as illustrated in a previous theoretical work.[37] The surface Pd enrichment observed in the experiments were also considered into these models by using a full Pd overlayer above the bimetallic subsurface (denoted as Pd/M, where M was the bimetallic surface) (**DFT model setup, see supporting information**). The 1/6 ML coverage H and 1/3 ML coverage OH adsorption potential values (denoted as $U_{ad}(H)$ and $U_{ad}(OH)$) on these PdCu close packed surfaces as well as those on Pt(111), Pd(111) and Cu(111), are shown in **Figure 5.8**. We have investigated the coverage dependence of H adsorption potential and found little variation with respect to coverage (**see supporting information**). H binding is the strongest on Pd(111) with the largest adsorption potential ($U_{ad}(H) = 0.36$ V), while the weakest on Cu(111) ($U_{ad}(H) = -0.01$ V). For the three PdCu alloy surfaces, $U_{ad}(H)$ lie well between that of pure Pd and Cu, namely, 0.29 V on Pd/PdCu-B2(110), 0.25 V on Pd/PdCu-L1$_0$(111), and 0.24 V on Pd/PdCu-B13(111), respectively. The $U_{ad}(H)$ on these PdCu surfaces are much closer to that on Pt(111) ($U_{ad}(H) = 0.29$ V) than Pd(111) and Cu(111) surfaces. OH adsorption, on the other hand, is the strongest on Cu(111) ($U_{ad}(OH) = 0.28$ V) while much weaker on Pd(111) ($U_{ad}(OH) = 0.71$ V). However, on all of the three model PdCu surfaces, $U_{ad}(OH)$ are higher than those on both Pd(111) and Cu(111), namely, 0.76 V on Pd/PdCu-B2(110), 0.90 V on Pd/PdCu-L1$_0$(111), and 0.94 V on Pd/PdCu-B13(111), respectively. The variation trends of $U_{ad}(H)$ and $U_{ad}(OH)$ on Pd/PdCu surfaces compared to Pd and Cu

are consistent with those on Pd/Cu surface (**see supporting information**), suggesting that the strain and ligand effects in the near surface PdCu alloy is maintained in Pd/PdCu systems. Interestingly, both H and OH adsorption potential values on Pd/PdCu-B2(110) are almost the same as those on Pt(111) (U_{ad}(H) = 0.29 V, U_{ad}(OH) = 0.78 V). It is well known that Pt possesses the best alkaline HOR catalytic performance among all the pure metals, therefore, Pd/PdCu-B2(110) is anticipated to exhibit remarkable catalytic activity for alkaline HOR. The calculation results are in excellent accordance with experimental results that PdCu nanoparticles containing more bcc phase possess better HOR catalytic activity.

Comparing the adsorption potentials of H and OH on different Pd/PdCu surfaces, H adsorption is only a little weaker on the two Pd/PdCu-fcc(111) surfaces than on Pd/PdCu-B2(110) and Pt(111). It is known that the binding of H on Pt lies near the topmost of the activity volcano. If the adsorption potential of H is the single descriptor in effect, the HOR catalytic activity on Pd/PdCu-fcc(111) should be similar to those on Pd/PdCu-B2(110) and Pt(111), which is contradictive to the experiment. In sharp contrast, OH adsorption strength is weakened by ~0.2 eV on Pd/PdCu-fcc(111) than on Pd/PdCu-B2(110) and Pt(111), suggesting that the lower oxophilicity of the fcc-PdCu(111) surfaces correlates with their relatively poorer catalytic performance. Compared to Pd(111) surface, the weakened extent of both H and OH adsorption is smaller on Pd/PdCu-B2(110) than on Pd/PdCu-L1$_0$ (111) and Pd/PdCu-B13(111) surfaces. It suggests that the different geometrical structures of bcc(110) and fcc(111) substrates give different extent of lattice compression of Pd overlayers. In summary, we argue that it is not sufficient to estimate the alkaline HOR

catalytic activity of a given material by simply measuring the adsorption potential of H. Instead, higher oxophilicity should also be taken into account.

In order to further explore the relation between HOR activity and HBE as well as OH binding energy, we plot the experimental estimated logarithm of the exchange current density as the function of both H and OH adsorption potential, as illustrated in **Figure 5.9 (i_0 calculation, see supporting information and Table S4)**. It is found that on the weak OH binding side, the exchange current density drops much more substantially than that on the strong OH binding side, which corroborates the fact that the observed much poorer HOR performance on Pd/PdCu-fcc(111) is largely attributed to the weaker OH binding, i.e., the lower oxophilicity. It should be further noted that, due to the existence of stepped surfaces on these PdCu nanoparticles as well as the existence of limited amounts of Cu on the surfaces, the OH binding on these surfaces should be stronger than that on Pd/PdCu. However, as illustrated in the volcano in **Figure 5.9**, the exchange current density will be less affected when OH binding moves to the strong side. Therefore, the major conclusion achieved using Pd/PdCu model surfaces is most unlikely to be affected. In summary, due to both the closer HBE and OH binding energies to the volcano top, PdCu-bcc phase is expected to exhibit much better HOR activity than its fcc counterpart.
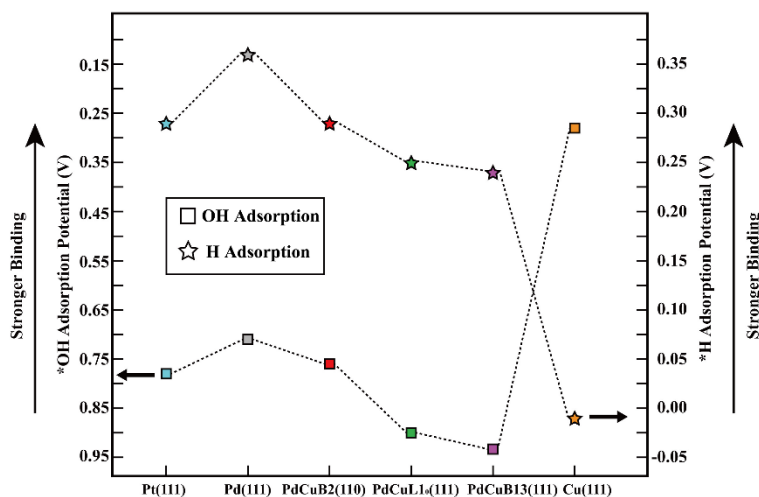
Figure 5.8 Equilibrium adsorption potentials (V_{RHE}) for *H (1/6 ML) and *OH (1/3 ML) on Pt, Pd, bcc-PdCu (B2 phase) and fcc-PdCu (L1$_0$ and B13 phases) terrace surfaces. The three PdCu surfaces shown here are covered by 1ML Pd
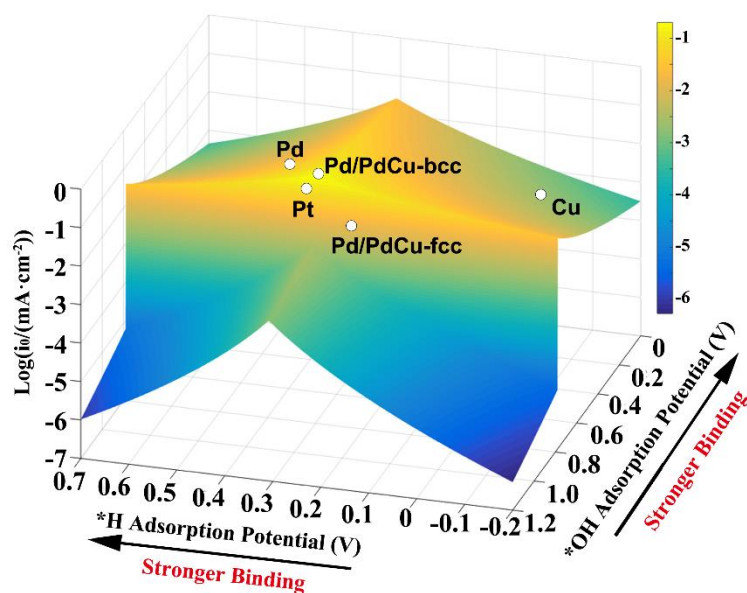
Figure 5.9 Experimentally measured exchange current density, log(i$_o$), for hydrogen oxidation in alkaline over different metals plotted as a function of the calculated H and OH adsorption potential

5.4 Conclusions

In summary, the bcc-phased PdCu alloy nano-particles were successfully synthesized by using wet-chemical method, followed by an additional thermal annealing. The HOR activity of these PdCu catalysts was found to strongly depend on the annealing temperature,

and the PdCu/C-500°C featuring a dominant bcc crystalline structure exhibits about 4 times and 2 times higher mass and specific activity than those of Pd/C and Pt/C in alkaline electrolyte. The crystalline structure transformation between fcc to bcc was observed during thermal annealing from 200°C to 600°C. At lower annealing temperature (<300°C), the as-synthesized PdCu NPs is stabilized with fcc crystalline structure, while the higher annealing temperature (300°C to 600°C) results in a phase transformation from fcc to bcc. Consequently, the correlation of the crystalline structure of PdCu NPs with HOR activity was first created in this work, and it is demonstrated that the higher HOR activity of PdCu catalysts can be attributed to the bcc phase dominance. The DFT computations were used to further investigate HOR enhancement from the perspective of H and OH adsorption strength. As compared to PdCu fcc model surface, it is found that PdCu bcc models surfaces possess very similar H binding and a much stronger OH binding, which are closer to those on the most HOR active Pt model surfaces. Therefore, the bcc phase dominated PdCu/C-500°C catalysts exhibit the outperforming HOR activity in alkaline electrolyte. By taking all results into consideration, the bcc-phased PdCu materials are very promising to be the alternative of Pt materials as the HOR catalyst for AEMFCs.

5.5 References

1.   Sheng, W. C.; Bivens, A. P.; Myint, M.; Zhuang, Z. B.; Forest, R. V.; Fang, Q. R.; Chen, J. G.; Yan, Y. S. *Energ Environ Sci* **2014**, *7*, 1719.

2.   Kibler, L. A. *Chemphyschem* **2006**, *7*, 985.

3.   Neyerlin, K. C.; Gu, W. B.; Jorne, J.; Gasteiger, H. A. *J Electrochem Soc* **2006**, *153*, A1955.

4.   Markovic, N. M.; Gasteiger, H. A.; Philip, N. *J Phys Chem-Us* **1996**, *100*, 6715.

5.   Piana, M.; Catanorchi, S.; Gasteiger, H. A. *ECS Transactions* **2008**, *16*, 2045.

6.   Neyerlin, K. C.; Gu, W. B.; Jorne, J.; Gasteiger, H. A. *J Electrochem Soc* **2007**, *154*, B631.

7.   Bagotzky, V. S.; Osetrova, N. V. *J Electroanal Chem* **1973**, *43*, 233.

8.   Durst, J.; Siebel, A.; Simon, C.; Hasche, F.; Herranz, J.; Gasteiger, H. A. *Energ Environ Sci* **2014**, *7*, 2255.

9.   S. Trasatti, J. Electroanal. Chem., 1977, 39, 183.

10.   Norskov, J. K.; Bligaard, T.; Logadottir, A.; Kitchin, J. R.; Chen, J. G.; Pandelov, S.; Norskov, J. K. *J Electrochem Soc* **2005**, *152*, J23.

11.   Skulason, E.; Tripkovic, V.; Bjorketun, M. E.; Gudmundsdottir, S.; Karlberg, G.; Rossmeisl, J.; Bligaard, T.; Jonsson, H.; Norskov, J. K. *J Phys Chem C* **2010**, *114*, 22374.

12.   Sheng, W. C.; Myint, M.; Chen, J. G. G.; Yan, Y. S. *Energ Environ Sci* **2013**, *6*, 1509.

13.   Zheng, J.; Sheng, W. C.; Zhuang, Z. B.; Xu, B. J.; Yan, Y. S. *Sci Adv* **2016**, *2*.

14.   Sheng, W. C.; Zhuang, Z. B.; Gao, M. R.; Zheng, J.; Chen, J. G. G.; Yan, Y. S. *Nat Commun* **2015**, *6*.

15.   Strmcnik, D.; Uchimura, M.; Wang, C.; Subbaraman, R.; Danilovic, N.; van der Vliet, D.; Paulikas, A. P.; Stamenkovic, V. R.; Markovic, N. M. *Nat Chem* **2013**, *5*, 300.

16.   Li, J.; Ghoshal, S.; Bates, M. K.; Miller, T. E.; Davies, V.; Stavitski, E.; Attenkofer, K.; Mukerjee, S.; Ma, Z. F.; Jia, Q. *Angewandte Chemie International Edition* **2017**, *56*, 15594.

17.   Wang, Y.; Wang, G. W.; Li, G. W.; Huang, B.; Pan, J.; Liu, Q.; Han, J. J.; Xiao, L.; Lu, J. T.; Zhuang, L. *Energ Environ Sci* **2015**, *8*, 177.

18.   Durst, J.; Simon, C.; Hasche, F.; Gasteiger, H. A. *J Electrochem Soc* **2015**, *162*, F190.

19.   McCrum, I. T.; Janik, M. J. *The Journal of Physical Chemistry C* **2016**, *120*, 457.

20.   Chen, X.; McCrum, I. T.; Schwarz, K. A.; Janik, M. J.; Koper, M. T. M. *Angewandte Chemie International Edition* **2017**, *56*, 15025.

21.   Scofield, M. E.; Zhou, Y. C.; Yue, S. Y.; Wang, L.; Su, D.; Tong, X.; Vukmirovic, M. B.; Adzic, R. R.; Wong, S. S. *Acs Catal* **2016**, *6*, 3895.

22.   Greeley, J.; Mavrikakis, M. *Nat Mater* **2004**, *3*, 810.

23.   Jiang, K. Z.; Wang, P. T.; Guo, S. J.; Zhang, X.; Shen, X.; Lu, G.; Su, D.; Huang, X. Q. *Angewandte Chemie-International Edition* **2016**, *55*, 9030.

24.   Qiu, Y.; Xin, L.; Li, W. Z. *Langmuir* **2014**, *30*, 7893.

25.   Zheng, J.; Zhou, S. Y.; Gu, S.; Xu, B. J.; Yan, Y. S. *J Electrochem Soc* **2016**, *163*, F499.

26.   Sheng, W. C.; Gasteiger, H. A.; Shao-Horn, Y. *J Electrochem Soc* **2010**, *157*, B1529.

27.   Fang, L. L.; Tao, Q. A.; Li, M. F.; Liao, L. W.; Chen, D.; Chen, Y. X. *Chin J Chem Phys* **2010**, *23*, 543.

28.   Shao, M. H.; Odell, J. H.; Choi, S. I.; Xia, Y. N. *Electrochem Commun* **2013**, *31*, 46.

29.   Lorimer, J. P.; Mason, T. J.; Plattes, M.; Walton, D. J. *J Electroanal Chem* **2004**, *568*, 379.

30.   Hara, M.; Linke, U; Wandlowski, Th. *Electrochimica Acta* **2007**, *52*, 5733.

31.   Zhang, Z. Y.; Xin, L.; Sun, K.; Li, W. Z. *Int. J. Hydrog. Energy* **2011**, *36*, 12686.

32.   Yang, N. L.; Zhang, Z. C.; Chen, B.; Huang, Y.; Chen, J. Z.; Lai, Z. C.; Chen, Y.; Sindoro, M.; Wang, A. L.; Cheng, H. F.; Fan, Z. X.; Liu, X. Z.; Li, B.; Zong, Y.; Gu, L.; Zhang, H. *Adv Mater* **2017**, *29*.

33.   Hillier, S. *Clay Miner* **2000**, *35*, 291.

34.   Omotoso, O.; Mccarty, D. K.; Hillier, S.; Kleeberg, R. *Clay Clay Miner* **2006**, *54*, 748.

35.   P.R Subramanian, D. E. L. *Journal of Phase Equilibria* **1991**, *12*, 231.

36.   Rudashevsky, N. S.; McDonald, A. M.; Cabri, L. J.; Nielsen, T. F. D.; Stanley, C. J.; Kretzer, Y. L.; Rudashevsky, V. N. *Mineral Mag* **2004**, *68*, 615.

37.   Sha, Y.; Yu, T. H.; Merinov, B. V.; Goddard, W. A. *ACS Catalysis* **2014**, *4*, 1189.

CHAPTER 6. CONCLUDING REMARKS AND RECOMMENDATIONS

My Ph.D. research has been focused on the advanced electrocatalysts design and synthesis for ORR/OER and HER/HOR, and applications in practical energy storage and conversion applications, e.g. fuel cells, and water electrolyzers. With the guidance of DFT calculation results, N-S-dual doped CMK-3 mesoporous materials were synthesized as ORR catalysts exhibiting remarkable ORR activity and durability in direct alcohol fuel cells (alkaline environment) owing to their high surface area with highly organized hierarchical mesoporous structures (**Chapter 3**). The nano-scaled NiFeOx particles were first synthesized through a modified wet chemistry method, and serve as a promising alternative of OER catalysts to IrO_2 and RuO_2 in alkaline electrolyte with very small required overpotential to achieve 10 mA/cm^2 current density, as well as good stability under long term cyclic voltammetry tests (**Chapter 4**). On the other hand, the crystalline structure (fcc & bcc) was found to significantly affect the HOR activity of PdCu NPs in alkaline electrolyte, and bcc-typed PdCu NPs exhibit an outstanding HOR performance and durability, which is much higher than those of all investigated HOR catalysts, including Pt, Pd, and other PdCu/C catalysts treated by different temperature (**Chapter 5**).

Recommendations for the future work include:

1) $NiFeO_x$ flexible electrode fabrication as OER electrode in practical water electrolyzers

2) Rational design Single atom doped N-Carbon materials as ORR catalysts

3) Pure bcc phased PdCu NPs synthesis with the investigation of particles size effect on HOR activity

APPENDIX A. SUPPORTING INFORMATION OF CHAPTER 3
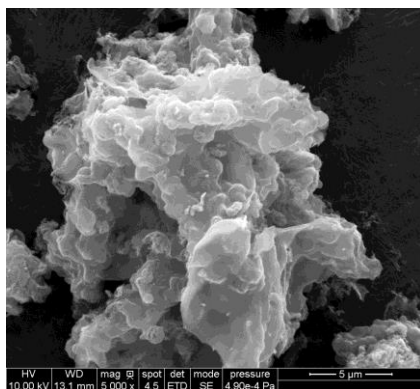
Figure S1 SEM image of CMK-3

(a)   (b)
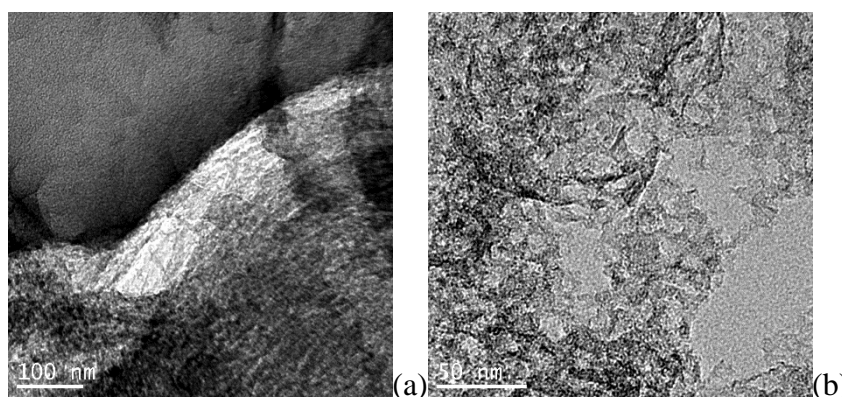
Figure S2 TEM images of (a) N-S-CMK-3 700 °C and (b)N-S-CMK-3 900 °C
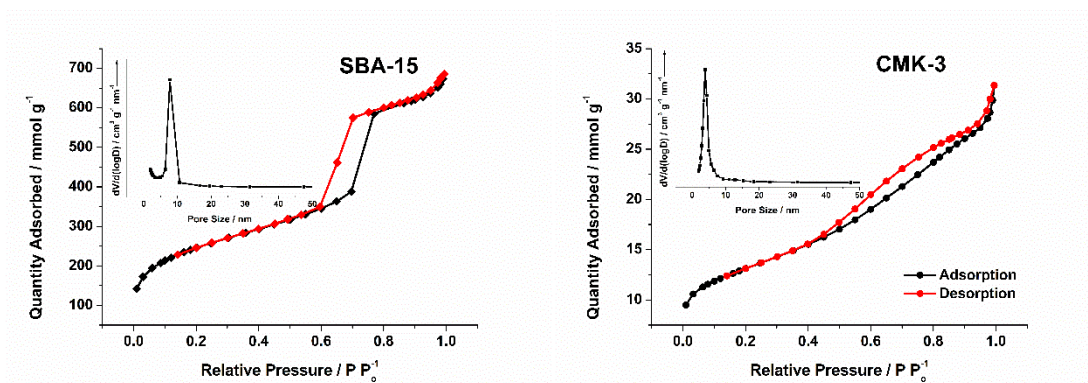
Figure S3 Nitrogen adsorption-desorption isotherms and pore size distribution (Inset) of (a) SBA-15 and (b) CMK-3
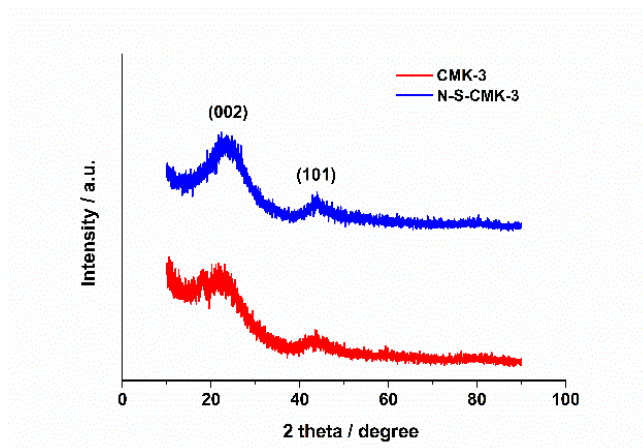
Figure S4 Wide-angle XRD patterns of N-S-CMK-3 800 ºC and CMK-3 catalysts
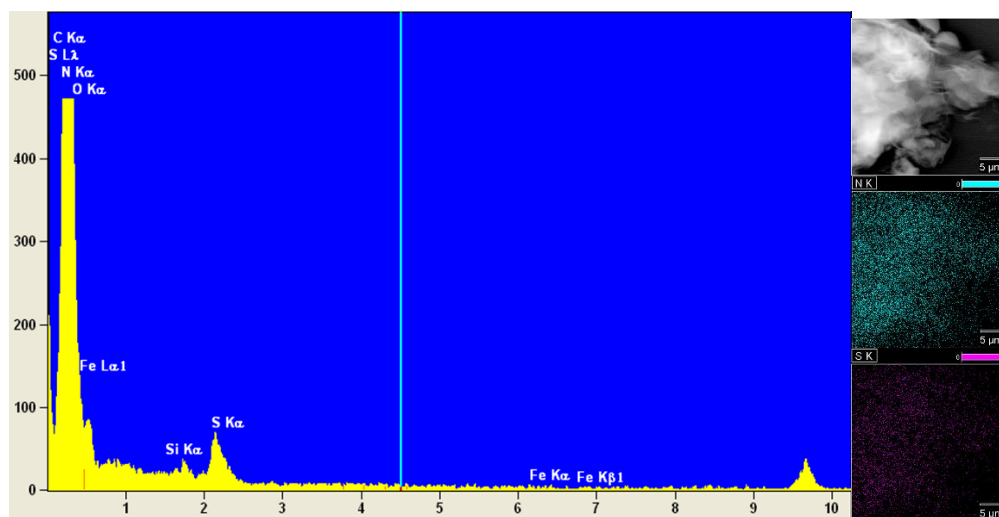
Figure S5 EDS spectrum of N-S-CMK-3 800 ºC, and EDS elemental mapping in conjunction with the TEM images of N and S in N-S-CMK-3 800 ºC
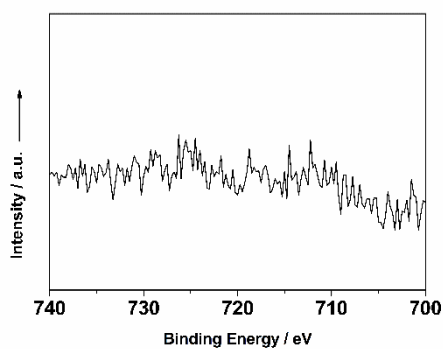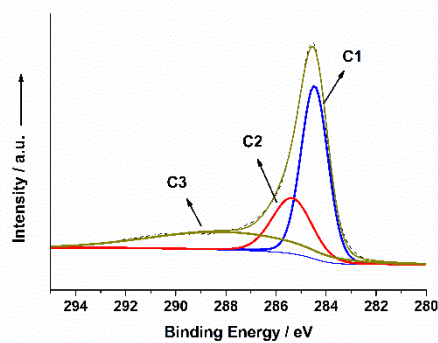
(a)   (b)

Figure S6 XPS high-resolution spectrum of (a) Fe_{2p} and (b) C_{1s} (b) of N-S-CMK-3 800 ºC
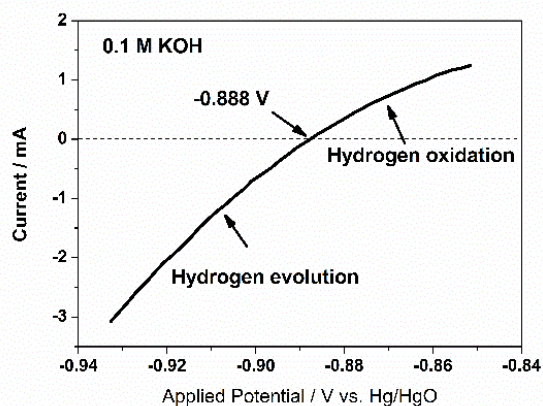
Figure S7 Potential calibration of the Hg/HgO reference electrode in 0.1 M H_2-saturated KOH solution
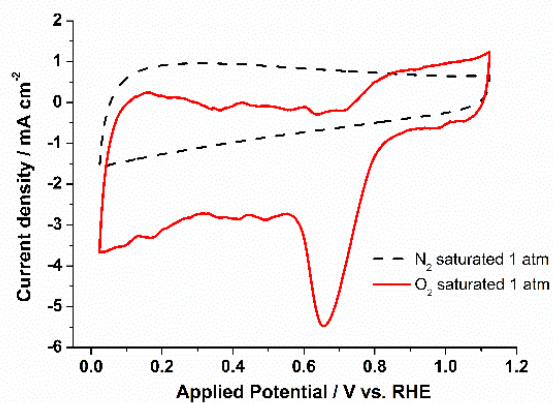
Figure S8 Polarization curves of cyclic voltammetry (CV) tests for N-S-CMK-3 800 ºC in 0.1M KOH solution saturated with N_2 (dash line) and O_2 (solid line) at a scan rate of 50 mV s^{-1}
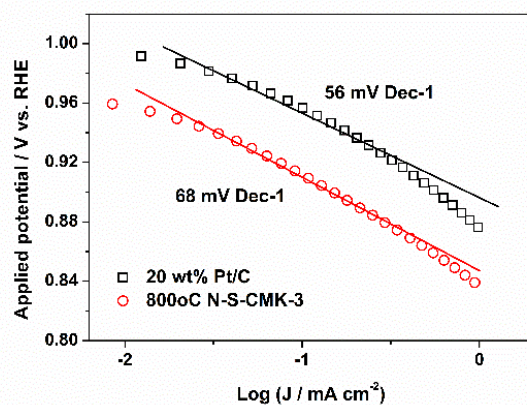
Figure S9 Tafel plots of ORR currents for N-S-CMK-3 800 ºC and commercial Pt/C catalysts
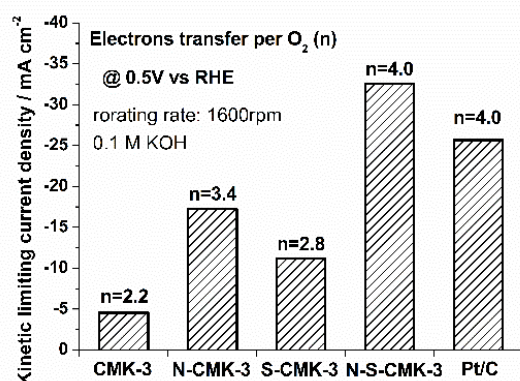
Figure S10 Kinetic limiting current density (j_k) and the calculation of electron transfer number for CMK-3 based and commercial Pt/C catalysts at 0.5V
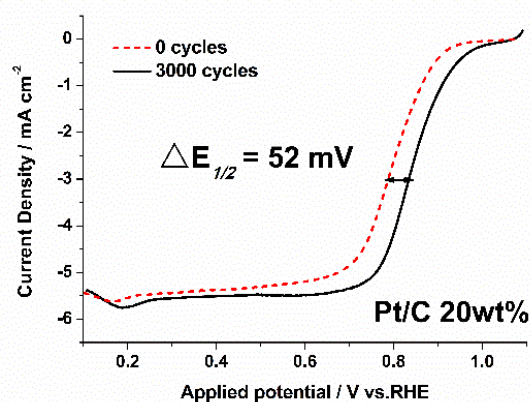
Figure S11 Polarization curves of commercial Pt/C before and after 3000 potential cycles in O_2-saturated 0.1M KOH solution
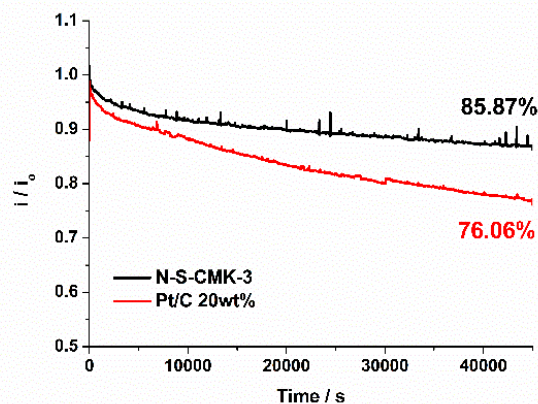
Figure S12 Time-drifting stability of the N-S-CMK-3 800 ºC and commercial Pt/C at 0.5 V vs. RHE for 45000 s with a rotating rate of 1600 rpm
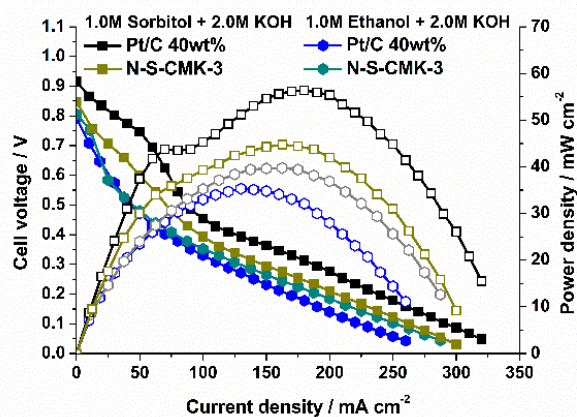
Figure S13 Polarization and power density curves of direct biorenewable alcohol fuel cell with the N-S-CMK-3 800 ºC (loading 2.0 mg cm^{-2}) and commercial Pt/C (loading 1.0 mg$_{Pt}$ cm^{-2}) cathode fed by 1.0 M ethanol + 0.1 M KOH or 1.0 M sorbitol + 0.1 M KOH at 50 ºC
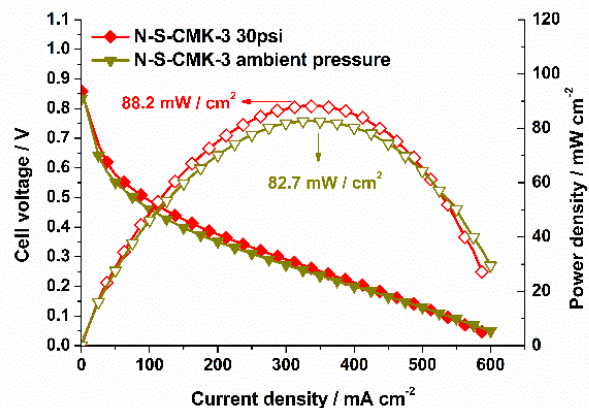
Figure S14 Polarization and power density curves of direct glycerol fuel cell with the N-S-CMK-3 800 ºC cathode (loading 2.0 mg cm^{-2}) at 50 ºC and different O$_2$ back pressures

(a)   (b)
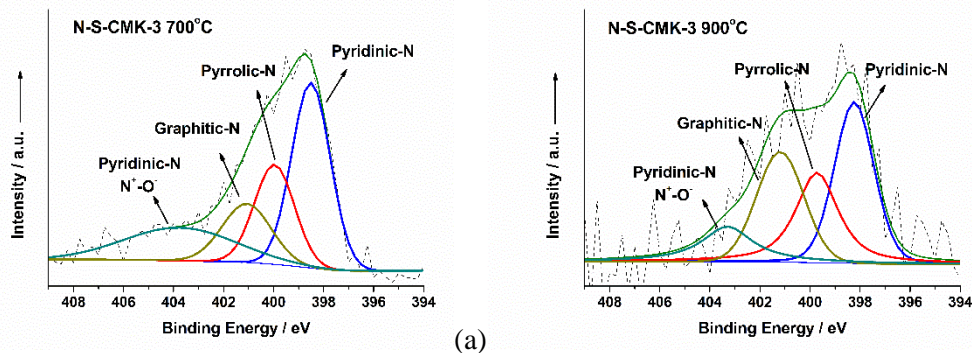
Figure S15 High-resolution spectra of N$_{1s}$ for (a) N-S-CMK-3 700 ºC and (b) N-S-CMK-3 900 ºC

Figure S16 High-resolution spectra of N_{1s} for N-CMK-3

Table S1 The textural parameters and element atomic concentrations of different catalysts

catalyst	BET surface area / $m^2\ g^{-1}$	Total pore volume / $cm^3\ g^{-1}$	Element atomic concentration / atom %				
			C	N	S	O	Fe
CMK-3	1126	1.215	96.51	N/A	N/A	3.33	N/A
N-S-CMK-3 700 °C	784	0.821	90.12	6.40	1.11	2.29	0.08
N-S-CMK-3 800 °C	1023	0.973	94.07	3.84	0.83	1.14	0.12
N-S-CMK-3 900 °C	921	0.701	97.64	1.27	0.20	0.87	0.02
N-CMK-3 800 °C	N/A	N/A	93.31	4.88	N/A	1.77	0.04
S-CMK-3 800 °C	N/A	N/A	97.07	N/A	1.21	1.57	0.15

Table S2 Comparison of the ORR activity of N-S-CMK-3 with other electrocatalysts

Catalysts	ORR onset potential (vs. RHE)	ORR Tafel slope (mV dec^{-1})	Potential at -3 mA cm^{-2} (vs. RHE)	Catalysts loading (mg cm^{-2})	Electron transfer number (*n*) at 0.5V vs. RHE	Electrolyte
800 °C N-S-CMK-3	0.92	68	0.78	0.306	3.96	0.1 M KOH
N-S-G	0.91	N/A	N/A	~0.2	3.6	0.1 M KOH
PCN-CFP	0.94	122.3	N/A	~0.2	3.9	0.1 M KOH
N-S doped graphene/CNT	0.85	N/A	0.72	0.407	3.8	0.1 M KOH
Fe-N/C	0.92	N/A	0.81	0.1	4.0	0.1 M KOH
FeSO4-PEI	0.79	58	0.68	0.4	3.8	0.1 M KOH
Mn3O4/pGC	0.75	~85	~0.7	~0.0001	4.0	0.1 M KOH

APPENDIX B. SUPPORTING INFORMATION OF CHAPTER 5
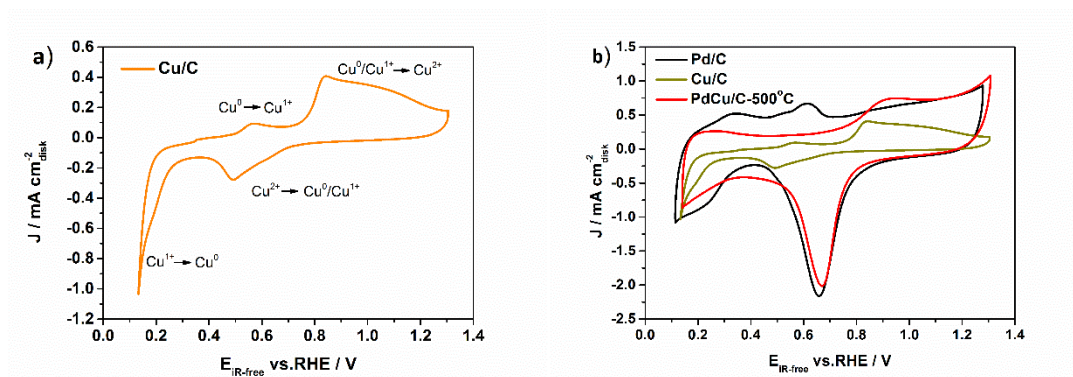
Figure S1 Polarization curves of cyclic voltammetry (CV) tests for Pd/C, Cu/C, and PdCu/C-500°C at a scan rate of 50 mV s^{-1}
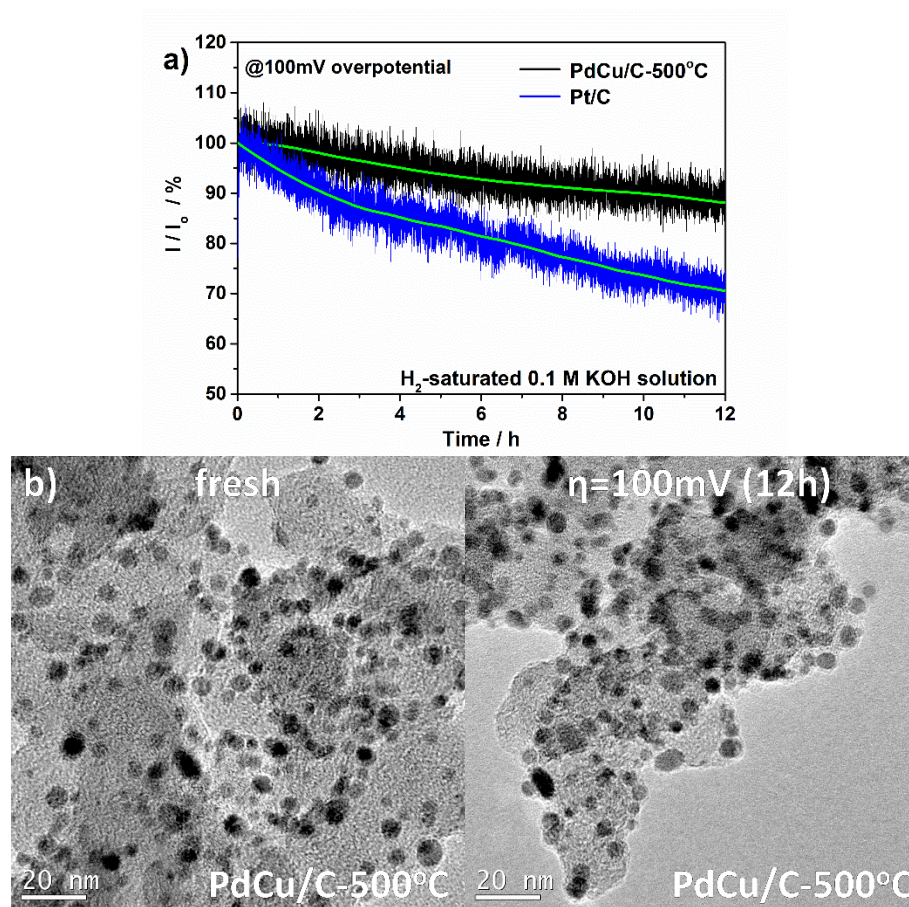
Figure S2 a) Plot of current ratio, I/I$_o$, as a function of time for PdCu/C-500°C at 1600rpm in H$_2$-saturated 0.1 M KOH solution; **b)** Tem images of PdCu/C-500°C before and after 12 durability test
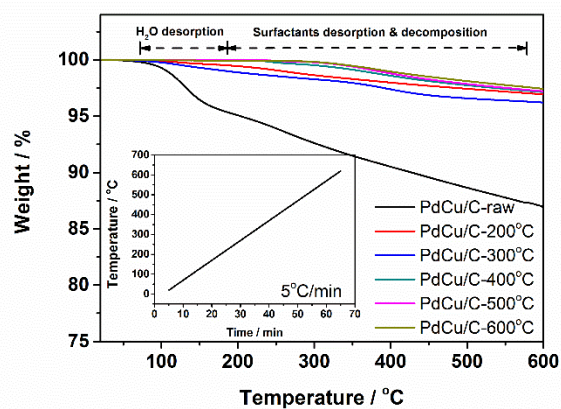
Figure S3 TGA results of PdCu-based materials under UHP N_2 conditions.
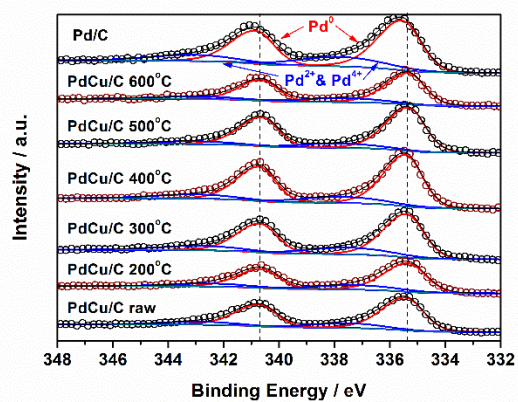
Figure S4 XPS high-resolution spectra of Pd 3d narrow scan of Pd/C and PdCu/C catalysts
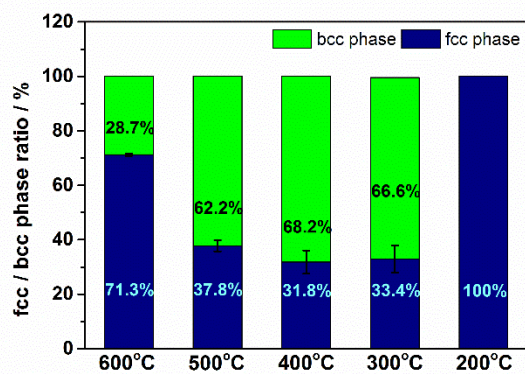
Figure S5 XRD RIR quantitative analysis of fcc/bcc ratio of PdCu/C-T (T=200°C to 600°C)
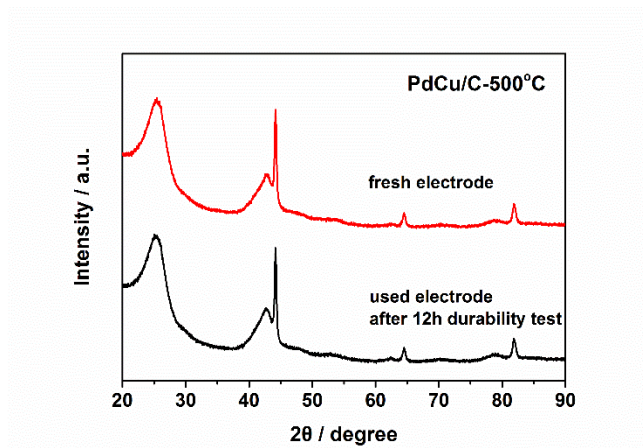
Figure S6 XRD patterns of PdCu/C-500°C before and after 12h durability test

Table S1 Summary of half wave potential, ECSA, MA and SA as 50 mV and 100 mV overpotential of different catalysts in this work

	$E_{1/2}$	ECSA	@ 50mV over-potential			@ 100mV over-potential		
			J_k	MA	SA	J_k	MA	SA
Pt/C	0.047 V	44.6 m^2/g	2.870 mA/cm$^2_{disk}$	0.229 mA/μg$_{Pt}$	0.514 mA/cm$^2_{Pt}$	8.504 mA/cm$^2_{disk}$	0.680 mA/μg$_{Pt}$	1.525 mA/cm$^2_{Pt}$
Pd/C	0.069 V	61.9 m^2/g	1.695 mA/cm$^2_{disk}$	0.135 mA/μg$_{Pd}$	0.219 mA/cm$^2_{Pd}$	4.820 mA/cm$^2_{disk}$	0.385 mA/μg$_{Pt}$	0.623 mA/cm$^2_{Pd}$
Cu/C	N/A	N/A		N/A		N/A		N/A
PdCu/C raw	0.204 V	73.5 m^2/g	0.224 mA/cm$^2_{disk}$	0.018 mA/μg$_{Pd}$	0.024 mA/cm$^2_{Pd}$	0.627 mA/cm$^2_{disk}$	0.050 mA/μg$_{Pt}$	0.068 mA/cm$^2_{Pd}$
PdCu/C 200°C	0.145 V	72.3 m^2/g	0.572 mA/cm$^2_{disk}$	0.046 mA/μg$_{Pd}$	0.063 mA/cm$^2_{Pd}$	1.395 mA/cm$^2_{disk}$	0.112 mA/μg$_{Pt}$	0.152 mA/cm$^2_{Pd}$
PdCu/C 300°C	0.050 V	73.8 m^2/g	2.660 mA/cm$^2_{disk}$	0.213 mA/μg$_{Pd}$	0.288 mA/cm$^2_{Pd}$	10.061 mA/cm$^2_{disk}$	0.804 mA/μg$_{Pt}$	1.091 mA/cm$^2_{Pd}$
PdCu/C 400°C	0.046 V	68.9 m^2/g	3.065 mA/cm$^2_{disk}$	0.245 mA/μg$_{Pd}$	0.356 mA/cm$^2_{Pd}$	11.323 mA/cm$^2_{disk}$	0.906 mA/μg$_{Pt}$	1.315 mA/cm$^2_{Pd}$
PdCu/C 500°C	0.028 V	59.1 m^2/g	6.528 mA/cm$^2_{disk}$	0.522 mA/μg$_{Pd}$	0.883 mA/cm$^2_{Pd}$	21.590 mA/cm$^2_{disk}$	1.727 mA/μg$_{Pt}$	2.922 mA/cm$^2_{Pd}$
PdCu/C 600°C	0.184 V	50.6 m^2/g	0.350 mA/cm$^2_{disk}$	0.028 mA/μg$_{Pd}$	0.055 mA/cm$^2_{Pd}$	0.818 mA/cm$^2_{disk}$	0.065 mA/μg$_{Pt}$	0.129 mA/cm$^2_{Pd}$

Table S2 Literature summary of HOR catalysts

	Electrolyte	@ 50mV over-potential		@ 100mV over-potential		Ref
		MA	SA	MA	SA	
PdCu/C-300°C	0.1 M KOH	0.213 mA/μg$_{pd}$	0.288 mA/cm$^2_{Pd}$	0.804 mA/μg$_{pt}$	1.091 mA/cm$^2_{Pd}$	This work
PdCu/C-400°C	0.1 M KOH	0.245 mA/μg$_{pd}$	0.356 mA/cm$^2_{Pd}$	0.906 mA/μg$_{pt}$	1.315 mA/cm$^2_{Pd}$	This work
PdCu/C-500°C	0.1 M KOH	0.522 mA/μg$_{pd}$	0.883 mA/cm$^2_{Pd}$	1.727 mA/μg$_{pt}$	2.922 mA/cm$^2_{Pd}$	This work
Ni/N-CNT	0.1 M KOH	0.009 mA/μg$_{Ni}$	0.05 mA/cm$^2_{Ni}$	-	-	1
CoNiMo	0.1 M KOH	-	0.044 mA/cm$^2_{Pd}$			2
Pd/CuNW	0.1 M KOH	0.76 mA/μg$_{Pd}$	-	0.944 mA/μg$_{Pd}$	-	3
PdNT (Cu)	0.1 M KOH	0.123 mA/μg$_{Pd}$	-	0.147 mA/μg$_{Pd}$	-	3
PtRu NWs	0.1 M KOH	0.6 mA/μg$_{Pt}$	-	1.667 mA/μg$_{Pt}$	-	4
PtCo NWs	0.1 M KOH	0.307 mA/μg$_{Pt}$	-	0.850 mA/μg$_{Pt}$	-	4
Pt NWs	0.1 M KOH	0.227 mA/μg$_{Pt}$	-	0.714 mA/μg$_{Pt}$	-	4

Table S3 Summary Pd/Cu ratio of PdCu catalysts determined by ICP-OES

	Pd / at.%	Cu / at.%
PdCu/C raw	56.80%	43.20%
PdCu/C 200°C	56.50%	43.50%
PdCu/C 300°C	56.74%	43.26%
PdCu/C 400°C	55.64%	44.36%
PdCu/C 500°C	55.97%	44.03%
PdCu/C 600°C	55.81%	44.19%

Table S4 Summary of mass and specific activity current densities determined from linearized Butler-Volmer equation with the assumption that $\alpha_a + \alpha_c = 1$ in 0.1 M KOH

	i_o	$I_{o,m}$	$I_{o,s}$
Pd/C	0.0939 mA	37.5692 mA/mg$_{Pd}$	0.0607 mA/cm2$_{Pd}$
Pt/C	0.2054 mA	82.1678 mA/mg$_{Pt}$	0.1842 mA/cm2$_{Pt}$
PdCu/C-200°C	0.0282 mA	11.2892 mA/mg$_{Pd}$	0.0156 mA/cm2$_{Pd}$
PdCu/C 500°C	0.3190 mA	127.6172 mA/mg$_{Pd}$	0.2159 mA/cm2$_{Pd}$

Reference

1.   Zhuang, Z. B.; Giles, S. A.; Zheng, J.; Jenness, G. R.; Caratzoulas, S.; Vlachos, D. G.; Yan, Y. S. *Nat Commun* **2016**, *7*.

2.   Sheng, W. C.; Bivens, A. P.; Myint, M.; Zhuang, Z. B.; Forest, R. V.; Fang, Q. R.; Chen, J. G.; Yan, Y. S. *Energ Environ Sci* **2014**, *7*, 1719.

3.   Alia, S. M.; Yan, Y. S. *J Electrochem Soc* **2015**, *162*. F849

4.   Scofield, M. E.; Zhou, Y. C.; Yue, S. Y.; Wang, L.; Su, D.; Tong, X.; Vukmirovic, M. B.; Adzic, R. R.; Wong, S. S. *Acs Catal* **2016**, *6*, 3895.

5.   Zheng, J.; Zhou, S. Y.; Gu, S.; Xu, B. J.; Yan, Y. S. *J Electrochem Soc* **2016**, *163*, F499.

APPENDIX C. COPYRIGHT PERMISSION OF WHOLE ARTICLE CITATION OF CHAPTERS 3, 4

Chapter 3 & Chapter 3 supporting information (Appendix A) in this prelim report were published on RSC Journal of Materials Chemistry A, titled "N- and S-doped mesoporous carbon as metal-free cathode catalysts for direct biorenewable alcohol fuel cells", volumes 4, and pages from 83 to 95 at 2016. The Copyright Permission to reproduce the whole article and copyrighted materials in both print and electronic formats attached below, and Chapter 3, page 36.

N- and S-doped mesoporous carbon as metal-free cathode catalysts for direct biorenewable alcohol fuel cells

Y. Qiu, J. Huo, F. Jia, Brent. H. Shanks and W. Li, *J. Mater. Chem. A*, 2016, **4**, 83
DOI: 10.1039/C5TA06039G

If you are the author of this article you do not need to formally request permission to reproduce figures, diagrams etc. contained in this article in third party publications or in a thesis or dissertation provided that the correct acknowledgement is given with the reproduced material.

Reproduced material should be attributed as follows:

> For reproduction of material from NJC:
> [Original citation] - Reproduced by permission of The Royal Society of Chemistry (RSC) on behalf of the Centre National de la Recherche Scientifique (CNRS) and the RSC

> For reproduction of material from PCCP:
> [Original citation] - Reproduced by permission of the PCCP Owner Societies

> For reproduction of material from PPS:
> [Original citation] - Reproduced by permission of The Royal Society of Chemistry (RSC) on behalf of the European Society for Photobiology, the European Photochemistry Association, and RSC

> For reproduction of material from all other RSC journals:
> [Original citation] - Reproduced by permission of The Royal Society of Chemistry

N- and S-doped mesoporous carbon as metal-free cathode catalysts for direct biorenewable alcohol fuel cells

Reproduced material should be attributed as follows:

> For reproduction of material from NJC:
> [Original citation] - Reproduced by permission of The Royal Society of Chemistry (RSC) on behalf of the Centre National de la Recherche Scientifique (CNRS) and the RSC

> For reproduction of material from PCCP:
> [Original citation] - Reproduced by permission of the PCCP Owner Societies

> For reproduction of material from PPS:
> [Original citation] - Reproduced by permission of The Royal Society of Chemistry (RSC) on behalf of the European Society for Photobiology, the European Photochemistry Association, and RSC

> For reproduction of material from all other RSC journals:
> [Original citation] - Reproduced by permission of The Royal Society of Chemistry

If you are the author of this article you still need to obtain permission to reproduce the whole article in a third party publication with the exception of reproduction of the whole article in a thesis or dissertation.

Chapter 4 in this prelim report was published in Langmuir (American Chemical Society), titled "Electrocatalytic Oxygen Evolution over Supported Small Amorphous Ni-Fe Nanoparticles in Alkaline Electrolyte", volumes 30, and pages from 7893 to 7901 at 2014. The Copyright Permission to reproduce the whole article and copyrighted materials in both print and electronic formats attached below, and Chapter 5, page 95.

Copyright Clearance Center **RightsLink**®

| Home | Create Account | Help | ✉ |

ACS Publications
Most Trusted. Most Cited. Most Read.

Title: Electrocatalytic Oxygen Evolution over Supported Small Amorphous Ni–Fe Nanoparticles in Alkaline Electrolyte
Author: Yang Qiu, Le Xin, Wenzhen Li
Publication: Langmuir
Publisher: American Chemical Society
Date: Jul 1, 2014
Copyright © 2014, American Chemical Society

LOGIN

If you're a copyright.com user, you can login to RightsLink using your copyright.com credentials.
Already **a RightsLink user** or want to learn more?

| BACK | CLOSE WINDOW |

APPENDIX D. COPYRIGHT PERMISSION OF FIGURES/TABLES/TEXT CITED IN THIS REPORT

Figure 1.1 (a-c) of this dissertation were initially published on: http://www.bp.com/content/dam/bp/pdf/energy-economics/energy-outlook-2016/bp-energy-outlook-2016.pdf. The copyright policy of BP p.l.c. is attached as below. The formal copyright permission will be obtained, and attached later.

Figure 1.3 of this dissertation were initially published on http://www.tf.uni-kiel.de/matwis/amat/elmat_en/kap_2/advanced/t2_1_3.html. The reproduction of these graphs is in compliance with the "Reuse and Copyright" info provided by Dr. Helmut Föll, and the permission is attached as above.

Figure 1.4 of this dissertation were initially published on The Journal of Physical Chemistry B at 2004, volume 108, page 17886, titled "Origin of the overpotential for oxygen reduction at a fuel-cell cathode" by Norskov, J. K.; Rossmeisl, J.; Logadottir, A.; Lindqvist, L.; Kitchin, J. R.; Bligaard, T.; and Jonsson, H. The Reprinted with permission from (Norskov, J. K.; Rossmeisl, J.; Logadottir, A.; Lindqvist, L.; Kitchin, J. R.; Bligaard, T.; Jonsson, H., Origin of the overpotential for oxygen reduction at a fuel-cell cathode, 2004, 108, 17886). Copyright (2004) American Chemical Society, as attached above.

Title: Electrolysis of water on oxide surfaces
Author: J. Rossmeisl,Z.-W. Qu,H. Zhu,G.-J. Kroes,J.K. Nørskov
Publication: Journal of Electroanalytical Chemistry
Publisher: Elsevier
Date: 1 September 2007
Copyright © 2006 Elsevier B.V. All rights reserved.

Logged in as:
Yang Qiu
Account #: 3001095614

LOGOUT

Order Completed

Thank you for your order.

This Agreement between Yang Qiu ("You") and Elsevier ("Elsevier") consists of your license details and the terms and conditions provided by Elsevier and Copyright Clearance Center.

Your confirmation email will contain your order number for future reference.

printable details

License Number	4201730225225
License date	Oct 04, 2017
Licensed Content Publisher	Elsevier
Licensed Content Publication	Journal of Electroanalytical Chemistry
Licensed Content Title	Electrolysis of water on oxide surfaces
Licensed Content Author	J. Rossmeisl,Z.-W. Qu,H. Zhu,G.-J. Kroes,J.K. Nørskov
Licensed Content Date	Sep 1, 2007
Licensed Content Volume	607
Licensed Content Issue	1-2
Licensed Content Pages	7
Type of Use	reuse in a thesis/dissertation
Portion	figures/tables/illustrations
Number of figures/tables/illustrations	6
Format	both print and electronic
Are you the author of this Elsevier article?	No
Will you be translating?	No
Original figure numbers	Figure 6
Title of your thesis/dissertation	Rational Design of Advanced Electrocatalysts for Oxygen and Hydrogen Reactions in Fuel Cells and Water Electrolyzers
Expected completion date	Feb 2018
Estimated size (number of pages)	220
Requestor Location	Yang Qiu
2125 Prairie view west
apt 203

AMES, IA 50010
United States
Attn: Yang Qiu |
| Publisher Tax ID | 98-0397604 |

Figure 1.5 (a) of this dissertation were initially published on Journal of Electroanalytical Chemistry at 2007, volume 607, page 83, titled "Electrolysis of water on oxide surfaces" by Rossmeisl, J.; Rossmeisl, J.; Zhu, H.; Zhu, H.; Norskov, J. K.; Nørskov, J. K. The Reprinted with permission from (Rossmeisl, J.; Rossmeisl, J.; Zhu, H.; Zhu, H.; Norskov, J. K.; Nørskov, J. K., Electrolysis of water on oxide surfaces, 2007, 607, 83) Copyright (2006) Elsevier B.V., as attached above.

Copyright Clearance Center

RightsLink®

Home | Account Info | Help

WILEY

Title: Universality in Oxygen Evolution Electrocatalysis on Oxide Surfaces

Author: Isabela C. Man,Hai - Yan Su,Federico Calle - Vallejo,Heine A. Hansen,José I. Martínez,Nilay G. Inoglu,John Kitchin,Thomas F. Jaramillo,Jens K. Nørskov,Jan Rossmeisl

Publication: ChemCatChem

Publisher: John Wiley and Sons

Date: Mar 16, 2011

Copyright © 2011 WILEY - VCH Verlag GmbH & Co. KGaA, Weinheim

Logged in as:
Yang Qiu
Account #:
3001095614

LOGOUT

Order Completed

Thank you for your order.

This Agreement between Yang Qiu ("You") and John Wiley and Sons ("John Wiley and Sons") consists of your license details and the terms and conditions provided by John Wiley and Sons and Copyright Clearance Center.

Your confirmation email will contain your order number for future reference.

printable details

License Number	4201730550926
License date	Oct 04, 2017
Licensed Content Publisher	John Wiley and Sons
Licensed Content Publication	ChemCatChem
Licensed Content Title	Universality in Oxygen Evolution Electrocatalysis on Oxide Surfaces
Licensed Content	Isabela C. Man,Hai - Yan Su,Federico Calle - Vallejo,Heine A. Hansen,José I.

2017/10/3   Rightslink® by Copyright Clearance Center

Author   Martínez,Nilay G. Inoglu,John Kitchin,Thomas F. Jaramillo,Jens K. Nørskov,Jan
                    Rossmeisl

Licensed Content   Mar 16, 2011
Date

Licensed Content   7
Pages

Type of use   Dissertation/Thesis
Requestor type   University/Academic
Format   Print and electronic
Portion   Figure/table
Number of   4
figures/tables
Original Wiley   Figure 4(a)
figure/table
number(s)
Will you be   No
translating?
Title of your thesis / Rational Design of Advanced Electrocatalysts for Oxygen and Hydrogen Reactions
dissertation   in Fuel Cells and Water Electrolyzers
Expected   Feb 2018
completion date
Expected size   220
(number of pages)
Requestor Location Yang Qiu
                    2125 Prairie view west
                    apt 203

                    AMES, IA 50010
                    United States
                    Attn: Yang Qiu
Publisher Tax ID   EU826007151
Billing Type   Invoice
Billing address   Yang Qiu
                    2125 Prairie view west
                    apt 203

                    AMES, IA 50010
                    United States
                    Attn: Yang Qiu

https://s100.copyright.com/AppDispatchServlet

Figure 1.5 (b) of this dissertation were initially published on ChemCatChem at 2011, volume 3, page 1159, titled "Universality in Oxygen Evolution Electrocatalysis on Oxide Surfaces" by Man, I. C.; Su, H. Y.; Calle, V. F.; Hansen, H. A.; Martínez, J. I.; Inoglu, N. G.; Kitchin, J.; Jaramillo, T. F.; Nørskov, J. K.; Rossmeisl, J. The Reprinted with permission from (Man, I. C.; Su, H. Y.; Calle, V. F.; Hansen, H. A.; Martínez, J. I.; Inoglu, N. G.; Kitchin, J.; Jaramillo, T. F.; Nørskov, J. K.; Rossmeisl, J., Universality in Oxygen Evolution Electrocatalysis on Oxide Surfaces, 2011, 3, 1159) Copyright (2011) WILEY-VCH Verlag GmbH & Co. KGaA, Weinheim, as attached above.

Journal of the Electrochemical Society

Order detail ID:	70703800
Order License Id:	4201750327286
ISSN:	0013-4651
Publication Type:	Journal
Volume:	
Issue:	
Start page:	
Publisher:	ELECTROCHEMICAL SOCIETY,
Author/Editor:	ELECTROCHEMICAL SOCIETY

Permission Status: ✅ Granted

Permission type: Republish or display content
Type of use: Republish in a thesis/dissertation

⊟ Hide details

Requestor type	Publisher, not-for-profit
Format	Print, Electronic
Portion	image/photo
Number of images/photos requested	1
The requesting person/organization	Yang Qiu
Title or numeric reference of the portion(s)	Figure 1
Title of the article or chapter the portion is from	Trends in the exchange current for hydrogen evolution
Editor of portion(s)	N/A
Author of portion(s)	Norskov, J. K. Bligaard, T. Logadottir, A. Kitchin, J. R. Chen, J. G. Pandelov, S. Norskov, J. K.
Volume of serial or monograph	152
Issue, if republishing an article from a serial	3
Page range of portion	J23
Publication date of portion	2005
Rights for	Main product
Duration of use	Current edition and up to 5 years
Creation of copies for the disabled	no
With minor editing privileges	no
For distribution to	United States
In the following language(s)	Original language of publication
With incidental promotional use	no

Author of portion(s)	Norskov, J. K. Bligaard, T. Logadottir, A. Kitchin, J. R. Chen, J. G. Pandelov, S. Norskov, J. K.
Volume of serial or monograph	152
Issue, if republishing an article from a serial	3
Page range of portion	J23
Publication date of portion	2005
Rights for	Main product
Duration of use	Current edition and up to 5 years
Creation of copies for the disabled	no
With minor editing privileges	no
For distribution to	United States
In the following language(s)	Original language of publication
With incidental promotional use	no
Lifetime unit quantity of new product	Up to 499
Order reference number	
Title	Rational Design of Advanced Electrocatalysts for Oxygen and Hydrogen Reactions in Fuel Cells and Water Electrolyzers
Instructor name	n/a
Institution name	n/a
Expected presentation date	Feb 2018
Expected size	220

Figure 1.6 of this dissertation were initially published on Journal of The Electrochemical Society at 2005, volume 152, page J23, titled "Trends in the Exchange Current for Hydrogen Evolution" by J. K. Nørskov, T. Bligaard, A. Logadottir, J. R. Kitchin, J. G. Chen, S. Pandelov and U. Stimming. Reprinted with permission from J. Electrochem. Soc., 152, J23 (2005). Copyright 2003, The Electrochemical Society., as attached above.

CyMail

Yang Qiu <yangqiu@iastate.edu>

Contact Page: use of copyrighted images
2 messages

Li Sun <lsun@pineresearch.com>   Tue, Dec 27, 2016 at 9:49 AM
To: "yangqiu@iastate.edu" <yangqiu@iastate.edu>
Cc: Diane White <dwhite@pineresearch.com>

Yang Qiu, yes, we permit you to use the said images, with one condition: you have to acknowledge the source right next to every image that will appear in your thesis. For example, if the images appear in two different pages, then the acknowledgment has to appear twice on those pages. Please add the following phrase next to the images you mentioned:

"Copyright Pine Research Instrumentation (www.pineresearch.com), used with permission"

Thank you for your inquiry, and please ask us again if you need to use other images for your thesis. Li.

Reason for request

General Inquiry

Name

Yang Qiu

Phone

9063708239

Email

yangqiu@iastate.edu

Affliated Insitution

Iowa State University

Street Address

2130B-A BRL
Ames, Iowa 50011
United States
Map It

Comments:

Hello Sir,

My name is Yang Qiu, PhD student of Iowa State University.

I would like to use two graphs in my PhD dissertation, and want to request the copyright of these two graphs.

The first graph is E3PK Fixed-Disk RDE tips, and the second graph is E6R2 Fixed-Disk RRDE tips.

I also attache these two graphs for you, and very appreciate that you can give me the copyright permission to use these two graphs in my dissertation "Rational Design of Advanced Electrocatalysts for Oxygen Reduction and Evolution Reactions in Alkaline environment".

Thanks.

Yang Qiu
Iowa State University, Chemical and Biological Engineering
9063708239

Attach Support Files

- Graphs-from-Pine.pdf

Yang Qiu <yangqiu@iastate.edu>   Tue, Dec 27, 2016 at 10:00 AM
To: Li Sun <lsun@pineresearch.com>
Cc: Diane White <dwhite@pineresearch.com>

Thanks so much.
[Quoted text hidden]
--

Yang Qiu

Ph.D student of Chemical & Biological Engineering
Iowa State University
2130-B Biorenewables Research Laboratory, Ames, Iowa, 50011
Email: yangqiu@iastate.edu

Figure 2.5 of this dissertation were reproduced from the website of Pine Research Instrumentation. The reproduction of these graphs is in compliance with the "Reuse and Copyright" info provided by Pine Research Instrumentation, as attached above.

RightsLink®

Home | Account Info | Help | ✉

Title: Li-O2 and Li-S batteries with high energy storage

Author: Peter G. Bruce, Stefan A. Freunberger, Laurence J. Hardwick, Jean-Marie Tarascon

Publication: Nature Materials

Publisher: Nature Publishing Group

Date: Dec 15, 2011

Copyright © 2011, Rights Managed by Nature Publishing Group

Logged in as:
Yang Qiu
Account #:
3001095614

LOGOUT

Order Completed

Thank you for your order.

This Agreement between Yang Qiu ("You") and Nature Publishing Group ("Nature Publishing Group") consists of your license details and the terms and conditions provided by Nature Publishing Group and Copyright Clearance Center.

Your confirmation email will contain your order number for future reference.

printable details

License Number	4201731102063
License date	Oct 04, 2017
Licensed Content Publisher	Nature Publishing Group
Licensed Content Publication	Nature Materials
Licensed Content Title	Li-O2 and Li-S batteries with high energy storage
Licensed Content Author	Peter G. Bruce, Stefan A. Freunberger, Laurence J. Hardwick, Jean-Marie Tarascon
Licensed Content Date	Dec 15, 2011
Licensed Content Volume	11
Licensed Content Issue	1

Type of Use	reuse in a dissertation / thesis
Requestor type	non-commercial (non-profit)
Format	print and electronic
Portion	figures/tables/illustrations
Number of figures/tables/illustrations	1
High-res required	no
Figures	Data for several electrochemical reactions that form the basis of energy-storage devices
Author of this NPG article	no
Your reference number	Table 1
Title of your thesis / dissertation	Rational Design of Advanced Electrocatalysts for Oxygen and Hydrogen Reactions in Fuel Cells and Water Electrolyzers
Expected completion date	Feb 2018
Estimated size (number of pages)	220
Requestor Location	Yang Qiu 2125 Prairie view west apt 203 AMES, IA 50010 United States Attn: Yang Qiu
Billing Type	Invoice
Billing address	Yang Qiu 2125 Prairie view west apt 203 AMES, IA 50010 United States Attn: Yang Qiu
Total	0.00 USD

ORDER MORE   CLOSE WINDOW

Table 1 of this dissertation were reproduced on Nature Materials at 2011, volume 11, page 19, titled "Li–O$_2$ and Li–S batteries with high energy storage" by Bruce, P.; Freunberger, S.; Hardwick, L.; Tarascon, J. M. The reproduction of table is in compliance with the "Reuse and Copyright" info provided by Nature Publishing Group, as attached below:

The text (page 27) of Ni(OH)$_2$ synthesis through hydrothermal method example of this dissertation were reproduced on ACS Applied Materials & Interfaces at 2015, volume 7, page 9203, titled "Ultrathin Two-Dimensional Free-Standing Sandwiched NiFe/C for High-Efficiency Oxygen Evolution Reaction" by Feng, Y. Y.; Zhang, H. J.; Zhang, Y.; Li, X.; and Wang, Y. The reproduction of table is in compliance with the "Reuse and Copyright" info provided by American Chemical Society, as attached below: